UC Berkeley
UC Berkeley Electronic Theses and Dissertations

Title
Numerical Simulations of Tungsten under Helium Irradiation

Permalink
https://escholarship.org/uc/item/1s75n203

Author
Faney, Thibault

Publication Date
2013

Peer reviewed|Thesis/dissertation

eScholarship.org Powered by the California Digital Library
University of California

Numerical Simulations of Tungsten under Helium Irradiation

by

Thibault Faney

A dissertation submitted in partial satisfaction of the
requirements for the degree of
Doctor of Philosophy

in

Engineering - Nuclear Engineering
and the Designated Emphasis
in
Energy Science and Technology
and the Designated Emphasis
in
Computational Science and Engineering

in the

Graduate Division

of the

University of California, Berkeley

Committee in charge:

Professor Joonhong Ahn, Chair
Professor Brian D. Wirth
Professor Donald R. Olander
Professor James A. Sethian

Fall 2013

Abstract

Numerical Simulations of Tungsten under Helium Irradiation

by

Thibault Faney

Doctor of Philosophy in Engineering - Nuclear Engineering
and the Designated Emphasis
in
Energy Science and Technology
and the Designated Emphasis
in
Computational Science and Engineering

University of California, Berkeley

Professor Joonhong Ahn, Chair

Magnetic confinement fusion is a promising technology for electricity production due to available fuel and low waste products. However, the construction of a nuclear fusion reactor remains a scientific challenge. One of the main issues is the resistance of the plasma facing materials exposed to very harsh operating conditions. Tungsten is the leading candidate for the divertor, a crucial plasma facing component. This dissertation focuses on modeling the behavior of tungsten under irradiation conditions relevant to the divertor operations using a multi-scale modeling approach. In particular, high fluxes of helium ions at low energy impact the divertor and are responsible for changes in the tungsten microstructure such as the formation of helium blisters and "fuzz"-like structures which can ultimately lead to erosion, degradation of materials performance and materials failure.

A spatially dependent cluster dynamics model is introduced in order to model the evolution of the tungsten microstructure under irradiation. This continuum model is based on kinetic rate theory and handles each material defect type independently. Under the assumptions of a low dilute limit and no spatial correlation between defects, this leads to a large system of non-linear reaction-diffusion equations. Hence, the results addressed in this thesis consist in the determination of the kinetic parameters for the cluster dynamics model, the construction of a solver which efficiently deals with the large non-linear system of partial differential equations, the determination of the applicability of the model to fusion relevant conditions, and the model results for a variety of irradiation conditions.

The input kinetic parameters to the cluster dynamics model are the defects' diffusion coefficients,

binding energies and capture radii. These can be determined using a molecular dynamics and density functional theory simulations as well as empirical data. The challenge lies in obtaining a consistent set of kinetic parameters. Therefore, a method to determine the value of the diffusion coefficients for small helium, interstitial and vacancy defects at various temperatures using only molecular dynamics simulations is presented. Binding energies are also determined using molecular dynamics, and when combined with the diffusion coefficients they form a consistent set of kinetic parameters.

An efficient implementation of a parallel solver is presented to deal with the large number of stiff non linear reaction diffusion equations. The implementation of a SDIRK scheme using a modified version of the SPIKE algorithm gives excellent parallelization results and suggests that this implementation would also be efficient for an extension of the model to two or three dimensions. Convergence results for a variety of SDIRK schemes show a convergence order reduction of the numerical scheme due to the stiffness of the reaction and diffusion terms.

A comparison between simulation results using the cluster dynamics model and experimental results is essential to assess the validity of the model. Comparison with thermal helium desorption spectrometry experiments at low flux and fluence shows an excellent agreement between simulation and experiments and indicate that the model captures the key physical properties affecting the evolution of the tungsten microstructure. Further comparison with molecular dynamics simulations at extremely high fluxes provides an insight in the expected limitations of the model due to surface effects and dilute limit approximations breakdown when applied to fusion relevant conditions.

Results of the model under fusion relevant conditions show the formation of large helium bubbles under the surface at a temperature dependent depth. The results are very sensitive to both irradiation flux and temperature. At large temperatures, a small concentration of large bubbles forms first deep under the tungsten surface, and forms a “plug” which moves towards the surface until eventually the dilute limit approximation breaks down, indicating that the sub-surfaces bubbles become interlinked. At small temperatures, a larger concentration of smaller bubbles forms close to the surface until eventually surface effects such as bubble bursting are expected to occur. These results are found to be in good agreement with a similar analytical reaction diffusion model for fusion relevant conditions. More work is needed to simulate past the dilute limit breakdown and examine the possibility of taking into account surface effects.

Contents

Contents **i**

List of Figures **iii**

List of Tables **vii**

1 Introduction **1**
1.1 The Need for Fusion Energy 1
1.2 Magnetic Confinement Fusion 3
1.3 Divertor Materials Challenges 5
1.4 Dissertation Objectives and Outline 7

2 Cluster Dynamics Model **12**
2.1 Introduction 12
2.2 Insight from Experiments and Molecular Dynamic Simulations 12
2.3 Objective and Notation 13
2.4 Description of the Physical Processes 15
2.4.1 Diffusion 15
2.4.2 Clustering Reactions 16
2.4.3 Dissociation Events 17
2.4.4 Source term 19
2.4.5 Boundary Conditions 19
2.5 Equations 20

3 Molecular Dynamics for Parameter Estimation **24**
3.1 Introduction 24
3.2 Background on Molecular Dynamics 24
3.3 Diffusion Coefficients 26
3.3.1 Methodology 26
3.3.2 Helium results 30
3.3.3 Self-Interstitial results 32
3.3.4 Vacancy results 33

3.3.5 Comparison with experimental values . . . 35
3.4 Binding Energies . . . 35
3.5 Capture radii . . . 40

4 Cluster Dynamics Solver **41**
4.1 Introduction . . . 41
4.2 Numerical Analysis . . . 41
4.2.1 System of Equations . . . 41
4.2.2 Existence and uniqueness of solutions . . . 42
4.2.3 Spatial Discretization . . . 43
4.2.4 Numerical Scheme . . . 44
4.3 Implementation . . . 46
4.3.1 Algorithm . . . 47
4.3.2 Practical Implementation . . . 50
4.4 Results . . . 54
4.4.1 Standard cases . . . 54
4.4.2 Convergence of SDIRK algorithms . . . 55
4.4.3 Parallel Performances . . . 57

5 Cluster Dynamics Model validation **60**
5.1 Comparison with experimental results . . . 60
5.1.1 Experimental conditions modeled in this work . . . 60
5.1.2 Modeling results . . . 63
5.1.3 Effect of implanted He fluence on THDS behavior . . . 66
5.2 Comparison with Molecular Dynamics . . . 67
5.2.1 MD Results . . . 67
5.2.2 Modeling Results . . . 69
5.2.3 Conclusion . . . 72

6 Cluster Dynamics Results under Fusion Relevant Conditions **73**
6.1 Trap mutation phenomenon . . . 73
6.2 Extension of the model to large clusters . . . 74
6.3 Results . . . 77
6.3.1 Tendril Geometry . . . 77
6.3.2 Half-Slab Geometry . . . 84
6.4 Conclusion . . . 93

7 Conclusion **94**

Bibliography **97**

List of Figures

1.1 World Energy Consumption from 1965-2011, as reproduced from reference [1]. 1
1.2 World Net Energy Generation from 1980-2009, as reproduced from reference [2]. . . . 2
1.3 a Global Greenhouse Emissions by Sector and b Global CO_2 Emissions from 1980-2010, as reproduced from reference [3]. 3
1.4 ITER schematic and origin of the main components, as reproduced from reference [4]. 4
1.5 Poloidal cross-section of a tokamak plasma, as reproduced from reference [5]. 6
1.6 SEM images of polycristalline tungsten following 1.3 MeV He implantation to a fluence of a 10^{22} He/m^2 , b 2×10^{21} He/m^2, c 10^{21} He/m^2 at 850°C and then flash heated at 2000°C, as reproduced from reference [6]. 7
1.7 Thermal hydrogen desorption results with a temperature ramp of 50 K/min. a The tungsten material was first irradiated at room temperature with 5 keV helium up to a fluence of 1.4×10^{21} He/m^2, followed by 1.7 keV H up to a fluence of 5×10^{22} H/m^2. b The tungsten material was first irradiated at room temperature with 1.7 keV H up to a fluence of 5×10^{22} H/m^2, followed by 5 keV helium up to a fluence of 1.4×10^{21} He/m^2. Figures reproduced from reference [7]. 7
1.8 SEM micrographs of tungsten surface after 50 eV helium irradiation at 1400 K up to a fluence of (a) 6×10^{24} He/m^2, (b) 1.1×10^{25} He/m^2, (c) 1.8×10^{25} He/m^2, (d) 2.4×10^{25} He/m^2, (e) 5.5×10^{25} He/m^2, as reproduced from reference [8]. 8
1.9 Multi-scale computational materials modeling 9

2.1 MD simulation results for a $30 \times 30 \times 30$ a_0 tungsten box at 500 Kelvin with a helium atom inserted at a random position every 100 ps. (a) time = 500 ps. Helium atoms diffuse and react to form small diffusing helium interstitial clusters. (b) time = 1 ns. Larger helium interstitial clusters are formed. The largest ones are immobile. (c) time = 1.5 ns. A SIA was emitted from a large helium interstitial clusters which sits in the remaining vacancy. (d) time = 2ns. The SIA diffused towards another helium-vacancy cluster in formation. 14
2.2 Range of 250 eV helium in Tungsten as calculated by SRIM [9]. 19

3.1 (a) Center of mass trajectory of a He_2 cluster at 1000 K, and (b) spatial trajectory of a He_2 cluster at 1000 K. 26

3.2 MSD_{time} curves for a He_2 cluster diffusing at 300 K. The 100 nanosecond trajectory was split into 10 sub-trajectories of 10 nanoseconds each (The graphs are plotted using the MSDanalyzer MATLAB package [10]). 28
3.3 MSD curve for a He_2 cluster diffusing at 300 K. The MD simulation duration is 100 nanoseconds and the number of sub-trajectories was 100, each lasting one nanosecond. The black area indicates the 95 $\%$ confidence interval, and the red curve is the linear regression giving the value of the diffusion coefficient. 29
3.4 MSD curves for a He_2 cluster diffusing at 300 K for different numbers of sub-trajectories. Equation 3.9 gives $\tau_{min} = 4 \times 10^{-6}$ ns. (a) 10 sub-trajectories of 10 ns each. $D = 1.05 \times 10^{-11}$ m^{2}s^{-1}. (b) 100 sub-trajectories of 1 ns each. $D = 1.25 \times 10^{-11}$ m^{2}s^{-1}. (c) 1000 sub-trajectories of 0.1 ns each. $D = 1.24 \times 10^{-11}$ m^{2}s^{-1}. (d) 10000 sub-trajectories of 0.01 ns each. $D = 1.24 \times 10^{-11}$ m^{2}s^{-1}. 30
3.5 Diffusion coefficient versus inverse temperature for helium interstitials and several helium clusters. 31
3.6 Trajectory of a single self-interstitial for a 100 ns simulation at various temperatures. (a) 300 Kelvin, (b) 750 Kelvin, and (c) 1000 Kelvin. 33
3.7 Diffusion coefficient versus temperature for SIA clusters. 34
3.8 Trajectory of a single vacancy at 1900 Kelvin. 35
3.9 Diffusion coefficient versus inverse temperature for a single vacancy. 36
3.10 Binding Energies for He_xV_y species from DFT simulations by Becquart et al. [11]. (a) Binding Energies for the reaction $He_xV_y \rightarrow He_{x-1}V_y + He$. (b) Binding Energies for the reaction $He_xV_y \rightarrow He_xV_{y-1} + V$. 38
3.11 Binding Energies for He_xV_y species obtained from MD simulations by Juslin et al. [12]. (a) helium binding energy and (b) vacancy binding energy. 39

4.1 Butcher tableau for the L-stable SDIRK method of order 4, as reproduced from Ref [13] 46
4.2 Schematic diagram of the algorithm. Local steps do not require any form of grid-to-grid communication. 53
4.3 Case A results (Depth integrated concentration of all species modeled). 54
4.4 Convergence results for several SDIRK schemes on test problem A. 56
4.5 Strong scaling results for the test problem B. Linear speedup indicates the ideal case in which $S_p = p$. 58
4.6 Weak scaling results for test problem B with 10 grid points per processor 59

5.1 THDS spectrum reproduced from Kornelsen [14] obtained after 5 keV Kr^+ irradiation to a fluence of $8 \times 10^{15}/m^2$, followed by 250 eV He^+ implantation to a fluence of $8 \times 10^{16}/m^2$ at room temperature. The dashed lines indicate the assumed reactions that can describe the observed desorption peaks. 62
5.2 Spatial distribution of single vacancies after $8 \times 10^{11}/cm^2$ 5 keV Kr^+ irradiation. . . . 64
5.3 Distribution of He_nV clusters predicted following 250 eV He^+ implantation to a fluence of $8 \times 10^{16}/m^2$ in Kr ion irradiated tungsten at room temperature. 64

5.4 Model predictions (blue) and measured THDS (black) spectra following 250 eV He^+ implantation to a fluence of $8 \times 10^{16}/m^2$. The experimental results are reproduced from reference [14]. 66
5.5 Model predictions (left) and measured THDS (right) for experiments performed using 5 keV Kr^+ irradiation to a fluence of $8 \times 10^{15}/m^2$ followed by 250 eV He^+ implantation to fluences from $4.4 \times 10^{15}/m^2$ to $1.8 \times 10^{17}/m^2$. The experimental results are reproduced from reference [14]. 67
5.6 Evolution in time of the helium bubble, tungsten interstitials, and surface adatoms during growth of a helium bubble below a tungsten surface (ag). Red spheres are vacant sites, green are displaced tungsten atoms, purple are surface adatoms, blue spheres are helium, and gray spheres are tungsten atoms. (a) to (h) only show the helium, displaced tungsten atoms and vacancies, with the original surface represented by a rectangle. (i) is a top-down view of the final surface with all the atoms represented. Trap-mutation processes of single interstitial formation repeatedly occur as gas pressure increases, leading to the self-assembly of prismatic loops, which de-trap from the bubble and glide to the surface, forming multiple adatom islands. Ultimately, the bubble ruptures (g,h), leaving a heavily deformed surface (i) with multiple layers of tungsten adatom islands, a crater, and a hole. This figure is reproduced from reference [15]. 68
5.7 CD and MD comparison of helium retention for a flux of 2.4×10^{27} Hem^{-2}s^{-1} up to a fluence of 2×10^{19} He m^{-2}. 69
5.8 CD and MD comparison of helium content in clusters for a flux of 2.4×10^{27} He m^{-2}s^{-1} up to a fluence of 2×10^{19} He m^{-2}, as a function of temperature. 70
5.9 Example of a coalescence event between two bubbles (MD simulation performed by Faiza Sefta). 71
5.10 Volume Fraction of helium clusters for a flux of 2.4×10^{27} He m^{-2}s^{-1} up to a fluence of 2×10^{19} He m^{-2}, as a function of temperature. 71

6.1 Limiting number of helium per vacancy at which trap mutation occurs at 0 K. 74
6.2 SEM micrograph showing a tungsten surface after 50 eV helium ion irradiation up to a fluence of $1.1 \times 10^{25} m^{-2}$ at $1400K$, as reproduced from Ref [8]. 77
6.3 Concentration of mobile helium clusters and immobile helium-vacancy clusters in a tendril after 10^{22} $m^{-2}s^{-1}$ 100 eV helium irradiation at 1000 K up to a fluence of $5 \times 10^{25} m^{-2}$. 78
6.4 Concentration of mobile helium clusters and immobile helium-vacancy clusters in a tendril after 10^{22} $m^{-2}s^{-1}$ 100 eV helium irradiation at 500 K up to a fluence of $5 \times 10^{25} m^{-2}$. 79
6.5 Concentration of mobile helium clusters and immobile helium-vacancy clusters in a tendril after 10^{22} $m^{-2}s^{-1}$ 100 eV helium irradiation at 1500 K up to a fluence of $5 \times 10^{25} m^{-2}$. 80
6.6 Concentration of mobile helium clusters and immobile helium-vacancy clusters in a tendril after 10^{21} $m^{-2}s^{-1}$ 100 eV helium irradiation at 1000 K up to a fluence of $5 \times 10^{25} m^{-2}$. 81

6.7 Concentration of mobile helium clusters and immobile helium-vacancy clusters in a tendril after 10^{23} $m^{-2}s^{-1}$ 100 eV helium irradiation at 1000 K up to a fluence of $5 \times 10^{25}m^{-2}$. 82
6.8 Steady-state concentrations of mobile helium clusters in a tendril for $10^{22}m^{-2}s^{-1}$ 100 eV helium implantation at 1000 K, as reproduced from reference [16]. 83
6.9 Time required to produce a single immobile helium cluster in the tendril as a function of helium implantation flux at 1000 K for both models. 83
6.10 Concentration of helium interstitial atoms and helium bubbles after 10^{22} $m^{-2}s^{-1}$ 100 eV helium irradiation at 1000K up to a fluence of $5 \times 10^{25}m^{-2}$. 85
6.11 Volume fraction of helium species under the tungsten surface after $10^{22}m^{-2}s^{-1}$ 100 eV helium implantation at 1000 K up to a fluence of $5 \times 10^{23}m^{-2}$. 86
6.12 Average radius (6.12a) and helium content (6.12b) under the tungsten surface after $10^{22}m^{-2}s^{-1}$ 100 eV helium implantation at 1000 K up to a fluence of $5 \times 10^{23}m^{-2}$. . . 87
6.13 Concentration of large HeV clusters (6.13a),average radius (6.13b) and volume fraction (6.13c) under the tungsten surface after $10^{22}m^{-2}s^{-1}$ 100 eV helium implantation at 500 K up to a fluence of $2 \times 10^{22}m^{-2}$. 89
6.14 Concentration of large HeV clusters ($\geq$ $He_{250}V_{50}$) under the tungsten surface after $10^{22}m^{-2}s^{-1}$ 100 eV helium implantation at 1500 K up to a fluence of $5 \times 10^{25}m^{-2}$. . . 90
6.15 Qualitative picture of the evolution of the concentration of the helium bubbles. $\hat{C}$, $\hat{t}$ and $\hat{x}$ are dimensionless quantities depending on the flux and temperature. 92

List of Tables

2.1 List of possible clustering reactions considered in this model. 17
2.2 List of possible dissociation reactions considered in this model. 18

3.1 Activation energy and diffusion pre-factor for small helium interstitial clusters. 31
3.2 Activation energy and diffusion pre-factor for SIA clusters. 34
3.3 Activation energy and diffusion pre-factor for a single vacancy and vacancy clusters. . 34
3.4 Comparison of migration energies between simulation results in this work, experimental results and other simulation results. 36
3.5 Summary of dissociation events for small He_xV_y clusters, and associate binding energies, as obtained from analysis of experimental THDS measurements [14] or theoretical modes [17, 18] 39

4.1 Parameters used in the standard case. 55
4.2 SDIRK schemes used in this work and order of convergence results. 56

5.1 Summary of dissociation events for small He_xV_y clusters, and associate binding energies, as obtained from analysis of experimental THDS measurements [14] or theoretical modes [17, 18] 63

Acknowledgments

I could not have reached the final paragraph of this dissertation without the support of a large number of people over the course of my graduate studies at the University of California Berkeley.

First, I would like to thank my advisor, professor Brian D. Wirth, for his guidance over the long course of my project. More than his excellent professional and academic supervision, it has been his enthusiasm for research and encouragement along my studies which gave me the strength to persevere and finish my PhD.

I also want to pay my sincere respects to my dissertation committee. Professors Joonhong Ahn, Donald R. Olander and James A. Sethian taught me a lot inside and outside the classroom, and gave me insightful advice during my qualifying examination and dissertation completion.

I also deeply thank the Nuclear Engineering department staff for their help with any matter I encountered, and in particular Liza Zemelman for her guidance through all the administrative difficulties faced by foreign students at UC Berkeley.

I would like to thank Faiza Sefta for her indefectible support through all of my PhD. I had a great time in California and later Tennessee, and the presence of Faiza at my side was largely responsible for it.

Special thanks are given to my past and current colleagues in the Wirth research group. It was always a pleasure to meet these people at and outside work. In particular, I thank Dr. Donghua Xu, Niklas Juslin and Karl Hammond for their important advice.

I would also like to express my deepest gratitude to all the friends I met during my graduate years. I will miss the life in the bay area which was so enjoyable thanks to James Whitbeck, Sasha Prokhorova, Gabriel Meric, Raluca Scarlat, Nicolas Zweibaum, Kurt Terrani, Stephane Denerolle, Leonid Rozkin, Peter Allen, Matthieu Hursin, Ken Ogorzalek, Raphael Craplet, Minh Vu Hong, Wayland Chu, Iheb Triky, Ben Tom, Paul Cothenet, Lea Nehme, Ryan Shin, Pierre-Adrien Itty, Alex Kantchelian, Sofia Medina, Emilia Esposito, Denia Djokic, Sylvain and Anais Queyreau, Hubert Chaperon, Henri Faucher, Mickael Hajjar, and many others. I will also miss the club tennis team and all the great moments we had during our travels. I hope I will see all of them soon, whether it is in the US or on any other continent.

Finally, I want to thank my family for always being so supportive during these five years. It was only possible to come to UC Berkeley because of their encouragement, and there is no word to express how thankful I am.

Chapter 1

Introduction

1.1 The Need for Fusion Energy

The rapidly increasing world energy consumption, which is depicted in figure 1.1, presents several challenges for a path to sustainable development. Indeed, the vast majority of the energy consumed today comes from fossil fuels (oil, natural gas and coal) with a trend towards a growing share of fossil fuels consumption in the energy mix.

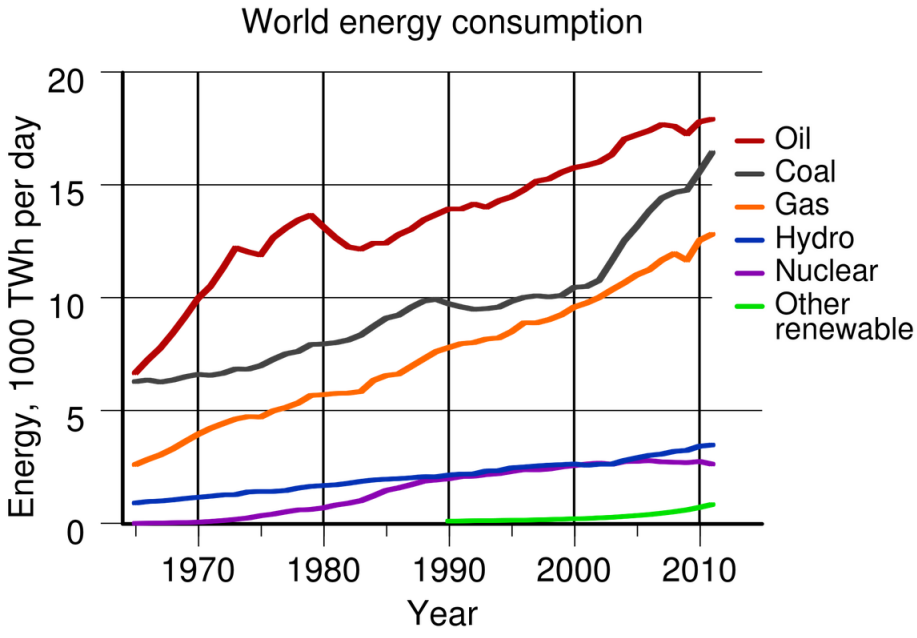


Figure 1.1: World Energy Consumption from 1965-2011, as reproduced from reference [1].

The situation for electricity generation depicted in figure 1.2 is very similar, with fossil fuels

representing the largest share in electricity consumption.

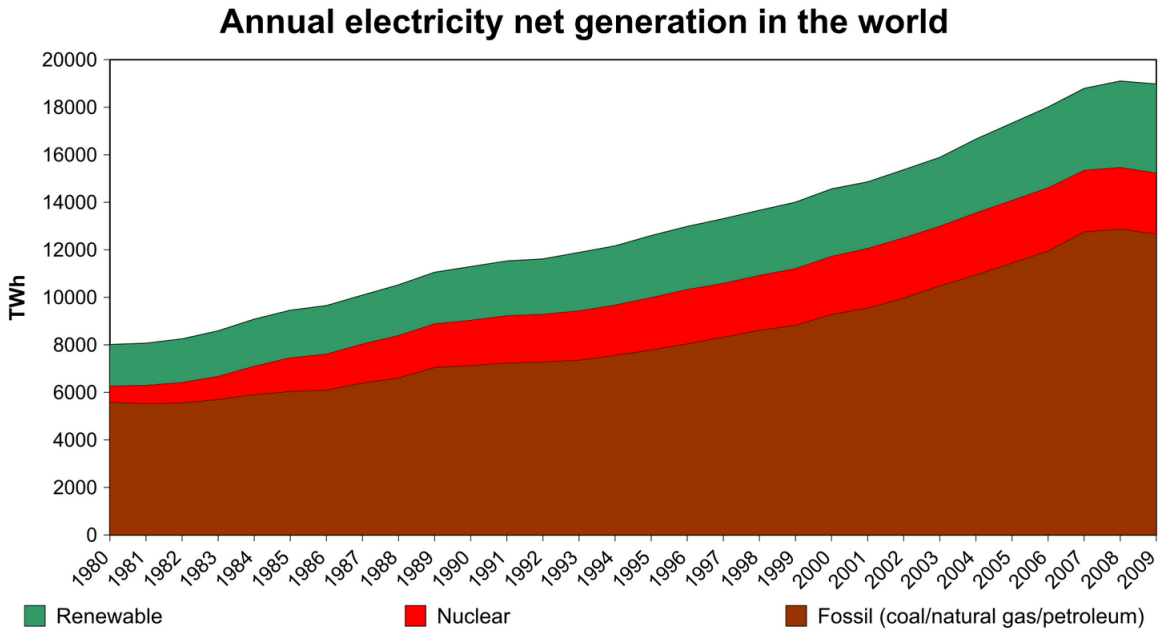


Figure 1.2: World Net Energy Generation from 1980-2009, as reproduced from reference [2].

Unfortunately, figure 1.3a shows that fossil fuels are largely responsible for greenhouse gas emissions worldwide and not surprisingly, these emissions drastically increased in the last 60 years as seen in figure 1.3b. The increase in Greenhouse gas emissions is largely believed to be the cause of recent climate change [19]. Moreover, fossil fuels are not renewable nor equally accessible to all countries, thus causing energy independence concerns. For these reasons, alternative energy sources need to be developed. While renewable energy sources and nuclear power are promising, they suffer from a variety of issues: intermittent production for renewable energies; and safety, proliferation, waste storage and general public acceptance issues for nuclear power.

Among energy sources under development, electricity production using fusion has the potential to mitigate all the previously mentioned issues. Two major branches of fusion energy research exist: Inertial Confinement Fusion (ICF), where nuclear fusion reactions are initiated by heating and compressing a fuel target using high-energy beams, and Magnetic Confinement Fusion (MCF), where magnetic fields confine the fusion fuel in the form of a plasma. This dissertation is focused on MCF, which is the approach being developed in the international research community.

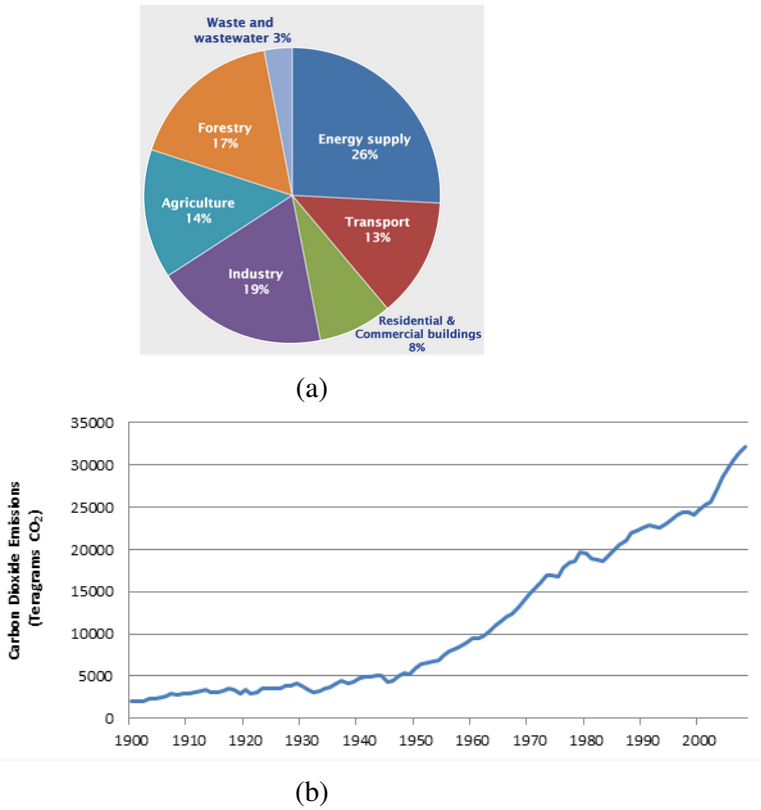


Figure 1.3: (a) Global Greenhouse Emissions by Sector and (b) Global CO_2 Emissions from 1980-2010, as reproduced from reference [3].

1.2 Magnetic Confinement Fusion

The idea behind electricity production through magnetic confinement fusion is relatively simple: A plasma, an ionized gas of particles, is created by heating and then confined using large magnetic coils. For sufficiently large temperature and pressure in the plasma, a nuclear fusion reaction occurs: a deuterium and a tritium particle collide to form an $\alpha-$particle and a neutron with excess energy. The $\alpha-$particle is then slowed down and eventually hits the divertor at low energy (E_i $\approx$ 100 eV), a component which acts as an exhaust system for the plasma. The neutron escapes the plasma due to its charge neutrality, goes through the first wall surrounding the plasma, and eventually hits the blanket module, designed to extract the neutron excess energy and pass it into the primary coolant, as well as breed tritium from lithium. This concept is being developed in ITER (International Thermonuclear Experimental Reactor), the world's largest tokamak currently being constructed in France under a large international cooperation effort which will eventually be capable of producing 1500 MW of fusion power.

Magnetic confinement fusion addresses the issues mentioned in the previous section:

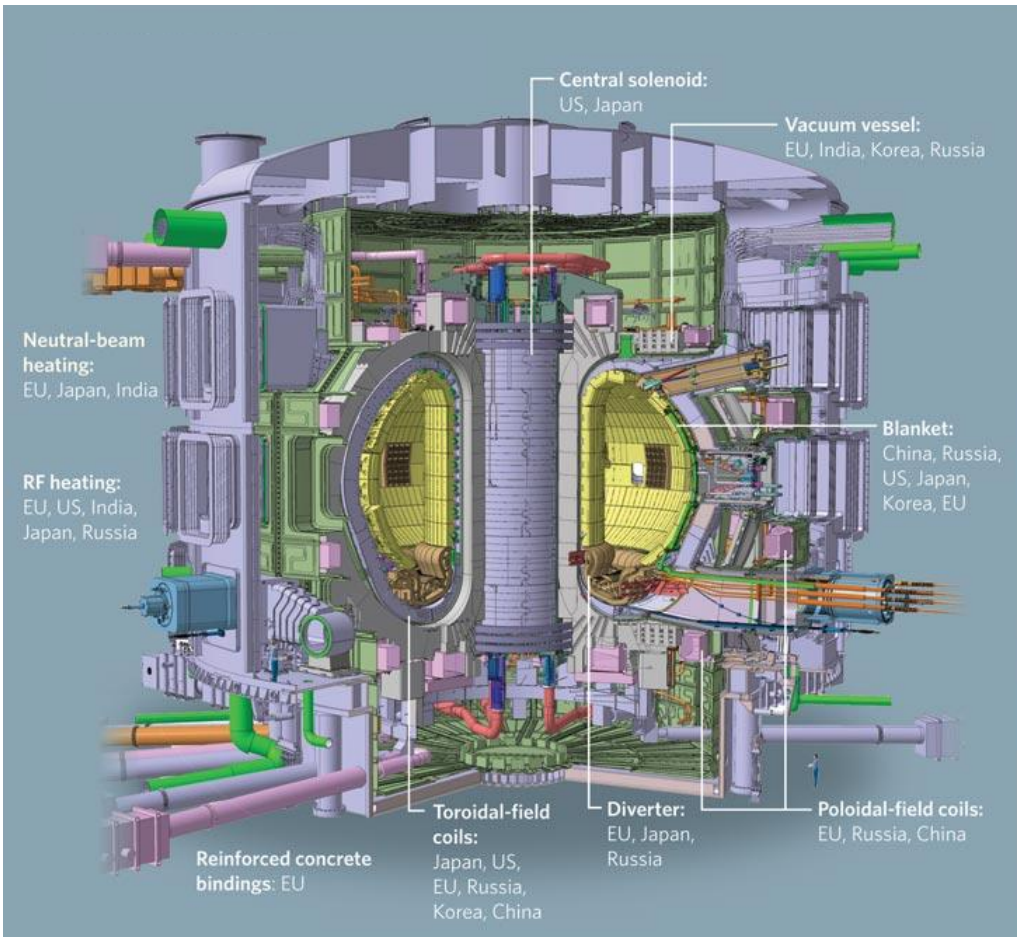


Figure 1.4: ITER schematic and origin of the main components, as reproduced from reference [4].

- No CO_2 will be directly emitted during operation of fusion power plants
- Fuel is abundant: deuterium can be extracted from water and tritium is directly bred in the reactor from lithium, which has large reserves, especially in South America.
- Radioactive waste produced during operation have a much smaller lifetime ($\sim$ 100 years) than fission reactors waste.
- Safety concerns are lower since any accidental event would typically lead to plasma disruption and end the fusion reaction within seconds. The risk of a runaway reaction leading to a catastrophic radioactive release event is therefore null.

1.3 Divertor Materials Challenges

The interactions between the edge of the plasma and the plasma facing components (PFCs) influence the core plasma performance: PFC materials have to sustain high heat loads ($\geq$ 20 MW/m^2) and particle fluxes ($\geq 10^{22}$ m$^{-2}s^{-1}$ for the divertor) at high temperatures ($\geq$ 1000 K). These extreme conditions create a variety of complex materials challenges: PFCs mainly need to resist plasma erosion in order to prevent impurities from poisoning the core plasma. Particle deposition onto PFCs alter their surface composition and can lead to enhanced erosion as well as enhanced tritium retention which can limit the reactor lifetime. Therefore, a complete understanding of plasma-materials interactions is essential to predict materials response and develop appropriate solutions.
The divertor is a key plasma facing component: it lies at the intersection of the magnetic field lines and is therefore subject to the highest fluxes of plasma particles. In particular, Helium exposure with fluxes up to 10^{23} $m^{-2}s^{-1}$ and temperatures between 1000 and 2000 Kelvins are expected in fusion reactors such as ITER [8]. These severe operating conditions pose new material challenges. Among materials investigated for the divertor, tungsten is one of the most promising due to its high melting temperature and low erosion rate. However, little understanding exists of the behavior of helium in tungsten under these operating conditions.

Several issues associated with tungsten under helium exposure have been experimentally observed, due to the low solubility and high diffusivity of helium in tungsten and therefore its ability to diffuse to nucleation sites (impurities, pre-existing defects or defects resulting from irradiation such as vacancies, self-trapped helium atoms) and form large gas bubbles. These issues include:

- Blistering and flaking: Figure 1.6 shows the surface morphology changes due to high energy (1.3 MeV) helium irradiation of tungsten at high temperature (850°C) [6]. Large blister caps form for low irradiation fluences (Figures 1.6a and 1.6b) and significant surface morphology changes occur at high fluences (1.6c) . This phenomenon is caused by helium trapping in vacancies and cavities (large vacancy clusters) produced by displacement cascades due to high energy irradiation. These gas bubbles grow due to continuous irradiation and diffusion of helium into these cavities and eventually burst at the surface at high fluences. This could lead to increased erosion of tungsten and reduction of the tungsten performances and lifetime.

- Changes in tritium retention: tritium, an isotope of hydrogen and a reactant in the fusion reaction, slowly contaminates the PFCs when leaking from the plasma. Since tritium is a radioactive element, it is necessary to quantify the tritium concentration in the PFCs. This tritium inventory can ultimately lead to the end of operation of the PFCs when it reaches a safety value fixed to protect fusion power plant workers. Figure 1.7 shows the effect of helium irradiation on the hydrogen retention properties of tungsten [7]. We see that following pre-irradiation of helium at room temperature (Figure 1.7a), hydrogen retention properties are greatly altered. A greater amount of hydrogen is released at lower temperatures, but the overall hydrogen retention remains similar. However, post-irradiation of helium (Figure

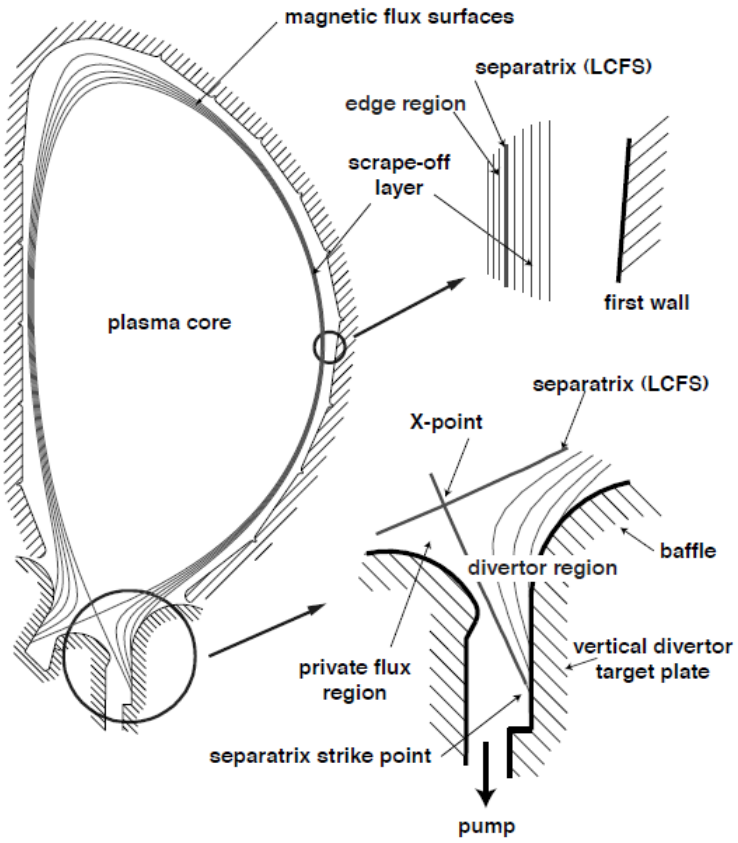
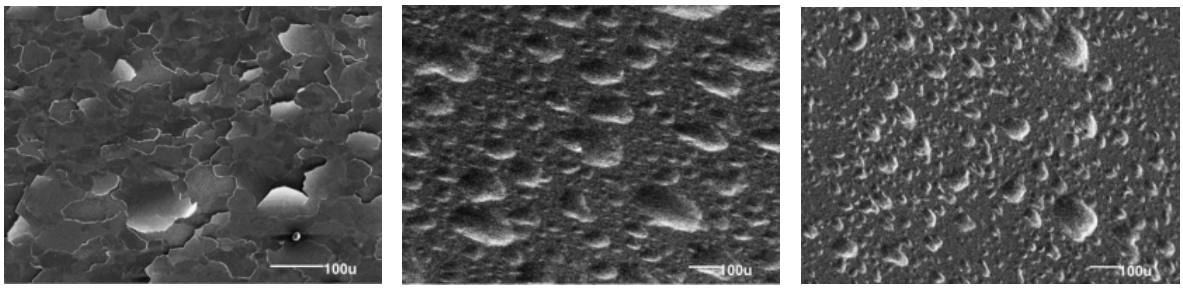


Figure 1.5: Poloidal cross-section of a tokamak plasma, as reproduced from reference [5].

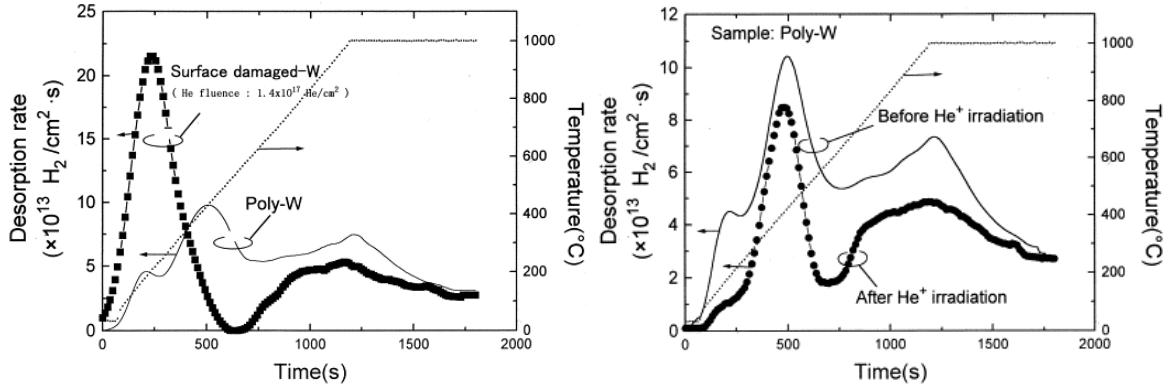
1.7b) reduces the overall amount of helium released by about 50%, which could lead to a much smaller lifetime of PFC materials in fusion reactors.

- Tungsten "nano-fuzz" formation: under fusion relevant conditions, incident helium ions on the divertor are expected to penetrate the tungsten surface without producing any damage due to their low incident energy ($E_i \leq 100$ eV). However, several recent experimental studies report a phenomenon described as "nano-fuzz" formation, corresponding to the growth of a thin layer of low density tungsten packed with helium bubbles [8, 20, 21, 22, 23]. Figure 1.8 depicts the evolution and growth of fuzz under helium irradiation [8]. The mechanisms leading to fuzz formation are not known yet, but it is expected that the high flux and high helium diffusivity at high temperatures under fusion relevant conditions lead to self-trapping of helium atoms or trapping at impurity sites. These small clusters then act as nucleation sites, attracting mobile helium atoms to form larger and larger nanometer-sized helium-vacancy clusters. The resulting large concentration of nanometer-sized gas bubbles causes significant surface morphology changes, due to bubble growth, bubble coalescence events and bursting



(a) 10^{22} He/m^2 (b) 2×10^{21} He/m^2 (c) 10^{21} He/m^2

Figure 1.6: SEM images of polycristalline tungsten following 1.3 MeV He implantation to a fluence of (a) 10^{22} He/m^2 , (b) 2×10^{21} He/m^2, (c) 10^{21} He/m^2 at 850°C and then flash heated at 2000°C, as reproduced from reference [6].



(a) (b)

Figure 1.7: Thermal hydrogen desorption results with a temperature ramp of 50 K/min. (a) The tungsten material was first irradiated at room temperature with 5 keV helium up to a fluence of 1.4×10^{21} He/m^2, followed by 1.7 keV H up to a fluence of 5×10^{22} H/m^2. (b) The tungsten material was first irradiated at room temperature with 1.7 keV H up to a fluence of 5×10^{22} H/m^2, followed by 5 keV helium up to a fluence of 1.4×10^{21} He/m^2. Figures reproduced from reference [7].

events at the surface. This nano-fuzz can ultimately lead to an alteration of the tungsten properties (thermal conductivity, erosion rate) which can drastically reduce the lifetime of the divertor.

1.4 Dissertation Objectives and Outline

The issues mentioned above indicate that it is crucial to develop an understanding of the microstructure evolution of helium-irradiated tungsten under fusion relevant conditions, which is the

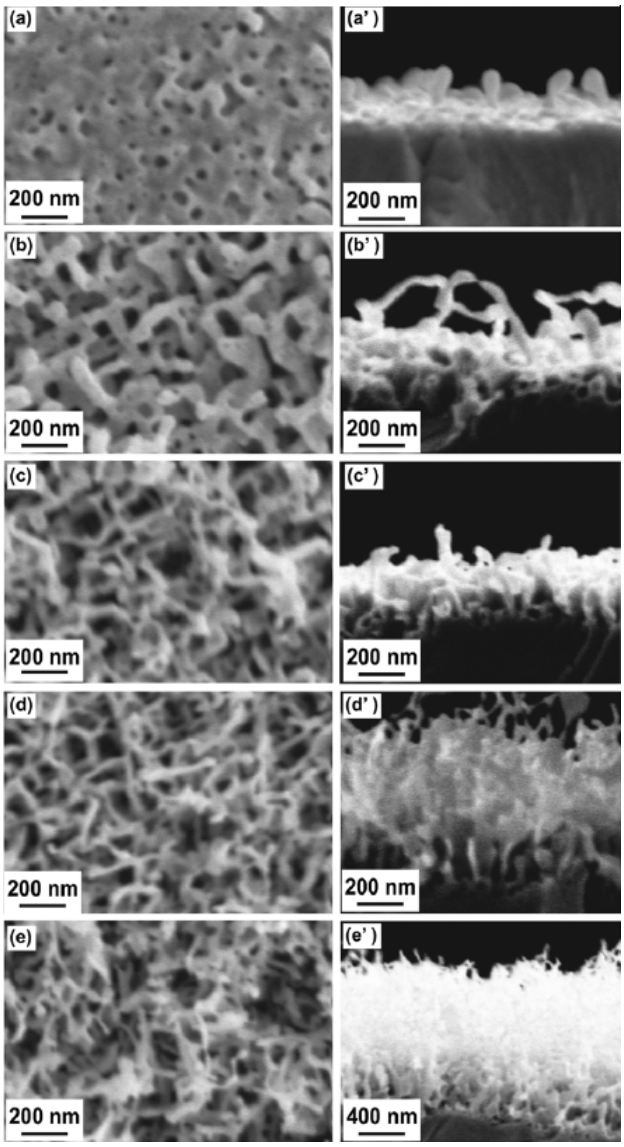


Figure 1.8: SEM micrographs of tungsten surface after 50 eV helium irradiation at 1400 K up to a fluence of (a) 6×10^{24} He/m^2, (b) 1.1×10^{25} He/m^2, (c) 1.8×10^{25} He/m^2, (d) 2.4×10^{25} He/m^2, (e) 5.5×10^{25} He/m^2, as reproduced from reference [8].

objective of this dissertation. The main challenge in modeling the changes in the tungsten material is the large span of time and length scales associated with the different mechanisms in play, from the diffusion of helium interstitial atoms to the growth of nanometer-sized gas bubbles. Since not one computational materials approach can simulate material evolution from the atomistic scale to the macroscopic scale, a combination of methods through increasingly coarser time and length scales is needed. Figure 1.9 illustrates the sequence of models that investigate material behavior from the quantum to the continuum level. The modeling tools at our disposal reflect this large

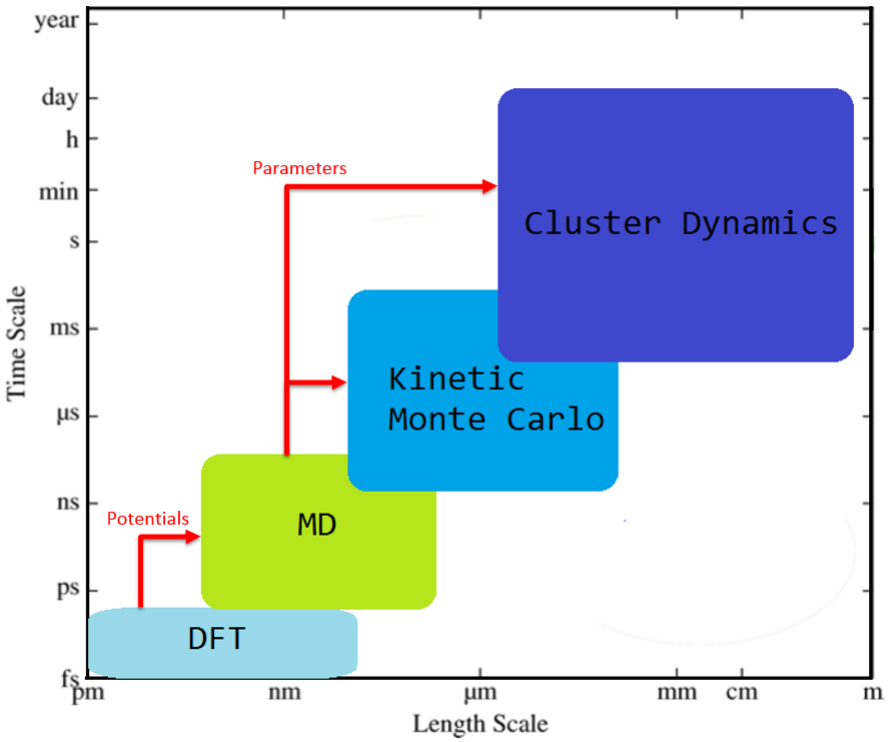


Figure 1.9: Multi-scale computational materials modeling

range of phenomena:

- **Density functional theory (DFT):** DFT is a quantum mechanical modeling method used to investigate the electronic structure of many-body systems, including condensed phases. It simplifies the many-body Schrödinger equation by describing the electrons with a density function. DFT simulations are of interest to us since they can accurately determine the energy of a system of atoms. Due to the accurate description of the interactions between atoms, DFT simulations are however limited to very small systems, typically less than 500 atoms.

- **Molecular Dynamics (MD):** MD is a computer simulation of the physical movement, or trajectory, of atoms. The principle is simple: MD solves Newton's equations of motion to simulate the trajectory of each atom in the system. MD allows both visualization of molecular motion at the atomic scale and the determination of macroscopic thermodynamical properties of the system (energy, temperature, pressure). A potential function is used to determine the interactions between atoms, which is determined semi-empirically from DFT and experimental data. MD simulations have relatively short time (< 1 microsecond) and length (< 100 nm) scales.

- **Kinetic Monte Carlo (KMC):** KMC are a class of stochastic models intended to simulate

the time evolution of objects according to selected processes. The possible processes are an input to the model, which at each time computes the rates of each of these possible processes, selects stochastically one of these (in general using an algorithm known as the resident time algorithm) and updates the objects and simulation time accordingly. Depending on what the objects are and which processes are considered, the length and time scales can vary greatly. In Lattice Kinetic Monte Carlo (LKMC), the objects are the individual atoms and the processes are the jumps of these atoms from one lattice site to another. Hence, the time and length scales are only slightly larger than the Molecular Dynamics ones. In Object Kinetic Monte Carlo (OKMC) on the other hand, the objects are only defects or defect clusters and the underlying lattice atoms are not taken into account. The processes are typically the diffusion of these objects and a series of predefined reactions between them. The time and length scales are larger but are limited by the number of species in the simulation box. Recently, an OKMC model simulating helium irradiation of tungsten reached large times ($\sim$ seconds) for a relatively low length scale ($\sim 1\ \mu m$) and implantation flux (10^{15} Hem^{-2}s^{-1}) [24, 11].

- **Continuum models:** Continuum models ignore the underlying lattice structure of the materials and, as indicated, treat it as a continuum. It only models the fate of specific objects evolving in that continuum. In this work, we will extensively use a continuum model called **Cluster Dynamics** (CD), which simulates the evolution of the materials microstructure. CD predicts the concentration of every type of defects in the material for large time ($\sim$ hours) and length ($\sim$ cm) scales that are more experimentally relevant, regardless of the number of defects in the material. Cluster Dynamics modeling is based on the reaction-diffusion equations and has been successfully applied to a variety of situations in past years [25, 26, 27, 28, 29, 30, 31].

Since the different physical processes occur over such a large range of time and length scales, this dissertation uses a multi-scale approach: we will perform simulations and use results of several of the tools presented above. The results of the lowest scales models can then be used as inputs for the parameters of the largest scale models. In particular, we perform molecular dynamics simulations to identify the atomistic physical processes involved in the microstructure evolution of helium-irradiated tungsten and determine the corresponding parameters. Then, we present a cluster dynamics code built to model these physical processes over a large spatial domain and period of time. The results of this code can then be compared to experimental results. The outline of this dissertation is therefore the following:

- **Chapter 2 - Cluster Dynamics Model:** This chapter introduces the cluster dynamics framework at the core of this dissertation. Insights from experiments, molecular dynamics and density functional theory are used to identify the relevant physical processes. The cluster dynamics equations are presented with a detailed list of parameters and assumptions.

- **Chapter 3 - Molecular Dynamics for Parameter Estimation:** This chapter presents the results of molecular dynamics simulations to determine the input parameters for the cluster

dynamics model. We compare the results with available DFT and experimental data, and present the resulting set of parameters used throughout this work.

- **Chapter 4 - Cluster Dynamics Solver:** This chapter focuses on the numerical analysis of the cluster dynamics equations and introduces the tools developed to solve this large system of non-linear partial differential equations.

- **Chapter 5 - Cluster Dynamics Model validation:** This chapter presents the results of the cluster dynamics code in two specific cases: first, results for helium irradiation at low fluxes and fluences on a heavy-ion irradiated tungsten material are presented. The range of species to consider and therefore parameters relevant under these conditions being more narrow, we can compare the numerical results to available experimental results as a first validation of the model. Second, results for helium irradiation similar to molecular dynamics conditions are introduced and compared to the molecular dynamics simulations, which allow us to determine potential issues encountered under fusion relevant conditions.

- **Chapter 6 - Cluster Dynamics Results under Fusion Relevant Conditions:** This chapter presents the results of the cluster dynamics code under fusion relevant conditions. We compare numerical results with experimental results as well as results from an analytical model based on the cluster dynamics equations.

Chapter 2

Cluster Dynamics Model

2.1 Introduction

Continuum models are useful to predict the behavior of tungsten microstructure evolution for the longest time scales ($\geq$ days) and largest length scales ($\geq$ meters). In this chapter, we introduce the cluster dynamics model, which aims to predict the evolution in space and time of different types of clusters of atoms in the tungsten material. The type of clusters to consider and the physical processes they can undergo is dictated by insights from experiments and molecular dynamics simulations. The objective of this chapter is then to lay out the cluster dynamics framework, including the notations, physical processes being described, equations and assumptions.

2.2 Insight from Experiments and Molecular Dynamic Simulations

There is a large body of experimental and theoretical work on the behaviour of helium in tungsten. Helium atoms diffuse in tungsten by the interstitial mechanism from tetrahedral to tetrahedral interstitial sites [32]. Due to their high mobility, helium atoms then react with other helium atoms, vacancies or self-interstitial atoms to form clusters. Each of these clusters have specific properties: size, mobility, binding energies with respect to various dissociation reactions, and other clusters they can interact with. Experiments confirm the wide range of these properties depending on the type of clusters considered [33, 34, 35, 14].
We can visualize this specific behavior of various clusters of atoms using molecular dynamics simulations. Figure 2.1 shows the results of a molecular dynamics simulation in tungsten at 500 Kelvin at different simulation times. Details on molecular dynamics simulations performed in this work (algorithm, potentials, boundary conditions) will be given in chapter 3. In this simulation, helium atoms are inserted at a random position in the $30 \times 30 \times 30\ a_0$ simulation box every 100 ps. The blue spheres represent the helium atoms, the yellow spheres the self-interstitial (SIA) and the red spheres the vacancies. We observe that helium intersitial atoms diffuse from their initial point

of insertion. Whenever two helium atoms come in close proximity, they react with each other to form a di-helium cluster which keeps diffusing. This process continually repeats with other helium atoms to form larger and larger helium interstitial clusters. We observe that large helium interstitial clusters diffuse slower than smaller ones. We also observe that a single helium can be emitted from a large helum intersititial cluster and diffuse freely away from it. Lastly, we observe that when a helium interstitial cluster reaches a critical size of about 6 atoms in this simulation, it becomes immobile. If an additional helium atom reacts with this cluster, then a self-interstitial tungsten atom is emitted which relieves the stress, and the helium-interstitial cluster remains immobile in the resulting vacant lattice site, a process known as trap mutation. These insights from experiments and molecular dynamics simulations show that our model needs to capture important properties to accurately describe the evolution of the microstructure of tungsten: diffusion, reactions between helium and helium-defects clusters, dissociation of helium clusters, and trap mutation events. The model also needs to reflect that these properties are different for each type of cluster of atoms considered.

2.3 Objective and Notation

Cluster dynamics is a continuum model focusing on predicting the evolution in space and time of the population of foreign species in the tungsten material: We define the term species to include any unique combination of atoms or defects grouping to form a cluster in the material. The species considered in our model are interstitial helium atoms (denoted as He_1) and clusters of helium atoms (He_x, $x \geq 2$), single vacancies (V_1) and clusters or vacancies (V_y, $y \geq 2$, also called voids), single self-interstitial tungsten atoms (I_1 or SIA) and clusters of self-interstitial atoms (I_z, $z \geq 2$, also called interstitial loops), and helium-vacancy clusters (He_xV_y, $x \geq 1$, $y \geq 1$, also called gas bubbles when they reach a size of several nanometers). We do not consider helium-interstitial clusters or helium-vacancy-interstitial cluster in this work: although they appear to play a role in iron materials, there is no experimental evidence to confirm the existence of these clusters in tungsten, and little simulation work has been performed to investigate these possible clusters. Each individual species has specific physical properties (such as diffusion coefficient, binding energies and capture radius) and is therefore treated separately. Cluster dynamics is a continuum model and therefore does not consider the motion of individual species in the materials such as is done by Kinetic Monte-Carlo models [24, 11]. Instead, the evolution of the concentration of each species is computed as a function of time and position. Therefore, the physical processes mentioned above (diffusion, reaction and dissociation events) are modeled in a continuum sense which leads to a physical system described by partial differential equations. For any species i, the typical equation

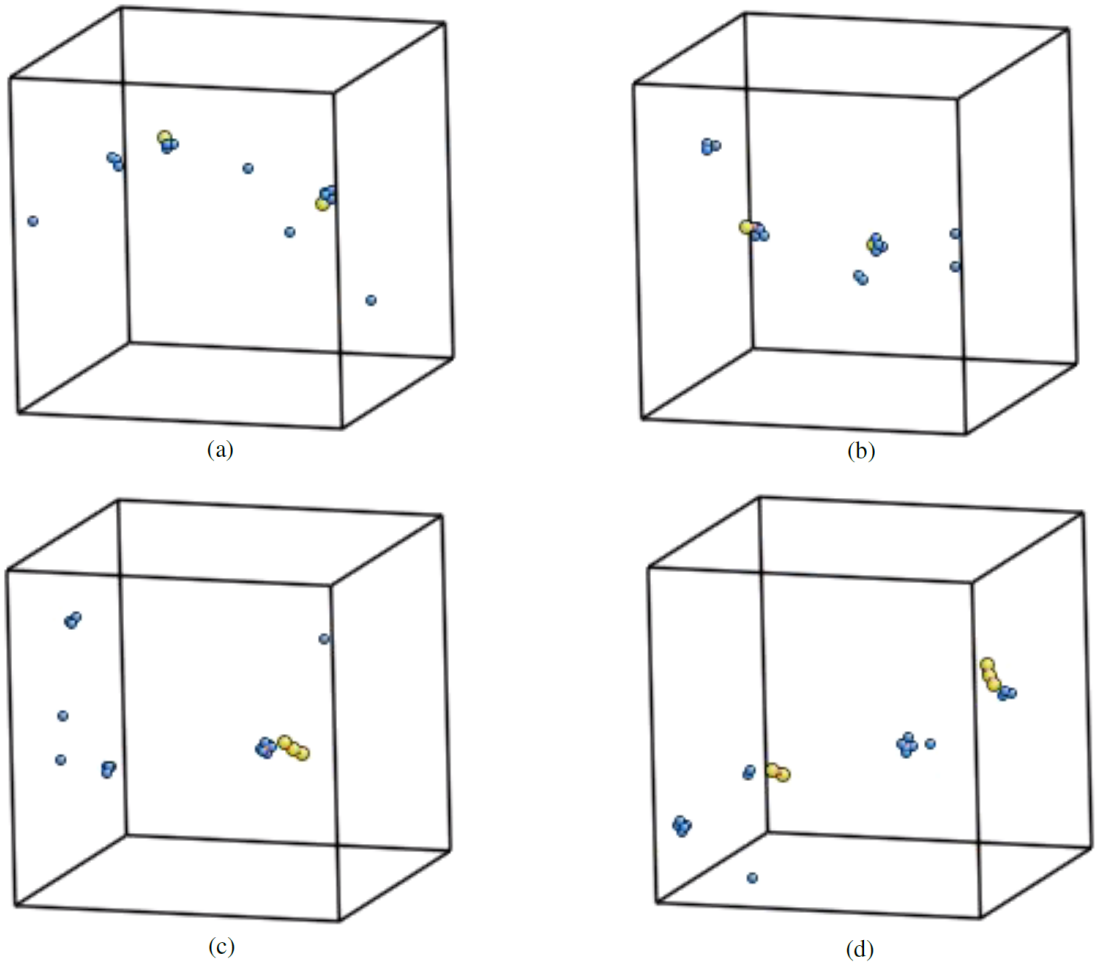


Figure 2.1: MD simulation results for a $30 \times 30 \times 30$ a_0 tungsten box at 500 Kelvin with a helium atom inserted at a random position every 100 ps. (a) time = 500 ps. Helium atoms diffuse and react to form small diffusing helium interstitial clusters. (b) time = 1 ns. Larger helium interstitial clusters are formed. The largest ones are immobile. (c) time = 1.5 ns. A SIA was emitted from a large helium interstitial clusters which sits in the remaining vacancy. (d) time = 2ns. The SIA diffused towards another helium-vacancy cluster in formation.

describing the evolution of its concentration $C_i(\vec{r},t)$ is then:

$$\begin{aligned}\frac{\partial C_i}{\partial t}(\vec{r},t) &= Diffusion_i(C_i,\vec{r},t) \\ &+ Source_i(\vec{r}) \\ &+ Reaction_i(C_1(\vec{r},t),...,C_N(\vec{r},t)) \\ &+ Dissociation_i(C_1(\vec{r},t),...,C_N(\vec{r},t))\end{aligned} \tag{2.1}$$

Each of the right hand side terms in equation 2.1 corresponds to a separate physical process.

2.4 Description of the Physical Processes

2.4.1 Diffusion

At the continuum level, the diffusion term is due to a concentration gradient in the species considered (we will see in chapter 3 a more detailed description of the diffusion process and how we can compute the diffusion coefficient from molecular dynamics simulations). Since we explicitly model the interactions between species in the reaction and the diffusion term, the diffusion term for each species only depends on the concentration gradient of the species itself and not on the concentrations of other species. If D_i denotes the diffusion coefficient of species i, we can use Fick's first and second laws to obtain the diffusion term:

$$\frac{\partial C_i}{\partial t}(\vec{r},t) = Diffusion_i(C_i,\vec{r},t) = D_i \nabla C_i(\vec{r},t) \tag{2.2}$$

In this dissertation, we are concerned about the depth dependence of the concentration of each species under the materials surface. Due to the symmetry in the directions parallel to the surface and perpendicular to the irradiation flux, we only consider the dependence in the x-coordinate which refers to the direction perpendicular to the surface. Therefore, our model becomes one-dimensional and the diffusion term is:

$$\frac{\partial C_i}{\partial t}(x,t) = D_i \frac{\partial^2 C_i(x,t)}{\partial x^2} \tag{2.3}$$

Molecular dynamics simulations results show that He_xV_y and V_y species are immobile during the time scale of the simulations. Since the He_xV_y represent the majority of the species considered, this has important implications in the solver, as our system becomes a coupled ODE-PDE system. We will see in chapter 4 how we can take advantage of the fact that only a small subset of species are mobile in order to efficiently solve the cluster dynamics equations.
Extension of the model to two or three dimensions to include the effects of grain boundaries or specific geometries (such as the tendril geometry in chapter 6) is possible, but has not been implemented in this work.

2.4.2 Clustering Reactions

The reaction term is obtained from chemical reaction theory. Consider an idealized system consisting of only two components A and B, which can react with a forward reaction constant $k^+_{A,B}$:

$$A + B \xrightarrow{k^+_{A,B}} AB \tag{2.4}$$

If we consider the reaction to be first order, that is, the species react directly to form the product in a single reaction step, then the production rate of species AB is given by

$$\frac{\partial C_{AB}}{\partial t} = -\frac{\partial C_A}{\partial t} = -\frac{\partial C_B}{\partial t} = k^+_{A,B} C_A C_B \tag{2.5}$$

The value of the forward reaction constant $k^+_{A,B}$ can be determined using the theory of diffusion limited reactions [36]. Two main assumptions are used to derive the value of the reaction rate constant:

- Species A and B are assumed to be randomly uniformly distributed. This assumption implies that the cluster dynamics model does not take into account spatial correlation. This has two consequences: first, since species produced in damage events such as displacement cascades in the case of heavy ion irradiation (such as vacancies and interstitial clusters) are highly spatially correlated, the source term in the cluster dynamics equations can not directly reflect the species produced at the peak of the displacement cascade. Hence, we will need to take care in determining the source term for each species for damage events. Second, we need to remain in the dilute limit: The volume occupied by the species must remain small compared to the volume of the surrounding tungsten matrix. If V_f denotes the total volume fraction of the species, we need $V_f \ll 1$ at all times. We will see in chapter 6 that helium implantation under fusion relevant conditions can lead to the dilute limit approximation breakdown.

- Species A and B are assumed to react instantaneously when they are within a certain distance of each other. This is known as a diffusion-limited reaction, since the rate of transport of the reactants through the tungsten matrix is the limiting step in the reaction and not the rate of formation of the product. The reaction distance is the sum of the reaction radius of each species r_A and r_B, which is the distance from the defect inside which the lattice experiences a significant strain field. This parameter will be described in more details in chapter 3.

Under these assumptions, the forward reaction rate is described as:

$$k^+_{A,B} = 4\pi(r_A + r_B)(D_A + D_B) \tag{2.6}$$

note that immobile species ($D_i = 0$) can not react with other immobile species, which results from the assumption that there is no spatial correlation between species. Therefore, when the dilute limit breaks down ($V_f \sim 1$), events such as bubble coalescence (two large He_xV_y clusters nearby merge into a larger one) are expected to take place and the current model would fail. Table 2.1

shows all the different types of reactions considered in the model. For a given species i, the value of $Reaction_i(C_1(\vec{r},t),...,C_N(\vec{r},t))$ depends on the type of species i since the possible reactions differ between species types. We will give the expression of this term in the complete equations below.

Table 2.1: List of possible clustering reactions considered in this model.

Reaction	Formula	Comment
Helium clustering	$He_x + He_y \rightarrow He_{x+y}$	Only possible for small clusters ($x+y<10$) due to trap mutation
Vacancy clustering	$V_x + V_y \rightarrow V_{x+y}$	Di-vacancy stable with MD data, not stable with DFT data
Interstitial clustering	$I_x + I_y \rightarrow I_{x+y}$	Interstitial concentration remains neglictible for low energy irradiation
Interstitial-Vacancy annihilation	$I_x + V_y \rightarrow \begin{cases} I_{x-y} & \text{if } x>y \\ V_{y-x} & \text{if } x<y \\ \varnothing & \text{if } x=y \end{cases}$	
Helium Vacancy clustering	$He_x + V_y \rightarrow He_xV_y$	
He/V cluster growth through helium absorption	$He_xV_y + He_z \rightarrow He_{x+z}V_y$	
He/V cluster growth through single vacancy absorption	$He_xV_y + V \rightarrow He_xV_{y+1}$	
He/V cluster reduction through interstitial absorption	$He_xV_y + I_z \rightarrow He_xV_{y-z}$	

2.4.3 Dissociation Events

Clusters of atoms and point defects can also dissociate into smaller fragments. Let us consider the reverse reaction from the previous section:

$$AB \xrightarrow{k^-_{AB\rightarrow A+B}} A + B \tag{2.7}$$

The backward reaction constant $k^-_{AB}(AB \rightarrow A + B)$ can be determined using chemical equilibrium principles [37]. The diffusion-limited reaction approximation gives an approximation to the forward reaction rate and at equilibrium, the forward and backward reaction rates are equal:

$$k^-_{AB} = k^+_{AB}\frac{C_{A_{eq}}C_{B_{eq}}}{C_{AB_{eq}}} = \frac{1}{\Omega}k^+_{AB}e^{-\frac{\Delta G^0}{k_bT}} = \frac{1}{\Omega}k^+_{AB}e^{-\frac{E_b(AB\rightarrow A+B)}{k_bT}} \tag{2.8}$$

where Ω is the atomic volume, ΔG^0 is the change in Gibbs free energy in the reaction, also called binding energy, k_b is the Boltzmann constant, and T is the temperature. Chapter 3 explains how to determine the binding energy for a given reaction using molecular dynamics simulations.
We need to describe the reaction we refer to in the backward reaction constant $k^-_{AB\rightarrow A+B}$ since a given species can undergo several different types of dissociation events. These dissociation events are of two different types: single species dissociation and trap mutation events. As observed in molecular dynamics simulations, we assume that only mobile point defects and single helium interstitials can dissociate from a cluster. The backward reaction constants for helium and point defect dissociation are denoted respectively by k^{-He} and k^{-PD}. However, there also exists a special class of dissociation events that we call trap mutation. An over-pressurized helium or helium-vacancy cluster ejects a surrounding tungsten atom to expand and stabilize:

$$He_x \rightarrow He_xV + I \tag{2.9}$$
$$He_xV_y \rightarrow He_xV_{y+1} + I \tag{2.10}$$

The tungsten self-interstitial atom formed is free to diffuse towards the free surface or react with another species. Trap mutation is an important phenomenon as we will see in chapter 6 since it explains how irradiation of tungsten with low energy incident ions (thus producing no direct damage) at high fluxes causes the formation of large gas bubbles under the material. The backward dissociation constant for trap mutation is denoted by k^{-TM}. Table 2.2 shows the different types of dissociation events considered in the model.

Table 2.2: List of possible dissociation reactions considered in this model.

Dissociation Reaction	Formula	Comment
Helium dissociation	$He_xV_y \rightarrow He_{x-1}V_y + He$	Single He dissociates from cluster
Vacancy dissociation	$He_xV_y \rightarrow He_xV_{y-1} + V$	Single vacancy dissociates from cluster
Trap mutation	$He_xV_y \rightarrow He_xV_{y+1} + I$	High pressure He/V cluster eject a lattice atom to create a single interstitial

2.4.4 Source term

The source term comes from the direct production of species in the material due to the irradiation or implantation flux. These species are the implanted helium atoms of course, but also the point defects and their clusters produced due to displacement cascades caused by scattering of incoming ions with the tungsten atoms on the lattice in the case of high energy particle irradiation. As mentioned above, the cluster dynamics model assumes no spatial correlation between species, even though point defects produced by irradiation are highly spatially correlated. Therefore, we need to take into account the very fast recombination between interstitials and vacancies produced by irradiation due to their spatial correlation. The program SRIM [9] provides a reasonably accurate prediction of the implanted helium range and the primary knock-on atoms (PKA) depth and energy distribution. However, SRIM does not take into account instant clustering of point defects. We therefore use additional molecular dynamics simulations of the relevant PKA energies to estimate the actual number of point defects and clusters of point defects created within the initial damage production, and use cluster dynamics to model the subsequent diffusive evolution.

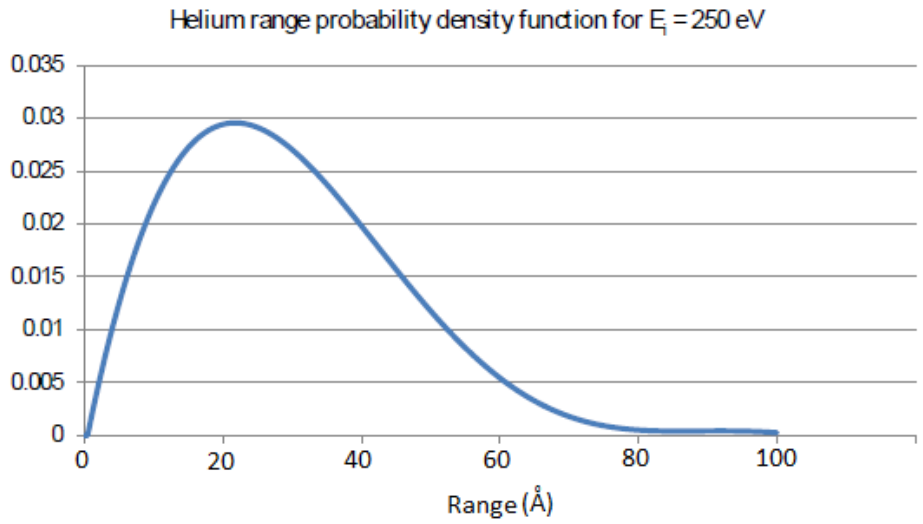


Figure 2.2: Range of 250 eV helium in Tungsten as calculated by SRIM [9].

2.4.5 Boundary Conditions

In order to completely describe our physical system, we need boundary conditions for the diffusive species. Since vacancies and interstitials simply vanish at the surface (they become part of the regular lattice again) and helium atoms desorb from the material, the boundary condition for each species i are simply:

$$C_i(x = 0, t) = C_i(x = L, t) = 0 \tag{2.11}$$

where L is the thickness of the tungsten material. A surface with such boundary conditions is called a free surface.

2.5 Equations

Before writing the cluster dynamics equations, we need a few more notations about the size of the system: if in theory clusters can always grow larger through reaction with other species and trap mutation events, in practice we only consider a limited number of species. We denote by y_M the maximum number of vacancies in a helium-vacancy cluster, and z_M the maximum number of interstitials in an interstitial cluster. We could denote by x_M the maximum number of helium in a helium-vacancy cluster regardless of the number of vacancies (which would give a total number of species $N = (x_M + 1) \times (y_M + 1) + z_M - 1$), but that would greatly overestimate the number of species considered. The maximum number of helium in a helium-vacancy cluster actually depends on the number of vacancies: for a given void, we can only fit a certain number of helium in it before the gas bubble becomes too over-pressurized and a trap mutation event instantaneously occurs to stabilize the system (even at 0 K). The exact number of helium $x_M(y)$ that can be contained in a helium-vacancy cluster with y vacancies will be discussed in chapter 3.
We can now write down the complete cluster dynamics equations for each type of species i with diffusion coefficient D_i, source term S_i and reaction and dissociation events listed in tables 2.1 and 2.2. The equations are different depending on the type of the species considered (single species, clusters, immobile species), so we give the equations for each group of species.
The PDE describing the evolution of the concentration of a single helium species He_1 is:

$$\begin{aligned}
\frac{\partial C_{He_1}}{\partial t} &= D_{He_1}\frac{\partial^2 C_{He_1}}{\partial x^2} + S_{He_1} \\
&- k^+_{He_1,He_1}C^2_{He_1} - C_{He_1}\sum_{j=0}^{y_M}\sum_{i=0}^{x_M(j)-1} k^+_{He_1,He_iV_j}C_{He_iV_j} + \sum_{j=1}^{y_M} k^+_{He_1V_j,I_j}C_{He_1V_j}C_{I_j} \\
&+ 2 \times k^{-He}_{He_2}C_{He_2} + \sum_{i=3}^{x_M(0)} k^{-He}_{He_i}C_{He_i} + \sum_{j=1}^{y_M}\sum_{i=1}^{x_M(y)} k^{-He}_{He_iV_j}C_{He_iV_j} \\
&+ k^{-He}_{He_1V_1}C_{He_1V_1} \\
&- k^{-TM}_{He_1}C_{He_1}
\end{aligned} \tag{2.12}$$

For clarity for the reader, we can describe the terms of this equation as an example. $\frac{\partial C_{He_1}}{\partial t}$ represents the rate of change in the concentration due to the effects of the combined physical processes, $D_{He_1}\frac{\partial^2 C_{He_1}}{\partial x^2}$ represents the change due to the diffusion process and S_{He_1} is the source term due to direct irradiation of helium ions. $k^+_{He_1,He_1}C^2_{He_1}$ and $-C_{He_1}\sum_{j=0}^{y_M}\sum_{i=0}^{x_M(y)-1} k^+_{He_1,He_iV_j}C_{He_iV_j}$ represent the loss due to the reaction of single helium with itself or other species ($He_1 + He_iV_j \rightarrow He_{i+1}V_j$).

$\sum_{j=1}^{y_M} k^{+}_{He_1V_j,I_j} C_{He_1V_j} C_{I_j}$ represents the production of helium due to the reaction of self-interstitial atom clusters with helium-vacancy clusters such that the interstitial atoms clusters and the vacancies annihilate each other to form a resulting single helium ($He_1V_j + I_j \rightarrow He_1$). The large term $2 \times k^{-He}_{He_2} C_{He_2} + \sum_{i=3}^{x_M(0)} k^{-He}_{He_i} C_{He_i} + \sum_{j=1}^{y_M} \sum_{i=1}^{x_M(y)} k^{-He}_{He_iV_j} C_{He_iV_j}$ is simply the production of single helium due to all the species which can eject a single helium ($He_iV_j \rightarrow He_{i-1}V_j + He_1$), the term $k^{-V}_{He_1V_1} C_{He_1V_1}$ is the production of single helium due to the dissociation of a vacancy from a He_1V_1 cluster ($He_1V_1 \rightarrow He_1 + V_1$), and finally the term $-k^{-TM}_{He_1} C_{He_1}$ represents the (unlikely) event of a trap mutation phenomenon involving a single helium species ejecting a self-interstitial tungstem atom to form a HeV cluster and stabilize ($He_1 \rightarrow He_1V_1 + I$).
The PDE describing the evolution of the concentration of a single vacancy species V_1 is:

$$\begin{aligned}
\frac{\partial C_{V_1}}{\partial t} &= D_{V_1} \frac{\partial^2 C_{V_1}}{\partial x^2} + S_{V_1} \\
&- k^{+}_{V_1,V_1} C^2_{V_1} - C_{V_1} \sum_{j=0}^{y_M-1} \sum_{i=0}^{x_M(j)} k^{+}_{V_1,He_iV_j} C_{He_iV_j} - C_{V_1} \sum_{k=1}^{z_M} k^{+}_{V_1,I_k} C_{I_k} + \sum_{j=2}^{y_M} k^{+}_{V_j,I_{j-1}} C_{V_j} C_{I_{j-1}} \\
&+ 2 \times k^{-PD}_{V_2} C_{V_2} + \sum_{j=3}^{y_M} k^{-PD}_{V_j} C_{V_j} + \sum_{j=1}^{y_M} \sum_{i=1}^{x_M(y)} k^{-PD}_{He_iV_j} C_{He_iV_j} \\
&+ k^{-PD}_{He_1V_1} C_{He_1V_1}
\end{aligned} \tag{2.13}$$

The PDE describing the evolution of the concentration of a self-interstitial atom I_1 is:

$$\begin{aligned}
\frac{\partial C_{I_1}}{\partial t} &= D_{I_1} \frac{\partial^2 C_{I_1}}{\partial x^2} + S_{I_1} \\
&- k^{+}_{I_1,I_1} C^2_{I_1} - C_{I_1} \sum_{j=1}^{y_M} \sum_{i=0}^{x_M(j-1)} k^{+}_{I_1,He_iV_j} C_{He_iV_j} + \sum_{k=2}^{z_M} k^{+}_{V_{k-1},I_k} C_{V_{k-1}} C_{I_k} \\
&+ 2 \times k^{-PD}_{I_2} C_{I_2} + \sum_{k=3}^{z_M} k^{-PD}_{I_k} C_{I_k} \\
&+ \sum_{j=0}^{y_M-1} \sum_{i=1}^{x_M(y)} k^{-TM}_{He_iV_j} C_{He_iV_j}
\end{aligned} \tag{2.14}$$

Now we can proceed to the PDEs describing the evolution of the concentration of pure cluster species (He_x,V_y,I_z).

The PDEs describing the evolution of the concentration of helium clusters He_x are:

$$\begin{aligned}\frac{\partial C_{He_x}}{\partial t} &= D_{He_x}\frac{\partial^2 C_{He_x}}{\partial x^2} \\ &- k^+_{He_x,He_x}C^2_{He_x} - C_{He_x}\sum_{j=0}^{y_M}\sum_{i=0}^{x_M(j)-x} k^+_{He_x,He_iV_j}C_{He_iV_j} \\ &+ \sum_{i=1}^{\lfloor x/2\rfloor} k^+_{He_i,He_{x-i}}C_{He_i}C_{He_{x-i}} + \sum_{j=1}^{y_M} k^+_{He_xV_j,I_j}C_{He_xV_j}C_{I_j} \\ &+ k^{-He}_{He_{x+1}}C_{He_{x+1}} - k^{-He}_{He_x}C_{He_x} \\ &+ k^{-V}_{He_xV_1}C_{He_xV_1} \\ &- k^{-TM}_{He_x}C_{He_x}\end{aligned} \tag{2.15}$$

Note that any mobile helium cluster can react with any other mobile helium cluster to form a larger mobile helium cluster.
The PDEs describing the evolution of the concentration of vacancy clusters V_y are:

$$\begin{aligned}\frac{\partial C_{V_y}}{\partial t} &= D_{V_y}\frac{\partial^2 C_{V_y}}{\partial x^2} + S_{V_y} \\ &- k^+_{V_y,V_y}C^2_{V_y} - C_{V_y}\sum_{j=0}^{y_M-y}\sum_{i=0}^{x_M(j)} k^+_{V_y,He_iV_j}C_{He_iV_j} \\ &+ \sum_{j=1}^{\lfloor y/2\rfloor} k^+_{V_j,V_{y-j}}C_{V_j}C_{V_{y-j}} + \sum_{k=y+1}^{z_M} k^+_{V_k,I_{k-y}}C_{V_k}C_{I_{k-y}} \\ &+ k^{-PD}_{V_{y+1}}C_{V_{y+1}} - k^{-PD}_{V_y}C_{V_y} \\ &+ k^{-He}_{He_1V_y}C_{He_1V_y}\end{aligned} \tag{2.16}$$

The PDEs describing the evolution of the concentration of self-interstitial clusters I_z are:

$$\begin{aligned}\frac{\partial C_{I_z}}{\partial t} &= D_{I_z}\frac{\partial^2 C_{I_z}}{\partial x^2} + S_{I_z} \\ &- k^+_{I_z,I_z}C^2_{I_z} - C_{I_z}\sum_{j=z}^{y_M}\sum_{i=0}^{x_M(j)} k^+_{I_z,He_iV_j}C_{He_iV_j} \\ &+ \sum_{k=1}^{\lfloor z/2\rfloor} k^+_{I_k,I_{z-k}}C_{I_k}C_{I_{z-k}} + \sum_{j=z+1}^{y_M} k^+_{V_{j-z},I_j}C_{V_{j-z}}C_{I_j} \\ &+ k^{-PD}_{I_{z+1}}C_{I_{z+1}} - k^{-PD}_{I_z}C_{I_z} \\ &+ \sum_{j=0}^{y_M-1}\sum_{i=1}^{x_M(j)} k^{-TM}_{He_iV_j}C_{He_iV_j}\end{aligned} \tag{2.17}$$

And finally, the ODEs describing the evolution of the concentration of immobile helium-vacancy clusters $He_xV_y, x \geq 1, y \geq 1$, are:

$$\begin{aligned}
\frac{\partial C_{He_xV_y}}{\partial t} &= -C_{He_xV_y} \sum_{\substack{i=1 \\ i+x \leq x_M(y)}}^{x_M(0)} k^+_{He_i, C_{He_xV_y}} C_{He_i} \\
&- C_{He_xV_y} \sum_{j=1}^{y_M - y} k^+_{V_j, He_xV_y} C_{V_j} \\
&- C_{He_xV_y} \sum_{k=1}^{y} k^+_{I_k, He_xV_y} C_{I_k} \\
&+ \sum_{i=1}^{x_M(0)} k^+_{He_i, He_{x-i}V_y} C_{He_i} C_{He_{x-i}V_y} \\
&+ \sum_{j=1}^{y} k^+_{V_j, He_xV_{y-j}} C_{V_j} C_{He_xV_{y-j}} \\
&+ \sum_{k=1}^{y_M - y} k^+_{I_k, He_xV_{y+k}} C_{I_k} C_{He_xV_{y+k}} \\
&- k^{-He}_{He_xV_y} C_{He_xV_y} + k^{-He}_{He_{x+1}V_y} C_{He_{x+1}V_y} \\
&- k^{-PD}_{He_xV_y} C_{He_xV_y} + k^{-PD}_{He_xV_{y+1}} C_{He_xV_{y+1}} \\
&- k^{-TM}_{He_xV_y} C_{He_xV_y} + k^{-TM}_{He_xV_{y-1}} C_{He_xV_{y-1}}
\end{aligned} \tag{2.18}$$

The chemical network describing the reactions and dissociation events of equations 2.12 to 2.18 seems complicated, but it should be noted that they we have a simple balance of mass: if defects containing vacancies are given a negative weight proportional to the number of vacancies, and species containing self-interstitials are given a positive weight proportional to the number of self-interstitials (which seem logical since vacancies are physically missing tungsten atoms in the lattice, while interstitials are extra tungsten atoms in the lattice), then the chemical network describes mass balance equations. Mass can then only be added to the system by the source term, or removed through diffusion towards the free surfaces. The concept of balance is important as it will allow to efficiently compute the reaction and dissociation term for each species by considering reactions and not individual species (and so not the complex sum terms in equations 2.12 to 2.18), as we will see in chapter 4.

It is clear that the cluster dynamics equations depend only on three types of parameters: the diffusion coefficients D, the binding energies for each possible dissociation event E_b, and the capture radii of each species r. The determination of these parameters is the focus of the next chapter.

Chapter 3

Molecular Dynamics for Parameter Estimation

3.1 Introduction

Molecular Dynamics (MD) simulations are a powerful tool to investigate atomistic effects in materials. In this chapter, we will show how MD simulations can be used to determine the cluster dynamics model parameters identified in chapter 2. We will also compare these results with experimental and density functional theory (DFT) results when available. Finally, we will determine a set of parameters that are used in the cluster dynamics model through the rest of this dissertation. To perform MD simulations, we use the parallel molecular dynamics code LAMMPS (Large-scale Atomic/ Molecular Massively Parallel Simulator) [38] developed by Sandia National Laboratory. LAMMPS is optimized for parallel computers, and uses spatial-decomposition techniques to partition the simulation domain into small 3D sub-domains, one of which is assigned to each processor. The computational efficiency of LAMMPS allows us to perform simulations on a $10 \times 10 \times 10$ nm^3 domain up to hundreds of nanoseconds.

3.2 Background on Molecular Dynamics

MD simulations have atomistic length and timescales which reveal material changes that happen too fast and too small for experimental observations. Not only do they complement experimental observations, the MD studies are also tailored to reveal important events that can then be incorporated in longer time and length scale methods for materials evolution simulations. The concept behind MD is straightforward: MD simulations calculate the trajectory of every individual atom in the simulation box based on Newton's second law of motion. The forces on each particle are only a function of the interatomic potentials. For a system of N particles, the Newton equations to

solve for each particle i are:

$$m_i\vec{a_i} = \sum_{\substack{j=1 \\ j\neq i}}^{N} \vec{F}_{ext} = -\sum_{\substack{j=1 \\ j\neq i}}^{N} \frac{\partial V_i}{\partial r_{ij}} \vec{u}_{ij} \tag{3.1}$$

where $\vec{a_i} = \frac{\partial \vec{v_i}}{\partial t} = \frac{\partial^2 \vec{r_i}}{\partial t^2}$ is the acceleration, $\vec{r_i}$ the position vector, $\vec{v_i}$ the velocity vector, m_i is the mass, V_i is the potential energy with respect to atomic position for atom i, and $\vec{u}_{ij}$ is a unit vector in the direction $i \rightarrow j$. Given an initial configuration of the N-atom system determined by parameters such as boundary conditions, lattice structure, integration method or thermostat, the numerical integration computes the result.

In this research, semi-empirical, interatomic potentials are used to describe body-centered cubic tungsten and its interactions with helium. These potentials are the key input to the molecular dynamics simulations performed using LAMMPS. The tungsten-tungsten interaction was described by the N-body embedded atom model (EAM) potential of Finnis and Sinclair [39] as modified by Ackland and Thetford [40], and which was recently modified by Juslin and Wirth [41] at small interatomic separations for sputtering and cascade simulations using a Ziegler–Biersack–Littmark (ZBL) universal potential [42], which is appropriate at high energy (short interatomic separations). The helium-tungsten pair potential fit by Juslin and Wirth [41] was tailored to the study of small helium-vacancy clusters. The helium-helium interaction is described by the 1968 Beck potential [43] and was modified at small interatomic separations by Morishita and co-workers [44] to connect with the ZBL potential fit at short ranges.

The numerical schemes to solve the resulting set of coupled partial differential equations for molecular dynamics are usually in the family of the Verlet algorithms [45]. The following defines the position within the Verlet algorithm:

$$r(t+\Delta t) = r(t) + v(t)\Delta t + \frac{1}{2}a(t)\Delta t^2 + \frac{1}{3!}r(t)\Delta t^3 + O(\Delta t^4) \tag{3.2}$$

$$r(t-\Delta t) = r(t) - v(t)\Delta t + \frac{1}{2}a(t)\Delta t^2 + \frac{1}{3!}r(t)\Delta t^3 + O(\Delta t^4) \tag{3.3}$$

$$r(t+\Delta t) + r(t-\Delta t) = 2r(t) + a(t)\Delta t^2 + O(\Delta t^4) \tag{3.4}$$

If the velocity at time t is then computed given the position at time $t+\Delta t$ the resulting scheme is the Basic Verlet integration:

$$\left.\begin{aligned} r(t+\Delta t) &= 2r(t) - r(t-\Delta t) + a(t)\Delta t^2 + O(\Delta t^4) \\ v(t) &= \frac{1}{2\Delta t}[r(t+\Delta t) - r(t-\Delta t)] + O(\Delta t^2) \end{aligned}\right\} \quad \text{Basic Verlet Integration} \tag{3.5}$$

The integration most commonly used in MD is actually the Velocity Verlet algorithm in which the velocity and the position are calculated at the same increment of the time variable. This is particularly practical in MD to get the velocity but also the Kinetic Energy at the same time the position is computed. The Velocity Verlet algorithm can be computed in the following way:

1. First, calculate $r(t+\Delta t) = r(t) + v(t)\Delta t + \frac{1}{2}a(t)\Delta t^2$
2. Then derive $a(t+\Delta t)$ from the interaction potentials, $-\sum_{\substack{j=1 \\ j\neq i}}^{N} \frac{\partial V_i}{\partial r_{ij}}\vec{u}_{ij}$, and using $x(t+\Delta t)$
3. Finally, calculate $v(t+\Delta t) = v(t) + \frac{1}{2}(a(t) + a(t+\Delta t))\Delta t$

This family of algorithms has properties that are particularly well adapted to molecular dynamics. Not only is it simple, but like the equations of motion it is time reversible and conserves energy. The velocity, however, has a local error that is only $O(\Delta t^2)$. The usual timestep requirement for applying this numerical integration scheme to solid-state material systems is on the order of 0.1 to 10 femtoseconds. Such MD simulations are therefore appropriate up to times on the order of nanoseconds.

3.3 Diffusion Coefficients

The diffusivity of helium atoms, vacancies and self-interstitial atoms is among the most important parameters in the cluster dynamics equations 2.12 to 2.18, as it determines both the diffusion rates of particles due to a concentration gradient as well as the reaction rates through equation 2.6. In this section, we describe the results of computing the diffusion coefficients of mobile species using molecular dynamics and compare the results to experimental values and available DFT data.

3.3.1 Methodology

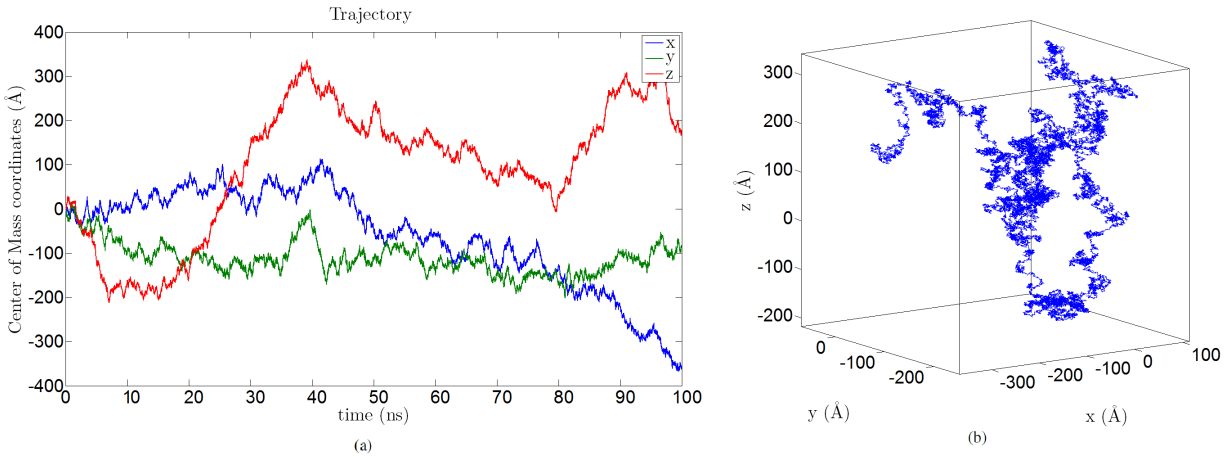


Figure 3.1: (a) Center of mass trajectory of a He_2 cluster at 1000 K, and (b) spatial trajectory of a He_2 cluster at 1000 K.

The motion of a particle in a medium (such as helium atoms, vacancies or self-interstitials in tungsten) follows the characteristics of Brownian motion. Figure 3.1 shows the center of mass trajectory of a di-helium cluster at a temperature of 1000 Kelvin over a time interval of 100 nanoseconds. We can see the Brownian nature of this 3-dimensional trajectory, with random jumps from an interstitial position to another. Such a trajectory can be described by a Langevin equation, which is simply Newton's equation of motion including linear friction and a random force representing the thermal fluctuation of the particle [46]:

$$m\frac{d^2\vec{r}}{dt^2} = -\gamma\frac{d\vec{r}}{dt} + \sigma\xi(t) \tag{3.6}$$

where m is the mass of the diffusing species, γ is a friction coefficient, and $\xi(t)$ is a stochastic variable such that $\langle\xi(t)\rangle = 0$ and $\langle\xi(t_1)\xi(t_2)\rangle = \delta(t_2 - t_1)$. Using the classical equi-partition principle $\frac{1}{2}m\langle v^2(t)\rangle = \frac{3}{2}k_bT$, we obtain an equation for the center of mass mean squared displacement (MSD) of the species [47, 48]:

$$\langle R^2(t)\rangle = \frac{6mk_bT}{\gamma^2}\left(\frac{\gamma t}{m} - \left(1 - e^{-\frac{\gamma t}{m}}\right)\right) \tag{3.7}$$

This equation defines two distinct regimes: for small times ($t \ll \frac{m}{\gamma}$), $\langle R^2(t)\rangle \propto t^2$, that is the mean squared displacement grows quadratically with time. This is the ballistic regime observed at short time scales [49]. For large time scales ($t \gg \frac{m}{\gamma}$, or taking the limit as $t \to \infty$), the mean squared displacement grows linearly with time. This long time behavior is the Einstein equation [50] which relates the diffusion coefficient of a diffusing species in a medium and its mean squared displacement:

$$\lim_{t\to\infty} = \frac{\langle R^2(t)\rangle}{6t} = \frac{k_bT}{\gamma} \equiv D \tag{3.8}$$

By measuring the center of mass trajectory of the diffusing species using molecular dynamics simulations, we can therefore compute the diffusion coefficient of that species in tungsten. Equation 3.7 gives us a practical way of determining the amount of time needed for each simulation to be in the linear regime. We need

$$t \gg \tau_{min} = \frac{m}{\gamma} = \frac{mD}{k_bT} \tag{3.9}$$

Once we determine the simulation time needed to observe each species in the linear regime, and thus be able to determine D from equation 3.8, we are able to perform molecular dynamics simulations at several different temperatures for each species to determine the diffusion coefficient in each case. The temperature dependence of the diffusion coefficient $D(T)$ is usually expressed by an Arrhenius expression:

$$D(T) = D_0e^{-\frac{E_m}{k_bT}} \tag{3.10}$$

where D_0 and E_m are the pre-exponential factor and the migration energy, respectively. We will therefore report results in term of these quantities for each mobile species. However, non-Arrhenius behavior of diffusing species can be observed, especially in the case of self-interstitial atoms [47],

and we shall make note of this when it is observed.
A practical matter arises in these simulations, since we have not performed multiple independent simulations for each freely diffusing species, but rather performed a single, long simulation (t $\geq$ 100 ns). Since true Brownian motion is supposed to be independent from the previous path (e.g. without correlation or memory of previous atomic jumps), we split the trajectory into many independent sub-trajectories, such that each sub-trajectory satisfies the time requirement of equation 3.9. Each sub-trajectory can then be seen as an independent trajectory for a diffusing species. We can compute one mean squared displacement (MSD) curve for each independent particle as a time-averaged curve: for a given time t, $MSD_{time}(t)$ is the square displacement averaged over all time intervals $[t_1, t_2]$ such that $t_2 - t_1 = t$. Figure 3.2 shows an example of such $MSD_{time}(t)$ curves for a di-helium cluster freely diffusing at 300 Kelvin. The MD simulation length was 100 nanoseconds, and the center of mass trajectory of the di-helium species was split into ten independent sub-trajectories. The ensemble average mean squared displacement (MSD) curve is then

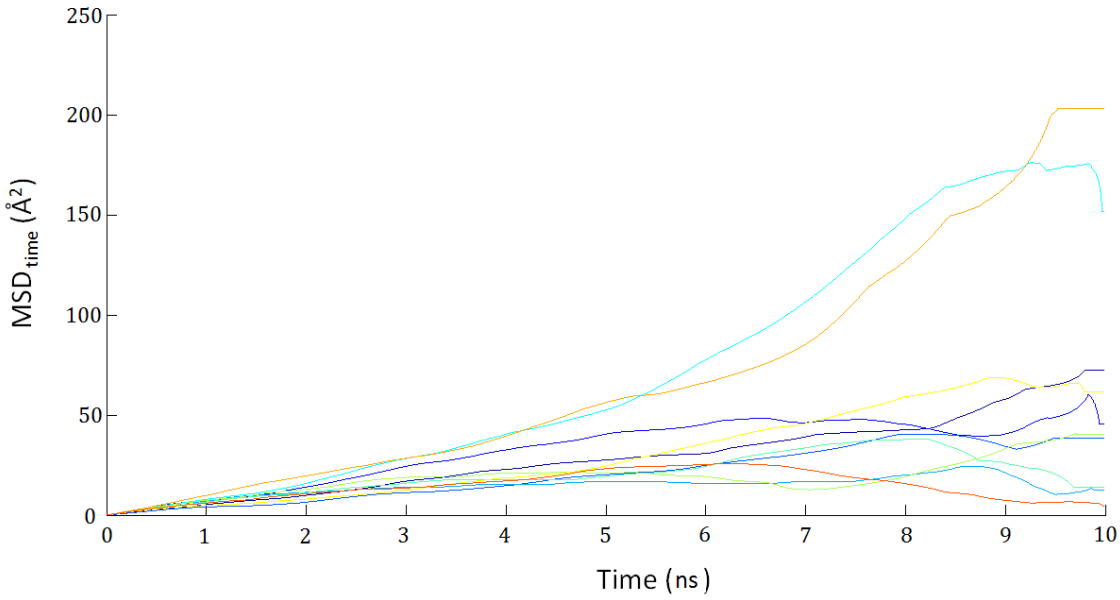


Figure 3.2: MSD_{time} curves for a He_2 cluster diffusing at 300 K. The 100 nanosecond trajectory was split into 10 sub-trajectories of 10 nanoseconds each (The graphs are plotted using the MSDanalyzer MATLAB package [10]).

the average of the $MSD_{time}(t)$ over all independent sub-trajectories. Figure 3.3 shows the MSD curve derived from the previous example, along with the 95 $\%$ confidence interval. The number of sub-trajectories needed for reaching accurate predictions is difficult to calculate $a\ priori$, but we can $a\ posteriori$ observe if the MSD curve converged and thus be confident in the results. For a given MD simulation, there is a trade-off between the number of independent sub-trajectories and

the duration of each sub-trajectory: A high number of sub-trajectories provides the advantage of good statistical average, but shortens the duration of each sub-trajectory, at the risk of sampling particles in the ballistic regime and therefore obtaining an incorrect assessment of the diffusion coefficient. As the number of sub-trajectories decreases, the length of each sub-trajectory increases and therefore the particles are more likely to be sampled in the linear regime that enables the correct diffusion coefficient to be calculated, although at the risk of having poor statistics for the ensemble average. Figure 3.4 shows an example of such a trade-off. Notice that for large numbers of independent sub-trajectories, the value of the diffusion coefficient converges since equation 3.9 is still satisfied ($\tau_{min} \sim 10^{-17}$ seconds in this case). One way to increase both the number of sub-trajectories and their duration is simply to increase the time of the MD simulation. In this work, the MD simulations have a duration of several hundred nanoseconds, which is sufficient to obtain good statistics for most species across a large range of temperatures. All MD simulations used to determine the diffusion coefficients have periodic boundary conditions so that the species can freely diffuse without artificial boundaries which would give an oncorrect value of the diffusion coefficient.

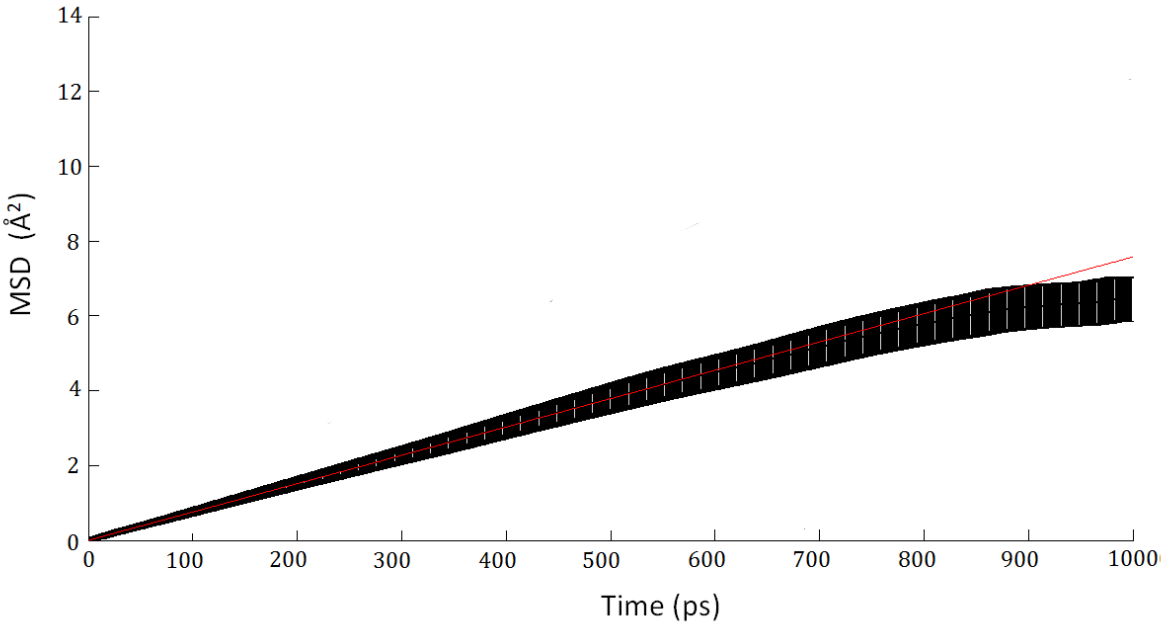


Figure 3.3: MSD curve for a He_2 cluster diffusing at 300 K. The MD simulation duration is 100 nanoseconds and the number of sub-trajectories was 100, each lasting one nanosecond. The black area indicates the 95 $\%$ confidence interval, and the red curve is the linear regression giving the value of the diffusion coefficient.

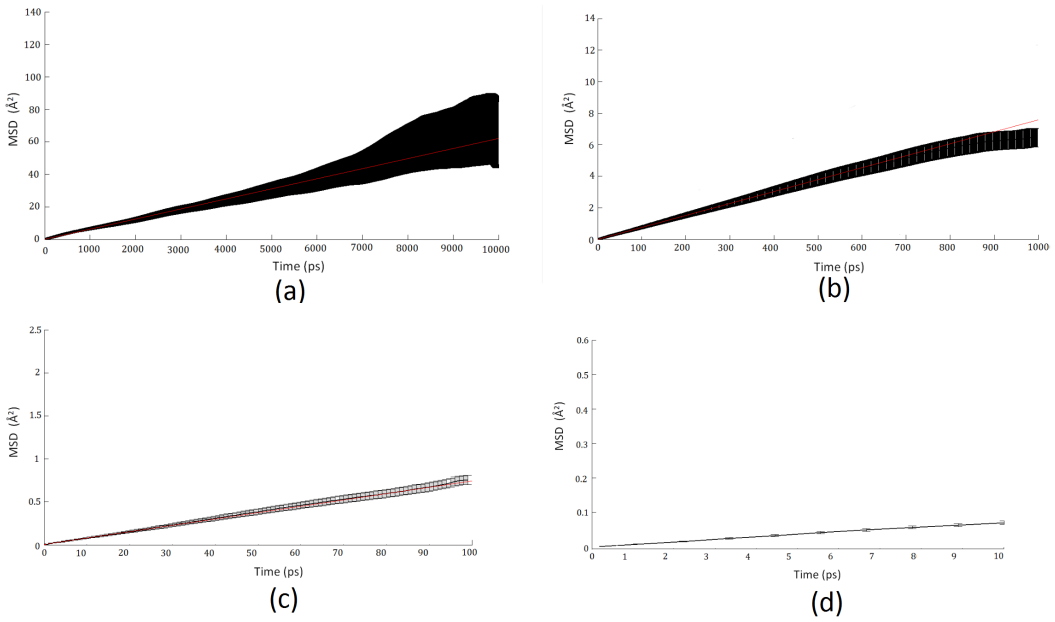


Figure 3.4: MSD curves for a He_2 cluster diffusing at 300 K for different numbers of sub-trajectories. Equation 3.9 gives $\tau_{min} = 4 \times 10^{-6}$ ns. (a) 10 sub-trajectories of 10 ns each. $D = 1.05 \times 10^{-11}$ m^{2}s^{-1}. (b) 100 sub-trajectories of 1 ns each. $D = 1.25 \times 10^{-11}$ m^{2}s^{-1}. (c) 1000 sub-trajectories of 0.1 ns each. $D = 1.24 \times 10^{-11}$ m^{2}s^{-1}. (d) 10000 sub-trajectories of 0.01 ns each. $D = 1.24 \times 10^{-11}$ m^{2}s^{-1}.

3.3.2 Helium results

As mentioned in chapter 2, helium atoms tend to aggregate in tungsten to form small clusters of helium atoms, denoted by He_x, where x defines the number of helium atoms. During MD time scales, these clusters are mobile up to about $x = 6$. The diffusion coefficient at the lowest temperature of 300 Kelvin is $D \sim 10^{-12}$ m^{2}s^{-1} and equation 3.9 gives $\tau_{min} \sim 10^{-17}$ seconds, while at the highest temperature of 2000 Kelvin $D \sim 10^{-8}$ m^{2}s^{-1} and equation 3.9 gives $\tau_{min} \sim 10^{-15}$ seconds. Therefore, even relatively short MD simulations are sufficient to reach the linear regime, and long MD simulations ($\sim$ 100 ns) allows us to obtain a very good statistical confidence (with small 95 $\%$ confidence intervals) on the values of the diffusion coefficients. Figure 3.5 shows the Arrhenius behavior for interstitial helium and small helium clusters containing up to 5 helium atoms ($He_1 - He_5$). As expected, the diffusion coefficient is temperature dependent and follows an Arrhenius law in a large range of temperatures. For large temperatures (T $>$ 1000 K), we see an inflexion in the slope of $\ln(D)$ vs $1/T$: This indicates a possible transition from the low temperature path used to jump from one position to another to a new path accessible at high temperatures. Nevertheless, the inflexion is quite small and we choose to describe the temperature dependence of the diffusion coefficient by a single fit (Activation energy and diffusion pre-factor) over the temperature range simulated from 300 to 2000 Kelvin. Table 3.1 summarizes the results for the mobile

helium clusters.

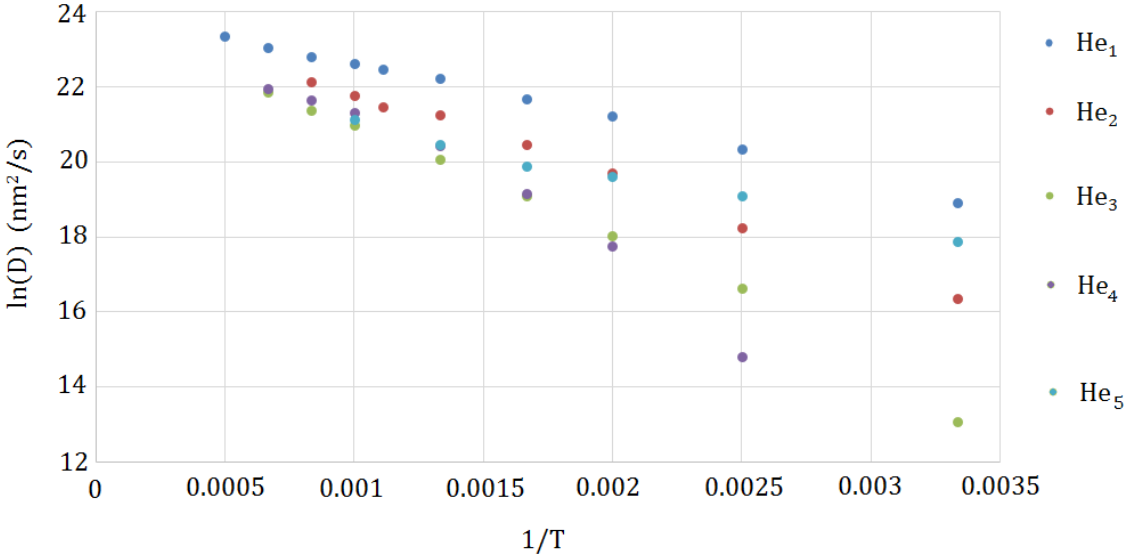


Figure 3.5: Diffusion coefficient versus inverse temperature for helium interstitials and several helium clusters.

Table 3.1: Activation energy and diffusion pre-factor for small helium interstitial clusters.

Number of helium atoms in cluster	1	2	3	4	5	6	≥ 7
E_m (eV)	0.13	0.2	0.25	0.2	0.12	0.3	\
D_0 ($\times 10^{-8}$ m^{2}s^{-1})	2.95	3.24	2.26	1.68	0.520	0.120	0

One practical difficulty in measuring the diffusion coefficients of clusters of atoms is that as mentioned in chapter 2, these clusters can dissociate or undergo trap mutation events. Since we explicitly model the occurence of these events in the cluster dynamics equations, we should be careful to exclude simulations where these events take place, since such processes would give a meaningless diffusion coefficient. Unfortunately, these events become more frequent with increasing temperatures, which prevents us from determining the diffusion coefficients of larger helium clusters at high temperatures with MD simulations. Nonetheless, we can determine the Arrhenius parameters at low temperatures and use these parameters to extrapolate to higher temperatures. It is interesting to note that this issue is not critical: if a species dissociates at a given temperature within the short MD timescales (making the MD simulation useless to determine the diffusion coefficient), this effect will be captured in a low binding energy for these dissociation events, meaning that the species will not exist in meaningful concentrations at the given temperature, as

it immediately dissociates. Fortunately this means that the diffusion coefficient for this cluster at this temperature does not influence the description of the physical system.

3.3.3 Self-Interstitial results

The case of self-interstitial atoms (SIA) and atom clusters is more difficult for several reasons. SIA clusters are mobile in tungsten up to very large sizes, forming interstitial loops. However in this work, there is no direct production of SIA and SIA clusters through irradiation, as the incident helium ion energy is too low. Interstitials can be produced by trap mutation events, but generally at a rate too low for clustering to occur and significant concentrations of SIA clusters to build-up since they should be able to quickly diffuse to the free surface. We do not consider a discrete dislocation loop punching mechanism, by which large, nanometer-sized gas bubbles can eject SIA clusters (as opposed to single SIA in a trap mutation event) which might produce larger concentrations of SIA clusters due to their lower mobility. Therefore in this work, we will only consider single SIA and small SIAs clusters, denoted by I_y where $y \leq 3$, where y defines the number of self-interstitial atoms.

Moreover, at low temperatures and in the MD time scales, SIA and SIA clusters diffuse only in one dimension, while equation 2.6, which gives an expression for the reaction rate constant, assumes the reactants are diffusing in 3 dimensions. Figure 3.6 shows an example of the trajectory for a single SIA at temperatures from 300 to 1000 Kelvin. With increasing temperature, the rotation of the SIA becomes so frequent that the migration of a single SIA can be considered three dimensional. Even at 300 Kelvin, SIA are expected to rotate at a rate of 1.35×10^6 per second [51], which explains why we do not observe SIA rotations at this temperature on the MD time scale but indicates that we can consider the motion to be 3-dimensional over longer diffusional times, such as those modeled at the continuum level by cluster dynamics.

Another issue is the very high mobility of SIA and SIA clusters: typical values for the diffusion coefficient of SIA clusters are on the order of $D \sim 10^{-7}$ m^{2}s^{-1} and equation 3.9 gives $\tau_{min} \sim 10^{-11}$ seconds. Therefore, we need relatively long sub-trajectories in order to measure the MSD in the linear regime. For a given MD simulation time, this means we sample less sub-trajectories in total and therefore the statistical variance is higher. To overcome this difficulty, we have performed several MD simulations of 100 ns at each temperature for I_1 to I_3.

It is also important to note that SIA and SIA clusters are a mathematical construct to describe a defect in the crystalline lattice. Thus, SIA diffusion does not represent physical atoms that are moving as in the case of helium, since a SIA "moves" by taking the lattice position of an existing tungsten atom which becomes the SIA itself. While the defect diffusion is strongly correlated to atomic motion, the diffusion coefficients of defects are different than self-atom diffusion. The activation energy for these events is very low in the temperature range of interest, and the picture of an atom jumping from an equilibrium position to another in a series of infrequent hops is no longer correct. Therefore, we observe a deviation of the Arrhenius behavior for SIA and SIA clusters, as predicted in reference [47].

Figure 3.7 shows the results for interstitial clusters, with the expected deviation from an ideal Arrhenius law, and table 3.2 summarizes the fitting results in term of the Arrhenius parameters.

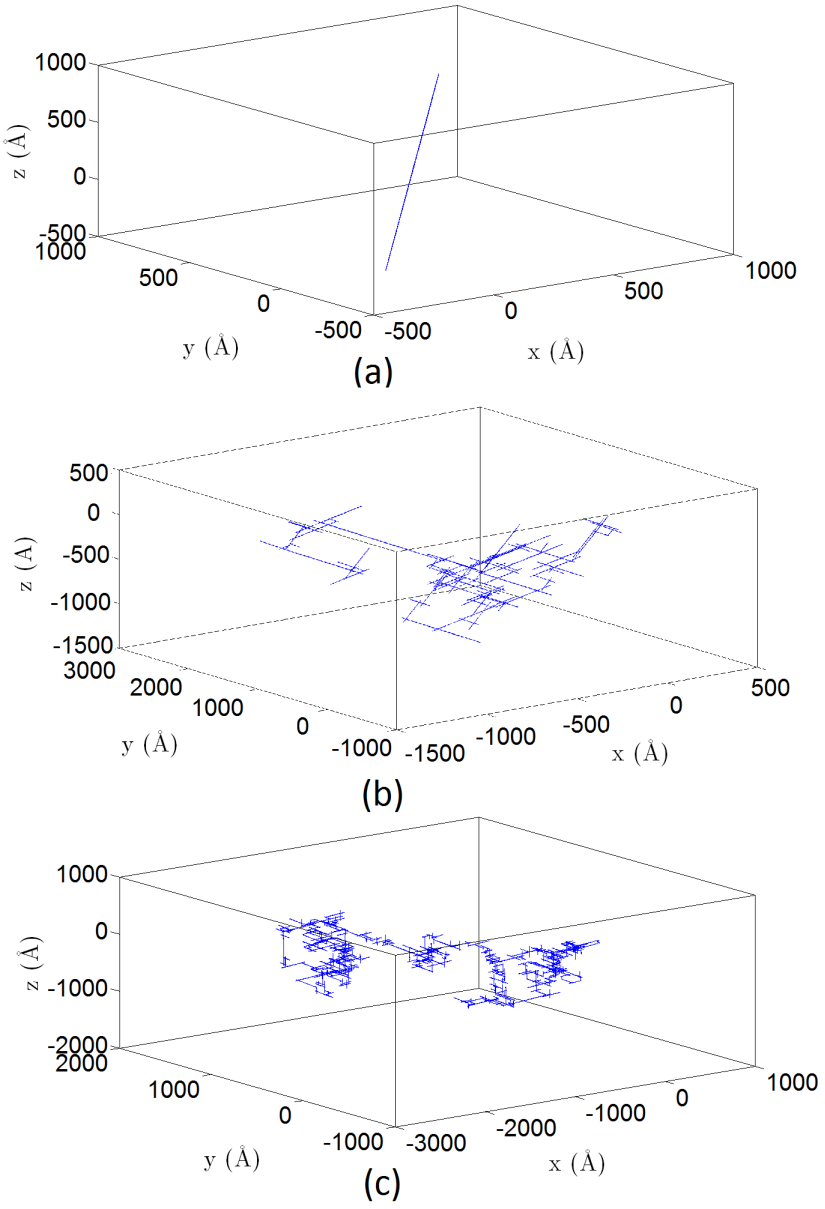


Figure 3.6: Trajectory of a single self-interstitial for a 100 ns simulation at various temperatures. (a) 300 Kelvin, (b) 750 Kelvin, and (c) 1000 Kelvin.

3.3.4 Vacancy results

The mobility of vacancy and vacancy clusters is easier to determine than the mobility of SIAs and SIA clusters. Single vacancies diffuse 3-dimensionally as shown in figure 3.8. The resulting diffusivity follows an Arrhenius law with a high migration energy: no jump is observed below 1000 Kelvin during MD time scales. We can however extrapolate the diffusion coefficient to lower

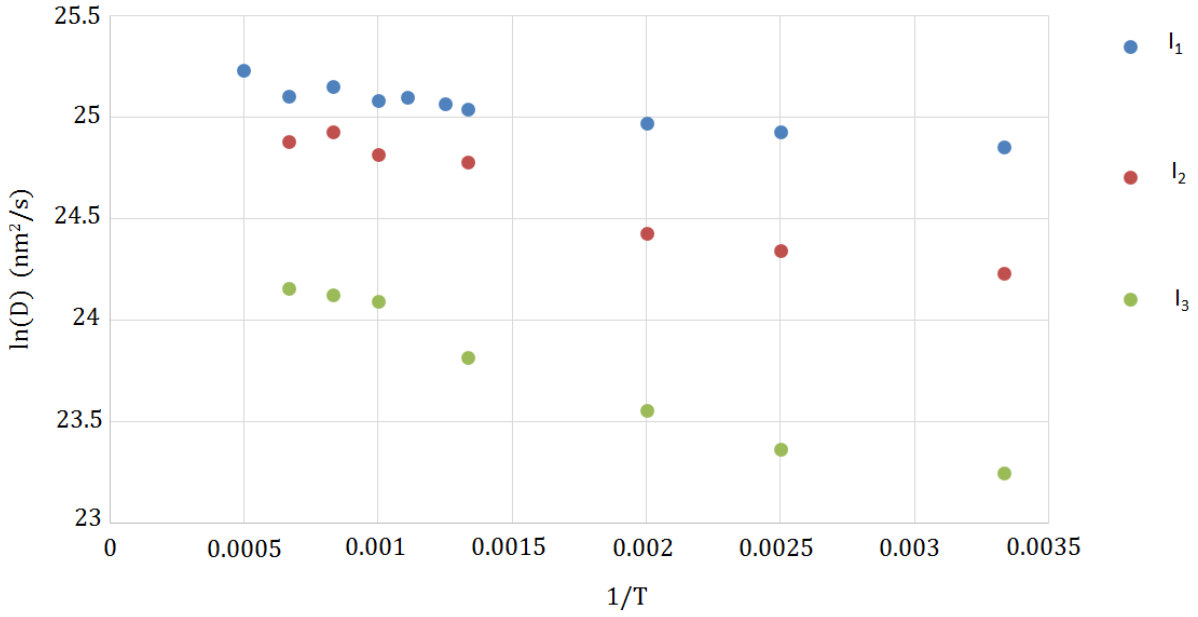


Figure 3.7: Diffusion coefficient versus temperature for SIA clusters.

Table 3.2: Activation energy and diffusion pre-factor for SIA clusters.

Number of interstitials in cluster	1	2	3
E_m (eV)	0.009	0.024	0.033
D_0 ($\times 10^{-8}$ m^{2}s^{-1})	8.77	7.97	3.92

temperatures using the Arrhenius relation obtained at higher temperature. Figure 3.9 shows MD simulation results of the MD simulations for the vacancy diffusivity at several temperatures, and table 3.3 summarizes the results. DFT results indicate that di-vacancies have a negative binding

Table 3.3: Activation energy and diffusion pre-factor for a single vacancy and vacancy clusters.

Number of vacancies in cluster	1	≥ 2
E_m (eV)	1.29	\
D_0 ($\times 10^{-8}$ m^{2}s^{-1})	177	0

energy [24], while MD simulations indicate a very low positive binding energy. Thus, we consider that di-vacancies are not stable and spontaneously dissociate into two single vacancies. Larger vacancy clusters are essentially immobile during MD time scales and their diffusivity is negligible.

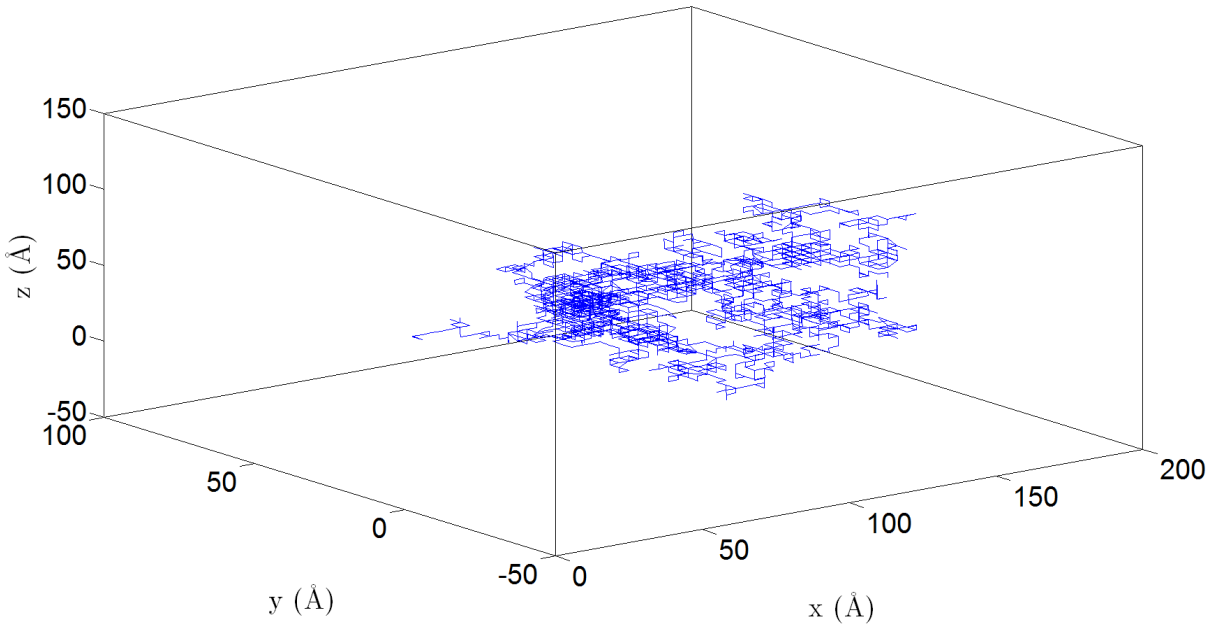


Figure 3.8: Trajectory of a single vacancy at 1900 Kelvin.

3.3.5 Comparison with experimental values

A large database of experimental work exists for migration values of defects in tungsten. However, only values for single defects (single helium, single vacancy or single SIA) are found as it is difficult to isolate a specific clusters of defects in any experiment. This also implies that these experimental values might reflect an average of the diffusivity of clusters of defects since it is not possible to prevent single species from reacting with each other. Therefore, we observe in general higher values than what is predicted by DFT data or MD simulations. Table 3.4 shows a comparison between our MD results and experimental results. It also includes other simulation results. As expected, our results differ from the experimental results but agree quite well with other simulation results.

3.4 Binding Energies

Now that the diffusion coefficients of the mobile species have been determined, we need the binding energies of cluster species relative to the dissociation and trap mutation events in order to compute the dissociation rate constants given by equation 2.8. These binding energies can be defined in relation to the formation energies of each species. Given the dissociation reaction $AB \rightarrow A + B$, the corresponding binding energy $E_{AB \rightarrow A+B}$ is defined as:

$$E_{AB \rightarrow A+B} = E_f(A) + E_f(B) - E_f(AB) \tag{3.11}$$

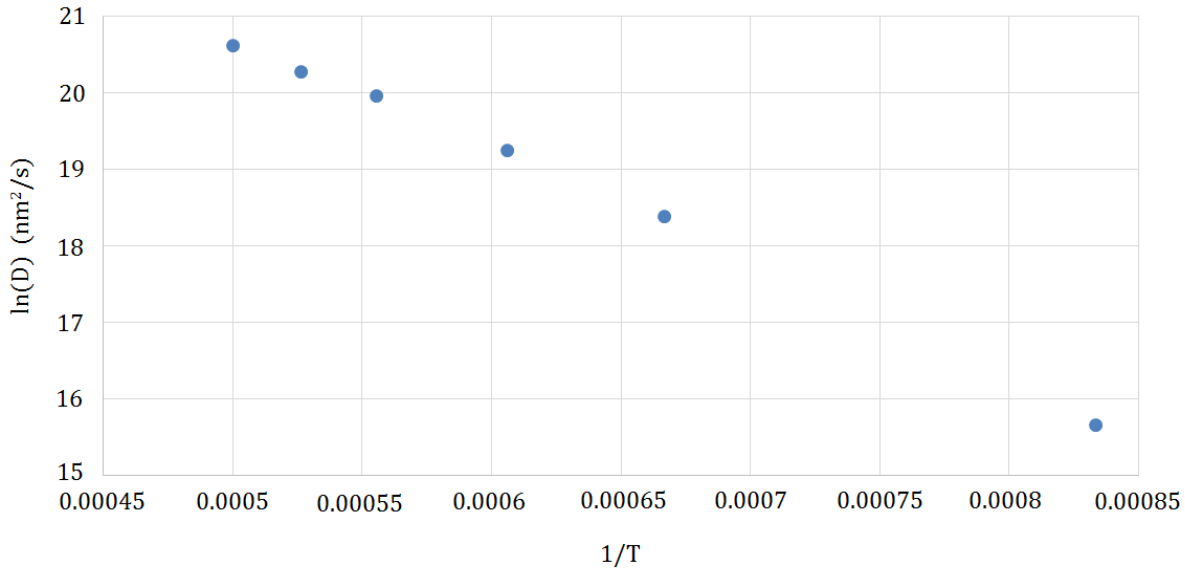


Figure 3.9: Diffusion coefficient versus inverse temperature for a single vacancy.

Table 3.4: Comparison of migration energies between simulation results in this work, experimental results and other simulation results.

Defect	This work	Experimental	Other simulation results
He_1	$E_m = 0.13$ eV	0.24 eV $< E_m <$ 0.32 eV [52, 53]	$E_m = 0.06$ eV [11]
I_1	$E_m = 0.009$ eV	0 eV $< E_m <$ 0.08 eV [52, 54, 55]	$E_m = 0.013$ eV [51]
V_1	$E_m = 1.29$ eV	1.5 eV $< E_m <$ 2.02 eV [56, 57, 58]	1.44 eV $< E_m <$ 2.34 eV [60, 61]

where $E_f(i)$ is the formation energy of the species i. The formation energy represents the potential energy required to create the defect in an otherwise perfect material. Therefore, the problem of computing the binding energies for each possible dissociation and trap mutation event is reduced to computing the formation energy for every species.

The formation energy of a species can be computed using either DFT or MD simulations at 0 Kelvin (also called Molecular Statics). In both cases, the computational method is similar: First, a simulation of N tungsten atoms is performed at 0 K to calculate the total potential energy after minimization E_{pure}. Second, a defect species, such as a helium-vacancy cluster He_xV_y is inserted in the box. The total potential energy after minimization is E_{defect}. The formation energy can then

be expressed by

$$E_f = E_{defect} - \frac{N-y}{N} E_{pure} - xE_{coh}^{He} \tag{3.12}$$

where $E_{coh}^{He} = -0.0054$ eV is the cohesive energy of solid helium at 0 K.
Binding energies can be determined from several sources: experiments, theoretical computations, DFT simulations or MD simulations. Experimental and theoretical values are available for only a very small set of reactions and these values are listed in table 3.5. DFT calculations by Becquart et al. [11] expand this set, as shown in figure 3.10. MD simulations can be performed to determine the formation energies for larger clusters, as has been done by Juslin [12], and we can compute the binding energies using equation 3.11.
DFT simulations are more computationally expensive than MD simulations, and are therefore limited to relatively small He_xV_y clusters ($x, y \leq 20$), but are considered more accurate. Therefore, we will select the set of binding energies for the rest of this work in the following way: The precise binding energies determined experimentally by Kornelsen [14] are used for very small He_xV_y species ($x \leq 5, y \leq 2$). For larger He_xV_y clusters and I_z clusters, DFT data computed by Becquart et al. [11] is used. From these available binding energies we can determine the formation energies using equation 3.11 and compute the binding energies for trap mutation events as well. Finally, for larger He_xV_y clusters ($x \geq 20, y \geq 10$), we determine the binding energies from the formation energies computed using MD simulations by Niklas Juslin [12]. Figure 3.11 shows the resulting binding energies for middle size helium-vacancy clusters. MD simulations have been performed for a very large range of helium-vacancy clusters, up to $He_{400}V_{100}$. Binding energies for larger clusters can be extrapolated, or we can use a different approach by measuring average quantities for very large clusters, as discussed in chapter 6. This provides a set of binding energies determined each by a as accurate a method as possible. Note that regardless of the method used, even for small He_xV_y species, each method (experimental, DFT and MD) is in good agreement with a relatively narrow range of binding energies for each species.

It is also important to note that there exists a discrepancy between the predicted rates of trap mutation events calculated from molecular statics binding energy data and the rates observed in molecular dynamics simulations: we observe trap mutation event at significant rates in molecular dynamics for clusters smaller than the number of helium which should trigger a trap mutation event based on cluster dynamics theory using molecular statics data. As an example, we observe several trap mutation events of a He_6 clusters at 500 Kelvin during a several nanosecond long molecular dynamics simulations, while the binding energy for these trap mutation as calculated from molecular statics is 1.18 eV which gives a half life time $t_{1/2} \sim 1$ second. However MD observations show that all species will have trap mutated in only a few hundred nanoseconds. We thus suspect that trap mutation occurs at a higher rate than what is predicted by cluster dynamics theory. This discrepancy is still being investigated and likely indicates the occurence of many transient events that are highly correlated, however, in this work, we have used the theoretical expression for the rate of trap mutation. Indeed, the discrepancy only represents a small shift in the trap mutation occurence for a helium-vacancy cluster; for example, the observed high trap

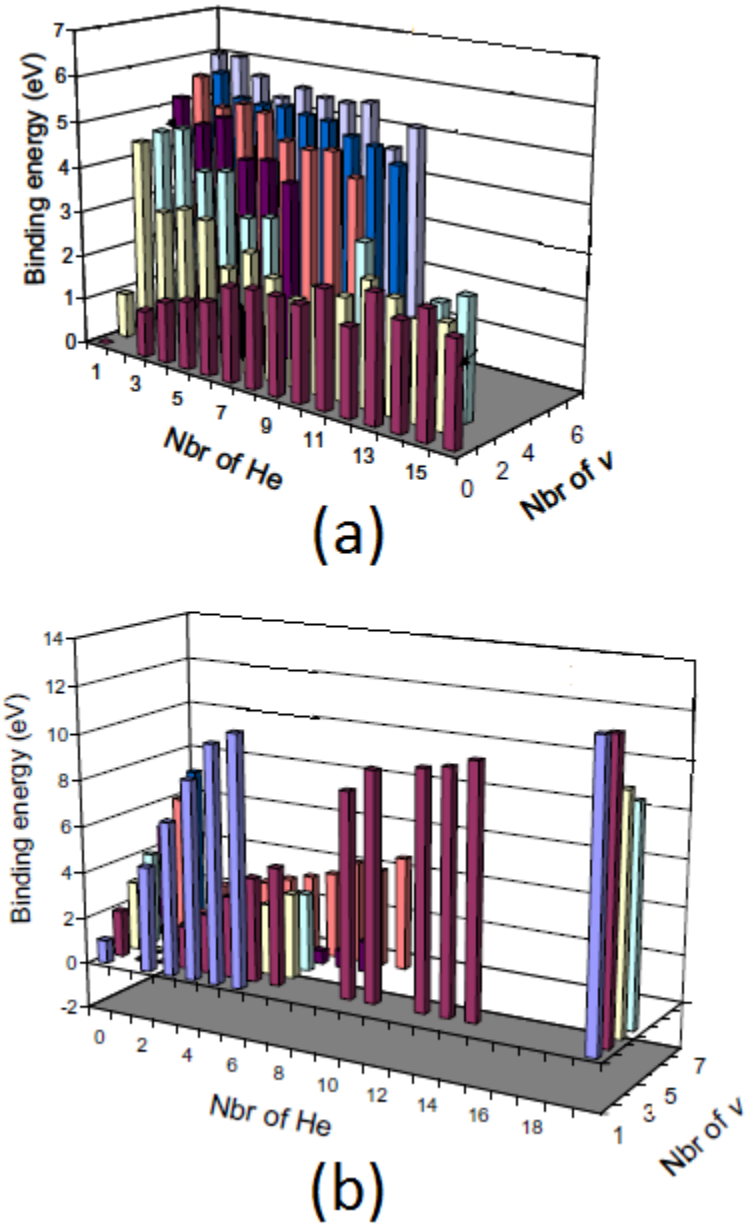


Figure 3.10: Binding Energies for He_xV_y species from DFT simulations by Becquart et al. [11]. (a) Binding Energies for the reaction $He_xV_y \rightarrow He_{x-1}V_y + He$. (b) Binding Energies for the reaction $He_xV_y \rightarrow He_xV_{y-1} + V$.

Table 3.5: Summary of dissociation events for small He_xV_y clusters, and associate binding energies, as obtained from analysis of experimental THDS measurements [14] or theoretical modes [17, 18] .

Reaction	Description	Experimental analysis of Kornelsen [14] (Desorption peak and binding energy)	Theoretical analysis of Wilson [18]	Theoretical analysis of Casper
1	$He_4V \rightarrow He + He_3V$	T = 950 K, E_b = 2.41 eV	E_b = 2.50 eV	E_b = 2.65 eV
2	$He_3V \rightarrow He + He_2V$	T = 1120 K, E_b = 2.88 eV	E_b = 2.52 eV	E_b = 2.73 eV
3	$He_2V \rightarrow He + HeV$	T = 1220 K, E_b = 3.11 eV	E_b = 2.89 eV	E_b = 3.14 eV
4	$HeV \rightarrow He + V$	T = 1560 K, E_b = 4.05 eV	E_b = 4.39 eV	E_b = 4.78 eV
5	$HeKrV_2 \rightarrow He + KrV_2$	T = 1480 K, E_b = 3.84 eV	E_b = 4.40 eV	
6	$He_2V_2 \rightarrow He + HeV_2$		E_b = 4.42 eV	E_b = 4.98 eV
7	$HeV_2 \rightarrow HeV + V$	T $<$ 1560 K, $E_b <$ 4.05 eV		E_b = 0.27 eV

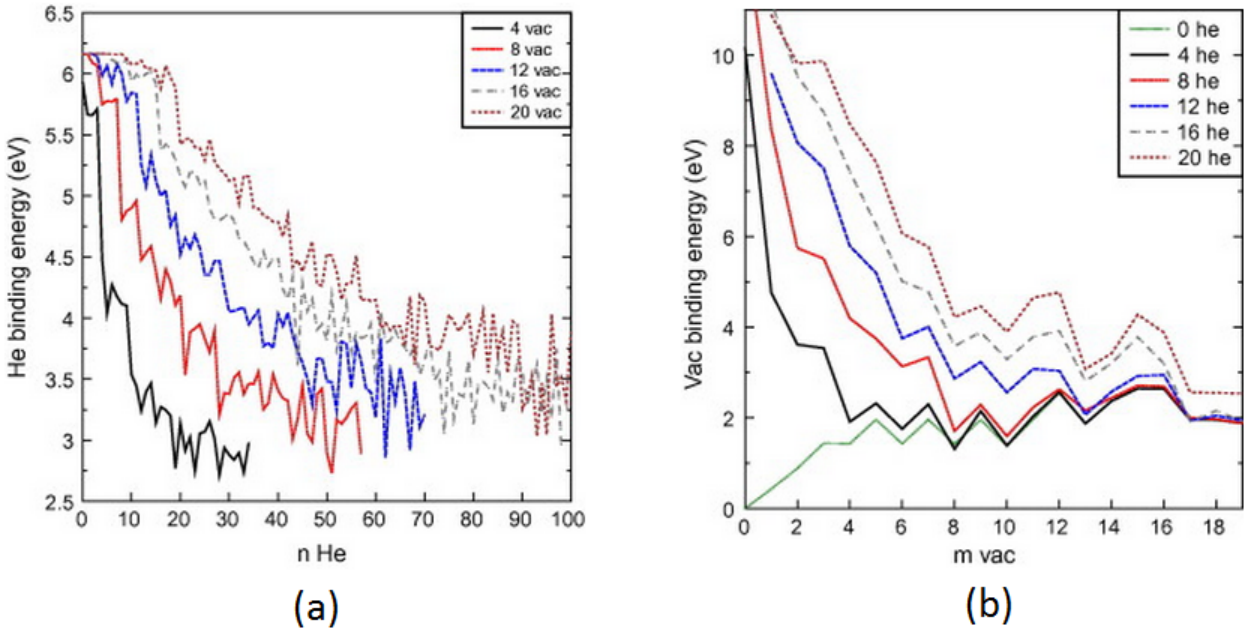


Figure 3.11: Binding Energies for He_xV_y species obtained from MD simulations by Juslin et al. [12]. (a) helium binding energy and (b) vacancy binding energy.

mutation rate in molecular dynamics simulations for He_6 clusters is similar to the rate calculated from the cluster dynamics trap mutation rate constant for He_9 clusters.

3.5 Capture radii

The definition of the reaction constant $k^+_{A,B} = 4\pi(r_A + r_B)(D_A + D_B)$ for reacting species A and B implies that these two species react when the separation distance between them becomes smaller than the sum of their individual capture radii r_A and r_B. The capture radius of a defect represents the distance from the defect inside which the lattice experiences a significant strain field. This modification of the strain field should be sufficient enough that any species which comes closer than this distance becomes trapped leading to a spontaneous reaction. This is known as diffusion limited kinetic theory [36] and is an important assumption within the current modeling approach.
To compute these capture radii, we follow the approach described in References [63] and [11]; namely that the capture radius is computed approximately as the radius of the volume of a sphere containing the species and the surrounding volume affected by the modification of the strain field. Denoting the lattice parameter a_0, we can define the capture radius of a single vacancy $r_{V_1} = \frac{\sqrt{3}}{4}a_0$ which is half the distance of the vacancy to the nearest neighbor, and arbitrarily define the capture radius of a single helium $r_{He_1} = 0.3$ nm which is approximately 95% of the tungsten lattice parameter. The capture radius for vacancy clusters and mixed helium-vacancy clusters containing y vacancies is calculated from:

$$r_{He_xV_y} = r_{He_0V_1} + \left(\frac{3}{4\pi}\frac{a_0^3}{2}y\right)^{1/3} - \left(\frac{3}{4\pi}\frac{a_0^3}{2}\right)^{1/3} \tag{3.13}$$

independent of the number of helium in the cluster. This assumes the shape of the helium-vacancy cluster is a sphere determined by the number of vacancies in the cluster.
For pure helium clusters, the capture radius is calculated as:

$$r_{He_x} = r_{He_1} + \left(\frac{3}{4\pi}\frac{a_0^3}{10}x\right)^{1/3} - \left(\frac{3}{4\pi}\frac{a_0^3}{10}\right)^{1/3} \tag{3.14}$$

which assumes that pure helium clusters grow as non-spherical platelets.
For interstitial clusters containing z interstitials, we use an approximation formula similar to that of vacancy clusters, modified by a bias factor of 1.15 to reflect the fact that interstitial clusters have a larger surrounding strain field:

$$r_{I_z} = 1.15 \times r_{He_0V_1} + \left(\frac{3}{4\pi}\frac{a_0^3}{2}z\right)^{1/3} - \left(\frac{3}{4\pi}\frac{a_0^3}{2}\right)^{1/3} \tag{3.15}$$

Note that this also assumes a spherical shape for SIA clusters as mentioned before. This is a weaker approximation as SIA clusters form non-spherical dislocation loops, however, since the concentration of large SIA clusters is negligible as discussed previously, this assumption does not influence the results of the model.

Chapter 4

Cluster Dynamics Solver

4.1 Introduction

Under fusion relevant irradiation conditions, it is common to have gas bubbles with hundreds of helium atoms filling a void consisting of hundreds of vacancies. Hence, the number N of species to model can quickly become very large ($N > 10,000$). Therefore, solving the resulting system of reaction-diffusion equations specified by equations (2.12)-(2.18) is a computational challenge. This chapter further describes the cluster dynamics equations and presents an algorithm to efficiently solve them.

4.2 Numerical Analysis

4.2.1 System of Equations

The reaction-diffusion system of Partial Differential Equations (PDE) describing the evolution of the system can be written as

$$\begin{cases} \frac{\partial C_i(x,t)}{\partial t} = D_i(t)\frac{\partial^2 C_i(x,t)}{\partial x^2} + Q_i(C_1(x,t), ..., C_N(x,t)) \\ \text{for } (x,t) \in [0,L] \times \mathbb{R}^+, \quad \forall i = 1...N \end{cases} \tag{4.1}$$

with boundary conditions

$$\begin{aligned} C_i(x=0,t) = C_i(x=L,t) = 0, \quad \text{for } t \in \mathbb{R}^+, \quad \forall i = 1...N \\ C_i(x,t=0) = C_i^{(0)}(x), \quad \text{for } x \in [0,L], \quad \forall i = 1...N \end{aligned} \tag{4.2}$$

This reaction-diffusion system of equations represents a slab of thickness L in which the species are able to diffuse due a gradient of concentrations and react with each other. The initial concentration of species is given either by physical considerations (equilibrium concentration of vacancies and interstitials, experimental observations) or by the results of other simulation codes (e.g. SRIM [9]).

We can rewrite this system in vector form as

$$\frac{\partial \mathbf{C}(x,t)}{\partial t} = \mathbf{D}(t)\frac{\partial^2 \mathbf{C}(x,t)}{\partial x^2} + \mathbf{Q}(\mathbf{C}(x,t)) \tag{4.3}$$

where

- $\mathbf{C}(x,t) = (C_1(x,t), \dots, C_N(x,t))^T$ is the solution vector containing the concentrations of all the chemical species as a function of their position and time.
- $\mathbf{D}$ is the diagonal matrix of diffusion coefficients. Let n be the number of mobile species ($n << N$ since only a few species are mobile), and we can assume without loss of generality for now to order the species by their mobility:

$$\mathbf{D} = \overbrace{\left(\begin{array}{ccc|c} \overbrace{D_1 & 0 & 0}^{n} & \\ 0 & \ddots & 0 & \mathbf{0} \\ 0 & 0 & D_n & \\ \hline & \mathbf{0} & & \mathbf{0} \end{array}\right)}^{N}$$

- $\mathbf{Q}(\mathbf{C}(x,t)) = (Q_1(\mathbf{C}(x,t)), \dots, Q_N(\mathbf{C}(x,t)))^T$ is the source term vector which includes production, reaction and dissociation terms. The source term is local: $Q_1, ..., Q_N$ depend only on the concentrations of the chemical species at position x. At each grid point, the interactions between species form a proper chemical reaction network [64].

4.2.2 Existence and uniqueness of solutions

Global existence and uniqueness of solutions for reaction-diffusion systems of equations is a non-trivial problem and has been extensively studied. A good review of the state of the art can be found in reference [65]. In some instances, even if the solution exists for a local time, it can become unstable and diverge at a finite time $t < \infty$. Results for cases with high dimensionality, mixed boundary conditions or exponential reaction rates remain open problems. Fortunately, the system of PDEs described by equation (4.1) has some desirable properties, in particular:

1 quasi-positivity: $\forall \mathbf{C} \in \mathbb{R}^N, \forall i = 1...N, \quad Q_i(C_1, ..., C_{i-1}, 0, C_{i+1}, ..., C_N) \geq 0$

2 mass control structure: $\exists (a_i)_{1 \leq i \leq N}$ with $\forall i, a_i > 0$ s.t. $\forall \mathbf{C} \in \mathbb{R}^N, \sum_{1 \leq i \leq N} a_i Q_i(\mathbf{C}) \leq K$

3 2nd order kinetics: each $Q_i, i = 1...N$ is a polynomial of degree at most 2

The quasi-positivity property is easily deduced from the structure of our chemical equations. It simply states that the negative contributions to the reaction function of the ith species only come

from reactions or dissociations involving the ith species. This property ensures that a non-negative solution vector is preserved. The mass control structure property simply states that the chemical equations are balanced and so the mass of the system is under control. It can be derived for our system by choosing a_i such that a_i is the number of monomers of species i: $a_{He_xV_yI_z} = x + y + z$. In that case, the constant K is the sum of the production rates of each monomer. Note that the inequality $\sum_{1 \leq i \leq N} a_i Q_i(\mathbf{C}) < K$ is strict in our case due to the possible destruction of chemical species caused by vacancy-interstitial recombinations.
With these properties, it can be proven that at least for a one-dimensional system and for smooth inital data $C_i^{(0)}$, there exists a unique solution to (4.1) for any time t > 0 [66] [67].

4.2.3 Spatial Discretization

Since the spatial dependence in this system of equations is confined to the diffusion term and due to the simple 1-dimensional geometry considered here, it is appropriate to use the method of lines (MOL) to apply a finite difference discretization to the spatial term and consequently solve a (larger) system of Ordinary Differential Equations (ODEs). Using the notation $\mathbf{C}(x = p\Delta x) = \mathbf{C}^p$, a second order central difference scheme gives

$$\frac{\partial^2 \mathbf{C}}{\partial x^2}(x = p\Delta x) = \frac{1}{\Delta x^2}(\mathbf{C}^{p-1} - 2\mathbf{C}^p + \mathbf{C}^{p+1}) + O(\Delta x^2), \qquad p = 1, ..., M \tag{4.4}$$

The Dirichlet boundary conditions are $\mathbf{C}^0 = \mathbf{C}^{M+1} = 0$. Due to the expected large variations of concentration gradients in the spatial domain, it is also possible to use a non-uniform grid to be refined regions of large spatial gradients, at the possible cost of a loss in the order of accuracy for a two point stencil [68]. Since the analysis remains unchanged for a non-uniform grid, in the following discussion we will consider a uniform grid with mesh size Δx for clarity .
The resulting system of $N \times M$ ODEs has the form:

$$\frac{\partial \vec{C}}{\partial t} = A\vec{C} + \vec{Q}(\vec{C}) \tag{4.5}$$

where

$$\vec{C}(t) = \begin{pmatrix} \mathbf{C}^1(t) \\ \vdots \\ \mathbf{C}^M(t) \end{pmatrix}, \vec{Q}(\vec{C}) = \begin{pmatrix} \mathbf{Q}(\mathbf{C}^1(t)) \\ \vdots \\ \mathbf{Q}(\mathbf{C}^M(t)) \end{pmatrix}, \text{and } A = \frac{1}{\Delta x^2} \overbrace{\begin{pmatrix} \overbrace{-2\mathbf{D}}^{N} & \mathbf{D} & & \\ \mathbf{D} & -2\mathbf{D} & \mathbf{D} & \\ & \ddots & \ddots & \ddots \\ & & \mathbf{D} & -2\mathbf{D} \end{pmatrix}}^{N \times M}$$

The ordering choice of the species in the solution vector is first by type and second by position, and is dictated by the locality of the source term. This allows the use of efficient algorithms to solve the system of equations (4.5).

4.2.4 Numerical Scheme

In this section, we discuss the properties of the system of ODEs provided in equation (4.5) which will allow us to consider an appropriate numerical scheme.

Stiffness

The system of equations (4.5) is stiff. Stiffness occurs in a system when transient phenomena have different time scales. In this specific reaction-diffusion system of helium irradiation and implantation in tungsten, we expect significant stiffness since the diffusion, reaction and dissociation constants, and therefore timescales, vary by several orders of magnitude. Several measures of stiffness exist and are usually based on the eigenvalues of the Jacobian matrix or the Lipschitz constant of the operator function, and also depend on the time interval considered. It is possible to compute these eigenvalues based on the values of the parameters determined in reference [69].
For our diffusion operator, it is clear that for any induced norm: $\forall x, y \in \mathbb{R}^{N\times M}, ||Ay - Ax|| \leq ||A|||y - x|$. Taking for example the 1-norm, we obtain $||A||_1 = \max\limits_{1\leq j\leq N\times M} \sum\limits_{1\leq i\leq N\times M} |a_{ij}| = \frac{4}{\Delta x^2} \max\limits_{1\leq i\leq n} D_i$. Noting that in our system $\max\limits_{1\leq i\leq n} D_i > 10^{10} nm^2/s$ and $\Delta x^2_{min} \sim 1nm$,this results in a very large Lipschitz constant and so for any time interval of interest, the diffusion operator alone can be considered stiff.
For the reaction operator, we can split the reaction function $\vec{Q}$ to separate terms describing the dissociation reactions $\vec{Q_d}$ and the clustering reactions $\vec{Q_r}$. Let us consider first the dissociation term $\vec{Q_d}$, which consists only of first order reaction kinetics, so each $(Q_d)_i$ is a first order polynomial of $(C_i, ..., C_n)$. Each species undergoing a dissociation reaction splits into at most two other species, and each species can only undergo at most three different dissociation reactions (helium dissociation, vacancy dissociation and trap mutation) in our model, so we can bound the variations of the dissociation operator as:

$$\forall \vec{C}, \vec{\tilde{C}} \in \mathbb{R}^{N\times M},$$
$$||\vec{Q_d}(\vec{C}) - \vec{Q_d}(\vec{\tilde{C}})||_1 \leq 3 \sum_{1\leq i\leq N} \sum_{1\leq p\leq M} (k^{he}_{d_i} + k^{v}_{d_i} + k^{trap}_{d_i})(C^p_i - \tilde{C}^p_i) \leq 3k_{max}||\vec{C} - \vec{\tilde{C}}||_1 \quad (4.6)$$

where $k_{max} = \max\limits_{1\leq i\leq N}(k^{he}_{d_i} + k^{v}_{d_i} + k^{trap}_{d_i}) > 10^{10} s^{-1}$ so that the dissociation operator is stiff as well.
The case of the reaction part $\vec{Q_r}$ is more difficult, since it is a quadratic polynomial of $(C_1, ..., C_n)$, such that the Lipschitz constant depends on the size of the interval considered, or equivalently, the eigenvalues of the Jacobian depend on the $(C_1, ..., C_n)$. Numerical experiments performed on our model system show that the eigenvalues of the Jacobian of the reaction part are always real and negative, and moreover the absolute value of the maximum eigenvalue grows linearly with $||\vec{C}||$, which is expected since the reaction part consists of polynomials of order 2. The reaction operator can therefore become arbitrarily stiff as concentrations increase.

SDIRK schemes

Based on the above stiffness considerations, we select an implicit scheme to solve (4.5). Since both reactions and diffusion operators are extremely stiff, schemes often used for reaction-diffusion problems such as operator splitting or Implicit-Explicit (IMEX) schemes which decouple the operators are not appropriate in this case and we have chosen a fully implicit scheme.
Runge-Kutta (RK) is a class of numerical methods commonly used to solve stiff ODEs [13]. Consider an ODE of the form

$$y' = f(t, y) \ , \quad y(t = 0) = y_0 \ , \quad y \in \mathbb{R}^N \tag{4.7}$$

A Runge-Kutta scheme applied to this ODE is a one-step method which computes the solution $y(t + \Delta t)$ from the solution $y(t)$ using s stages

$$k_i = f(t + c_i \Delta t, y(t) + \Delta t \sum_{j=1}^{s} a_{ij} k_j) \ , \quad i = 1, \dots, s \tag{4.8}$$

$$y(t + \Delta t) = y(t) + \Delta t \sum_{j=1}^{s} b_j k_j \tag{4.9}$$

where the number of stages s and the coefficients a_{ij},b_i and c_i are a characteristic of the RK scheme and often displayed as a Butcher tableau of the form

$$\begin{array}{c|ccc} c_1 & a_{11} & \dots & a_{1s} \\ \vdots & \vdots & & \vdots \\ c_s & a_{s1} & \dots & a_{ss} \\ \hline & b_1 & \dots & b_s \end{array} \tag{4.10}$$

A particular class of RK methods where all the diagonal coefficients a_{ii} are equal and non-zero, and all the above-diagonal coefficients are zero was introduced by Nørsett [70]. These methods are called Single Diagonally Implicit Runge-Kutta (SDIRK). An example of a Butcher tableau for a 5-stage SDIRK scheme is shown in figure 4.1. SDIRK schemes allow for computing each stage value k_i successively, since these only depend on previously computed quantities. Moreover, solving the non-linear equations for each stage value using a SDIRK method is greatly simplified by the possibility to re-use the same Jacobian matrix due to the constant value of the diagonal coefficients, a feature discussed in more detail in section 4.3.2. SDIRK methods also provide a very efficient implementation of parallel algorithms as discussed in the next section. Thus, we believe SDIRK methods represent a good trade-off between computational efficiency and accuracy, and are commonly used to solve problems arising from semi-discretization of non-linear parabolic PDEs such as reaction-diffusion equations, where only moderate accuracy is required. The choice of a specific SDIRK scheme based on convergence properties is discussed in section 4.4.2.

$\frac{1}{4}$	$\frac{1}{4}$				
$\frac{3}{4}$	$\frac{1}{2}$	$\frac{1}{4}$			
$\frac{11}{20}$	$\frac{17}{50}$	$-\frac{1}{25}$	$\frac{1}{4}$		
$\frac{1}{2}$	$\frac{371}{1360}$	$-\frac{137}{2720}$	$\frac{15}{544}$	$\frac{1}{4}$	
1	$\frac{25}{24}$	$-\frac{49}{48}$	$\frac{125}{16}$	$-\frac{85}{12}$	$\frac{1}{4}$
$y_1 =$	$\frac{25}{24}$	$-\frac{49}{48}$	$\frac{125}{16}$	$-\frac{85}{12}$	$\frac{1}{4}$
$\widehat{y}_1 =$	$\frac{59}{48}$	$-\frac{17}{96}$	$\frac{225}{32}$	$-\frac{85}{12}$	0
$err =$	$-\frac{3}{16}$	$-\frac{27}{32}$	$\frac{25}{32}$	0	$\frac{1}{4}$

Figure 4.1: Butcher tableau for the L-stable SDIRK method of order 4, as reproduced from Ref [13]

4.3 Implementation

The Implementation of a SDIRK scheme to solve the system of equations (4.5) is difficult. The number of species N can easily be as large as $N = 10,000$ or greater. A grid containing 100 mesh points results in $N \times M > 1,000,000$ unknowns. Thus, two computational issues arise; namely, data memory management and computational efficiency. Fortunately, both issues can be alleviated by the use of parallel algorithms. In particular, we make use of the known sparsity pattern of the source term and its Jacobian, the locality of the source term, and the fact that only a few species n (with $n << N$) diffuse in the material.

4.3.1 Algorithm

SDIRK algorithm

SDIRK numerical schemes split each time step into s stages (s = 5 for the Hairer and Wanner scheme given as an example in figure 4.1). Let $\vec{C}^n$ be the solution vector at time $t = n\Delta t$ and let $f : \mathbb{R}^{N\times M} \to \mathbb{R}^{N\times M}$ with $f(\vec{C}) = A\vec{C} + \vec{Q}(\vec{C})$ such that $\frac{\partial \vec{C}}{\partial t} = f(\vec{C})$, the same form as equation 4.7. Each stage i consists of solving a non-linear equation in the unknown k_i since the $k_{j<i}$ are already computed at the previous stages as:

$$F(k_i) = k_i - f\left(\vec{C}^n + \Delta t \sum_{j=1}^{i-1} a_{ij}k_j + \gamma\Delta t k_i\right) = 0 \quad , \tag{4.11}$$

where the a_{ij} are the coefficients of the Butcher tableau and γ is the constant diagonal coefficient. Solving the non-linear equation (4.11) is done by applying Newton's iteration method. Starting with an initial guess $k_i^{(0)}$, the iteration sequence $k_i^{(l)}$ is computed as

$$\begin{aligned} &1. \quad \text{solve} && F'(k_i^{(l)})\Delta k_i^{(l)} = -F(k_i^{(l)}) \\ &2. \quad \text{increment} && k_i^{(l+1)} = k_i^{(l)} + \Delta k_i^{(l)} \\ &3. \quad \text{stop if} && \frac{\Delta k_i^{(l)}}{k_i^{(l)}} < \varepsilon \quad , \end{aligned} \tag{4.12}$$

where ε is a relative tolerance parameter for the stopping criterion and $F'(k_i^{(l)})$ is the Jacobian of F computed at $k = k_i^{(l)}$. The Jacobian has the following form:

$$\begin{aligned} F'(k_i^{(l)}) &= I - f'\left(\vec{C}^n + \Delta t \sum_{j=1}^{i-1} a_{ij}k_j + \gamma\Delta t k_i^{(l)}\right) \\ &= I - \gamma\Delta t\left(A + Q'\left(\vec{C}^n + \Delta t \sum_{j=1}^{i-1} a_{ij}k_j + \gamma\Delta t k_i^{(l)}\right)\right) \\ &= I - \gamma\Delta t J \end{aligned} \tag{4.13}$$

where $J = A + Q'\left(\vec{C}^n + \Delta t \sum_{j=1}^{i-1} a_{ij}k_j + \gamma\Delta t k_i^{(l)}\right)$ and Q' is the Jacobian matrix of the local source term $\vec{Q}$ and is therefore a block-diagonal matrix.
The implementation of a SDIRK scheme leads to repeatedly solving linear systems of the form

$$(I - \gamma\Delta t J)X = -F(k_i^{(l)}) \tag{4.14}$$

Three main operations thus influence the data memory management and computational efficiency: evaluating the operator function $-F$, computing the Jacobian matrix J, and solving the linear system $(I - \gamma\Delta t J)X = -F$.

Jacobian and operator function evaluation

The large majority of the computational work in the operator function evaluation is spent on the source term, as the reaction network is relatively complex while the diffusion process on the grid is straightforward. Since this source term is local, we can make use of distributed memory architectures within MPI for space decomposition. This form of parallelism alleviates two main concerns: First, the operator function evaluation is embarrassingly parallel since no communication is required between processors in order to compute the source term at any grid point. For the diffusion operator, communication of the solution vector for mobile species is only required from the neighboring processors, and it is usually negligible compared to the work involved in computing the local source term. Second, each processor only needs to store the data of the solution vector and function on the local part of the mesh it is assigned to (and the neighboring solution vectors for mobile species). This significantly lowers the memory requirement for each processor.
The case of the Jacobian computation is similar, since using a spatial decomposition allows each processor to compute and form its own block diagonal Jacobian of the source term $\vec{Q}$ and store it, which provides similar benefits in memory requirement and computational efficiency as above.

Linear system

The case of the linear system solve is more complex. The matrix $(I - \gamma\Delta t J)$, with $J = A + Q'$ is block-tridiagonal with a sparsity pattern that we need to take advantage of in order to efficiently solve the linear system:

$$(I-\gamma\Delta t J) = \overbrace{\begin{pmatrix} \overbrace{I-\gamma\Delta t\mathbf{Q}'_1+\frac{2\gamma\Delta t}{\Delta x^2}\mathbf{D}}^{N} & -\frac{\gamma\Delta t}{\Delta x^2}\mathbf{D} & & \\ \frac{\gamma\Delta t}{\Delta x^2}\mathbf{D} & \ddots & & \\ & \ddots & & -\frac{\gamma\Delta t}{\Delta x^2}\mathbf{D} \\ & -\frac{\gamma\Delta t}{\Delta x^2}\mathbf{D} & & I-\gamma\Delta t\mathbf{Q}'_M+\frac{2\gamma\Delta t}{\Delta x^2}\mathbf{D} \end{pmatrix}}^{N\times M} \tag{4.15}$$

Since the diagonal matrix $\mathbf{D} = diag\overbrace{(D_1, \dots, D_n, 0, \dots, 0)}^{N}$ only consists of the diagonal coefficients of the n mobile species with $n << N$, the fact that only n equations in the system (4.1) are PDEs now clearly appears in the linear system as the fact that only n species are coupled between blocks of the matrix $(I-\gamma\Delta t J)$ above. In other words, we can take advantage of the fact that our original system of equations (4.1) is mostly an ODE system in order to efficiently solve (4.14).
In order to decouple the mobile and non-mobile species, we use a version of the SPIKE algorithm [71] adapted to our problem, which can also be considered as a form of Block-Jacobi preconditioning:
Consider the block diagonal matrix $T = diag(T_1, \dots, T_M)$ where $T_p = I - \gamma\Delta t\mathbf{Q}'_p + \frac{2\gamma\Delta t}{\Delta x^2}\mathbf{D}$ for

$p = 1, \dots, M$. We can use T^{-1} as a left preconditioner for the system (4.14):

$$\begin{aligned} & (I - \gamma \Delta t J)X = -F \\ \iff \quad & T^{-1}(I - \gamma \Delta t J)X = -T^{-1}F \\ \iff \quad & SX = G \end{aligned} \tag{4.16}$$

The matrix S in (4.16) is called the spike matrix and has the following structure:

$$S = \overbrace{\begin{pmatrix} \overbrace{I}^{N} & V_1 & & & \\ W_2 & I & V_2 & & \\ & \ddots & \ddots & \ddots & \\ & & W_M & & I \end{pmatrix}}^{N \times M} \tag{4.17}$$

The matrices V_p and W_p for $p = 1, \dots, M$ are called the spikes and can be computed along with the right hand side $G = (G_1, \dots, G_M)^T$ by solving the following independent linear systems:

$$\left.\begin{aligned} (I - \gamma \Delta t \mathbf{Q}'_p + \frac{2\gamma \Delta t}{\Delta x^2}\mathbf{D})W_p &= \frac{\gamma \Delta t}{\Delta x^2}\mathbf{D} \\ (I - \gamma \Delta t \mathbf{Q}'_p + \frac{2\gamma \Delta t}{\Delta x^2}\mathbf{D})V_p &= \frac{\gamma \Delta t}{\Delta x^2}\mathbf{D} \\ (I - \gamma \Delta t \mathbf{Q}'_p + \frac{2\gamma \Delta t}{\Delta x^2}\mathbf{D})G_p &= -F \end{aligned}\right\} \qquad \text{for } p = 1, \dots, M. \tag{4.18}$$

Note that in the uniform grid case the $N \times N$ matrices $V_p = W_p$ for $p = 2, \dots, M-1$, but this is not necessarily true for a non-uniform grid. In the latter case, let the centered spatial discretization be $\frac{\partial^2 \mathbf{C}^p}{\partial x^2} = \alpha(p)\mathbf{C}^{p-1} + \beta(p)\mathbf{C}^p + \delta(p)\mathbf{C}^{p+1}$. Then we simply have $V_p = \frac{\delta(p)}{\alpha(p)}W_p$.

Due to the structure of $\mathbf{D}$, only the n leftmost columns of the $N \times N$ matrices V_p and W_p are non-zeros, hence the name 'spikes'. We can extract an independent subsystem from the linear system (4.16) consisting of only the n mobile species. We call that system the reduced system. Specifically, let

$$V_p = \begin{pmatrix} V_p^{(n)} & 0 \\ V_p^{(N-n)} & 0 \end{pmatrix}, W_p = \begin{pmatrix} W_p^{(n)} & 0 \\ W_p^{(N-n)} & 0 \end{pmatrix} \text{ and } G_p = \begin{pmatrix} G_p^{(n)} \\ G_p^{(N-n)} \end{pmatrix} \tag{4.19}$$

where $V_p^{(n)}$ and $W_p^{(n)}$ are matrices of dimension $n \times n$, $V_p^{(N-n)}$ and $W_p^{(N-n)}$ are matrices of dimension $(N-n) \times n$, $G_p^{(n)}$ is a column vector of dimension n and $G_p^{(N-n)}$ is a column vector of dimension $N - n$. The reduced system is then:

$$\tilde{S}\tilde{X} = \tilde{G} \quad , \tag{4.20}$$

and the reduced spike matrix $\tilde{S}$ and right hand side vector $\tilde{G}$ are now:

$$\tilde{S} = \overbrace{\begin{pmatrix} \overbrace{I}^{n} & V_1^{(n)} & & \\ W_2^{(n)} & I & V_2^{(n)} & \\ & \ddots & \ddots & \ddots \\ & & W_M^{(n)} & I \end{pmatrix}}^{n \times M} \text{ and } \tilde{G} = \begin{pmatrix} G_1^{(n)} \\ \vdots \\ G_M^{(n)} \end{pmatrix} \tag{4.21}$$

Once the solution $\tilde{X} = (X_1^{(n)}, ..., X_M^{(n)})$ to the reduced system (4.20) is known, we can then recover the solution of the original system (4.14) using:

$$X_p^{(N-n)} = G_p^{(N-n)} - W_p^{(N-n)} X_{p-1}^{(n)} - V_p^{(N-n)} X_{p+1}^{(n)} \tag{4.22}$$

To summarize, solving the $N \times M$ linear system of equations given by equation (4.14) requires three steps:

1. compute the spikes using (4.18)
2. solve the $n \times M$ reduced system (4.20)
3. Recover the solution using (4.22)

Steps 1 and 3 can be performed with perfect space parallelism. Step 2 solves the dense block-tridiagonal system obtained from a spike reduction. While several methods exist to efficiently solve such systems [71] [72], in the case of cluster dynamics modeling of helium and hydrogen diffusion and bubble growth, the reduced system of n mobile species is small enough to be solved using a simple algorithm such as a direct LU factorization since in general $n < 100$ while $N > 10,000$. Therefore, we expect that solving the reduced system will not be a computational bottleneck.

4.3.2 Practical Implementation

Simplified Newton iteration

Each Newton iteration involves solving the linear system 4.14, in which the Jacobian,

$$I - \gamma \Delta t J = F'(k_i^{(l)}) = I - f' \left(\vec{C}^n + \Delta t \sum_{j=1}^{i-1} a_{ij} k_j + \gamma \Delta t k_i^{(l)} \right) \quad ,$$

must be evaluated at each Newton iteration. We use a simplified Newton iteration scheme [73] in which the Jacobian is kept constant for all Newton iterations ($I - \gamma \Delta t J = F'(k_i^{(0)})$) or even for all stages ($I - \gamma \Delta t J = F'(k_1^{(0)})$). The initial guesses $k_i^{(0)}$ are extrapolated from the final values of the previous stages using the method developped by Hairer et al. [13].
This simplified Newton iteration scheme allows computing the Jacobian and the spikes only once per time step, which provdes a very large gain in computational efficiency.

Operator function evaluation

The operator function must also be evaluated at each Newton iteration. The evaluation of the diffusion operator represents a negligible amount of work compared to the reaction operator. Evaluating the local reaction operator $\mathbf{Q}(\mathbf{C}^p)$ at a given grid point p can be done efficiently by looping over the $n \times N$ reactions (instead of looping over each species individually) and updating the value of the reaction operator for each species involved in the reaction. As an example, in a standard reaction

$$\mathrm{A} + \mathrm{B} \underset{k^-_{AB}}{\overset{k^+_{A,B}}{\rightleftharpoons}} \mathrm{AB}, \tag{4.23}$$

the value of the reaction operators are updated as:

$$\begin{aligned} Q_{AB} &= Q_{AB} + k^+_{A,B} C_A C_B - k^-_{AB} C_{AB} \\ Q_A &= Q_A - k^+_{A,B} C_A C_B + k^-_{AB} C_{AB} \\ Q_B &= Q_B - k^+_{A,B} C_A C_B + k^-_{AB} C_{AB} \end{aligned} \tag{4.24}$$

The same approach can be used to evaluate the Jacobian at each time step, and thus only 6 entries of the Jacobian are updated for each reaction.

Spikes Computation

Computing the spikes using the approach outlined by equation (4.18) involves solving $n+1$ linear systems of size $N \times N$ on each grid point p for the spikes V^p and W^p and the right hand side G^p. Using a simplified Newton iteration scheme, the Jacobian, and hence the spikes V^p and W^p, have to be computed only once per time step. However, a linear system of size $N \times N$ remains to be solved on each grid point p at each Newton iteration to compute the right hand side G^p. Therefore, we choose to compute a LU factorization of each diagonal block of the Jacobian at the beginning of every time step to speed-up the computation of the right hand side during the following Newton iterations.

We can then take advantage of the chemical reaction network structure within each diagonal block of the Jacobian, so that the extensive literature for optimization of chemical reaction systems can be used. First, we perform a species reordering: the ordering chosen for the species in the solution vector has an important role in the LU factorization and especially in the resulting fill-in. Different types of reordering have been studied in reference [74], showing that the intuitive reordering based on the reactivity of the species is not the most efficient method to minimize fill-in. Therefore, we use the ParMETIS package [75] to compute fill-reducing orderings of the Jacobian diagonal blocks. Second, we make use of the known chemical network sparsity pattern since the chemical network is known in advance of computation. We compute offline a maximum sparsity pattern for the diagonal blocks of the Jacobian and perform a symbolic LU factorization [76]. Only the numeric LU factorization will then have to be performed during any time step iteration.

Error measurement and clipping

The SDIRK algorithm computes the solution vector $\vec{C}$ at time $t + \Delta t$ which contains the concentrations C_i^p of all the species i at all the positions $x = p\Delta x$; it also gives an estimate of the local truncation error $\vec{e}$. A scalar measure of the truncation error is then computed, as in reference [77]:

$$E_p = \sqrt{\frac{1}{N}\sum_{i=1}^{N}\left(\frac{e_i^p}{atol_i + rtol_i|C_i^p|}\right)^2} \tag{4.25}$$

and

$$E = \sqrt{\sum_{p=1}^{M} E_p^2 \Delta x} \tag{4.26}$$

where $atol_i$ and $rtol_i$ are user-specified tolerances for the species i. The time step is accepted if $E < 1$. However, very small, negative values of the concentrations of some species due to numerical errors can produce a relatively small error and be accepted during a time step. These unphysical negative values in the concentrations can lead to catastrophic results due to numerical oscillations. A simple way to deal with this problem is to use clipping, that is, to set the small negative values of the concentrations to zero. Clipping presents the disadvantage of not preserving mass conservation in the reaction-diffusion equations. Therefore, more complex projection methods have been developed to deal with this issue [77]. In our case, clipping is found to have a negligible influence on mass conservation and therefore we have thus used the simple clipping method to deal with negative concentrations.

Summary

Figure 4.2 provides a summary of the algorithm described above. Note that the only steps requiring communication between data on the grid are the reduced system step and the diffusion operator evaluation.

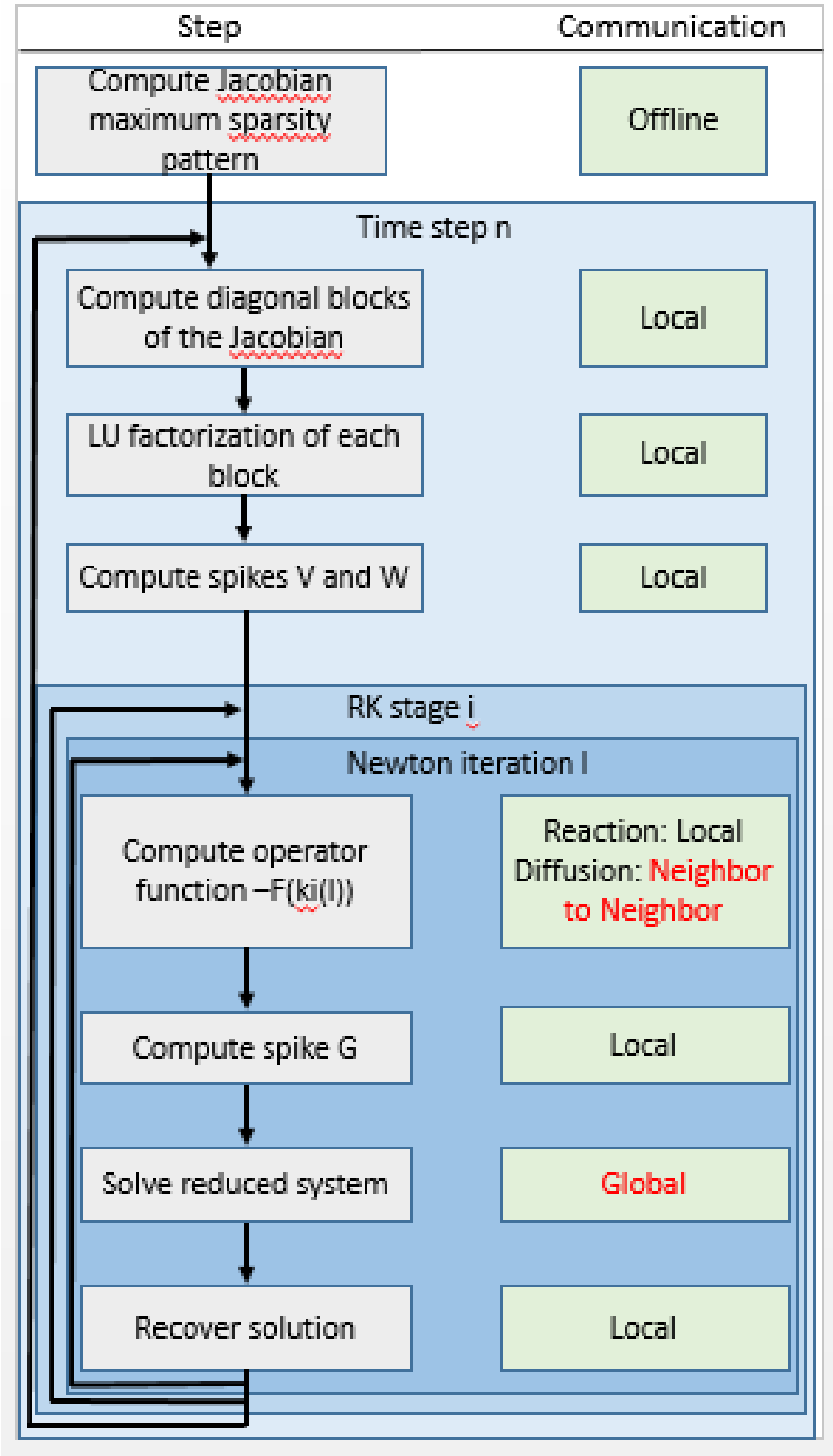


Figure 4.2: Schematic diagram of the algorithm. Local steps do not require any form of grid-to-grid communication.

4.4 Results

4.4.1 Standard cases

We define two standard cases relevant to fusion reactors in order to illustrate the results obtained with our implementation of a SDIRK scheme to the reaction-diffusion problem specified by equation (4.1).
The first case (problem A) has a tendril-like geometry with Dirichlet boundary conditions at $x = 0$ and $x = 30$ nm, and is representative of the observed tungsten "nanofuzz", a nanometer sized fiber structure [8]. Since we want to use this case to illustrate the convergence issues due to stiffness, we only consider a small number of species ($N = 57$, from a single helium interstitial to the largest species being $He_{20}V_3$) with a pre-existing concentrations of vacancies $C_V = 10^{-6}$ nm^{-3} which will act as a trap for implanted helium and ensures that both reactions and diffusion of mobile species occur during the simulation time. Figure 4.3 shows the resulting concentration of the species after 5×10^{-4} seconds of helium implantation.

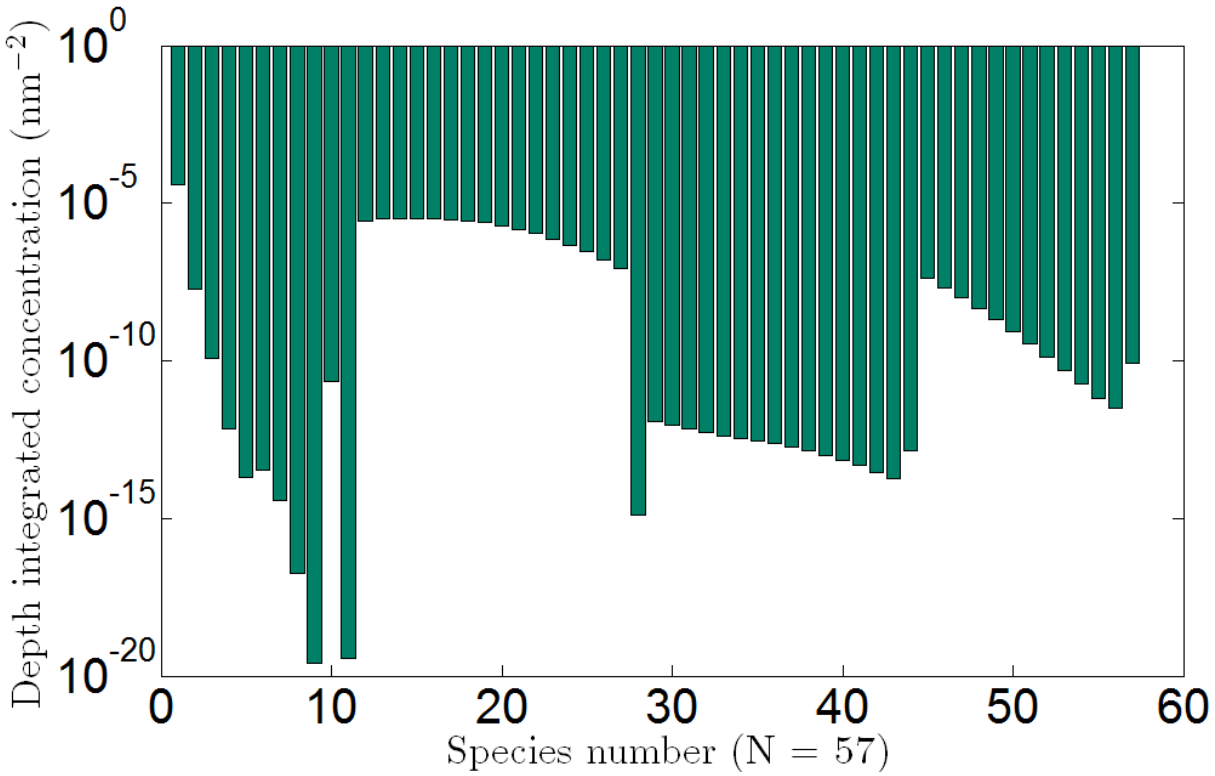


Figure 4.3: Case A results (Depth integrated concentration of all species modeled).

The second case (problem B) evaluates a half-slab geometry (semi-infinite slab with Dirichlet boundary conditions at $x = 0$), and illustrates the numerical and memory issues encountered in

cluster dynamics modeling. The very high fluxes of incident helium particles is responsible for the rapid clustering into helium-vacancy clusters and a large number of species to be considered. High temperatures are responsible for both fast diffusion and large reaction constants.
The physical results for these two cases are described in greater detail in chapter 6.

Table 4.1: Parameters used in the standard case.

Parameter	Problem A	Problem B
Incident helium flux	10^{22} m^{-2}s^{-1}	2.4×10^{22} m^{-2}s^{-1}
simulation time	5×10^{-4} sec	1000 sec
Temperature	1000 Kelvin	2000 Kelvin
grid length	30 nm	semi-infinite
Number of grid meshes M	100	200
Number of mobile species n	10	25
Number of species N	57	2782

4.4.2 Convergence of SDIRK algorithms

Several properties affect the stability and convergence behavior of SDIRK numerical schemes. Reference [13] provides a detailed definition of the concepts of A-,L- and S-stability for stiff ODE systems. Since in reaction-diffusion systems, the Jacobian eigenvalues are real negative and can become arbitrarily large, the selected SDIRK scheme should be at least A-stable and preferentially L-stable to efficiently deal with extremely large eigenvalues.
However, stiffness does not only affect stability properties of the numerical schemes. The phenomenon of order reduction was first shown in reference [78]. For stiff problems, the order of convergence of a numerical scheme can indeed be lower than the classical order of convergence of the method. This led to the development of the theory of B-convergence [79] and B-stable schemes [80]. Unfortunately, SDIRK schemes can only have an order of B-convergence which is at most 2, and this means that for very stiff systems we can only expect a convergence order of 2 even for schemes with higher classical order.
We study the convergence of several SDIRK schemes using the problem A defined in section 4.4.1 above. The error is measured using an expression similar to the one in section 4.3.2:

$$E_p = \sqrt{\frac{1}{N}\sum_{i=1}^{N}\left(\frac{Cref_i^p - C_i^p}{atol_i + rtol_i|Cref_i^p|}\right)^2} \tag{4.27}$$

and

$$E = \sqrt{\sum_{p=1}^{M} E_p^2 \Delta x} \tag{4.28}$$

where the accuracy is $rtol_i = 10^{-3}$ and $atol_i = 10^{-10}$, and C_{ref} is the reference solution computed using the highest order scheme (classical order 4) and the lowest time step ($\Delta t = 10^{-10}$ sec).

Table 4.2 shows the SDIRK schemes used in the convergence tests performed on problem A, as well as the reference to their original article and their respective properties and observed order of convergence. Figure 4.4 shows the results of the convergence tests for all the SDIRK schemes given in table 4.2. As expected, we see that the stiffness of our problem indeed reduced the order of convergence of all SDIRK schemes to 2, regardless of their classical order of convergence. Thus, there is a trade-off between the choice of SDIRK schemes which exhibit a low order of convergence and the efficiency gains expected from the implementation in section 4.3. Nevertheless, for the solution of semi-discretized PDE problems where relatively low accuracy is needed, this trade-off can be beneficial.

Table 4.2: SDIRK schemes used in this work and order of convergence results.

SDIRK scheme name	number of stages	Properties	Classical order of convergence	Observed order of convergence
HW4 [13]	5	L-stable	4	2.13
A4 [81, 82]	5	S-Stable	4	1.96
B4 [80]	3	Algebraically-stable	4	1.99
A3 [82]	3	S-stable	3	2.06
B2 [80]	2	L-stable	2	2.05

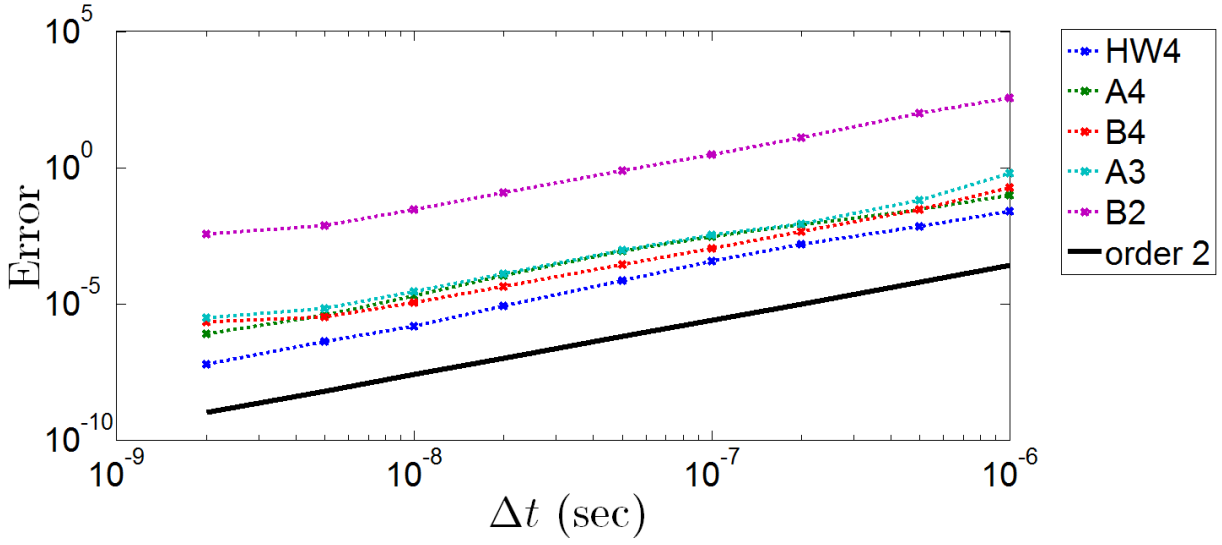


Figure 4.4: Convergence results for several SDIRK schemes on test problem A.

4.4.3 Parallel Performances

In this section, we discuss the parallel performance of the algorithm introduced in section 4.3 and summarized in Figure 4.2. This algorithm splits most of the problem into independent local subproblems. Therefore, we use a distributed memory architecture with a Message Passing Interface (MPI) so that each processor independently deals with local data. Our algorithm limits the amount of communication per processor to $O(n)$ floating point numbers to evaluate the diffusion operator, and $O(M \times n^2)$ floating point numbers to solve the non-parallel reduced system. Hence, we expect excellent parallel performance up to the point when the reduced system step becomes dominant. The computational system used on NERSC is Hopper, a Cray XE6 system.

Strong Scaling

We have used the parallel algorithm on test problem B for an increasing number of processors. Speedup S can be defined as

$$S_p = T_p/T_1 \tag{4.29}$$

where T_1 is the serial time of execution and T_p is the time of execution of the program running on a distributed memory architecture with p processors. Figure 4.5 shows the results of our parallelization strategy. We observe excellent parallel performance up to the point where the number of processors is close to the maximum number of grid points ($M = 200$ in the test problem B). At this point, the communication to computation ratio increases, while at the same time the serial computational time needed for the reduced system step is no longer negligible. Both these features are responsible for the slow down of parallel performance at the limit of one processor per grid point. Nevertheless, the parallel efficiency remains above 50% even in the worst case. Increasing the strong scaling efficiency past this value would require an appropriate parallelization of the reduced system step, using algorithms such as block cyclic reduction algorithms [83].

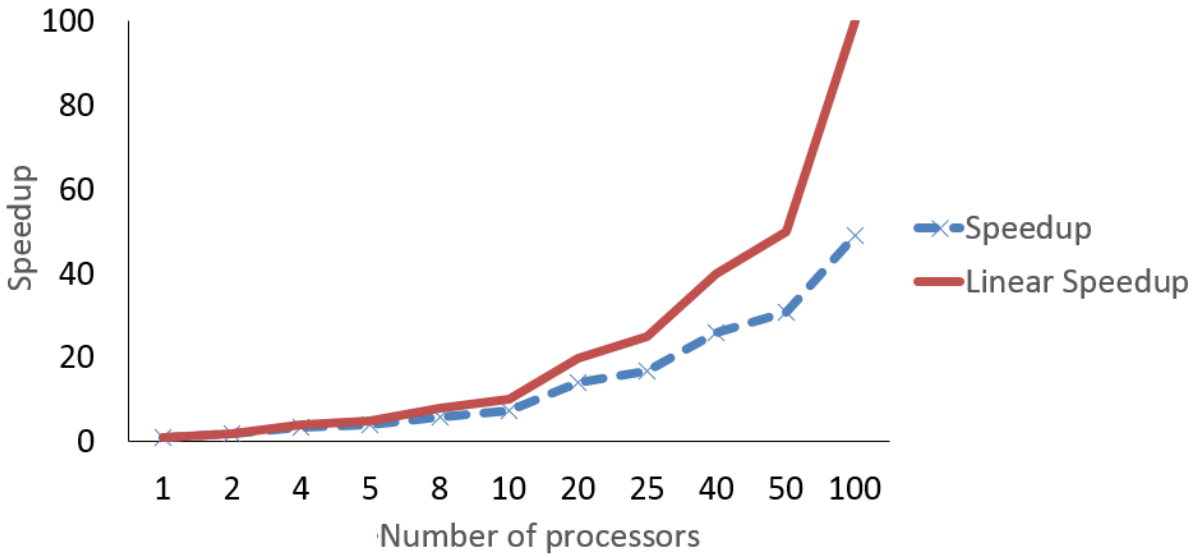


Figure 4.5: Strong scaling results for the test problem B. Linear speedup indicates the ideal case in which $S_p = p$.

Weak Scaling

We now perform a numerical experiment in which the number of grid points M is increasing with a constant number of grid points per processor. Figure 4.6 shows the results of this weak scaling simulation. We observe excellent parallel performance up to several hundred processors. The weak scaling efficiency decreases significantly for a very large number of processors ($N_p \geq 500$), due to the non-parallel reduced system step becoming dominant. These results suggest the use of this algorithm to extend the code to a two- or three-dimensional model, since the split strategy between local reactions and global diffusion naturally extends to higher spatial dimensions.

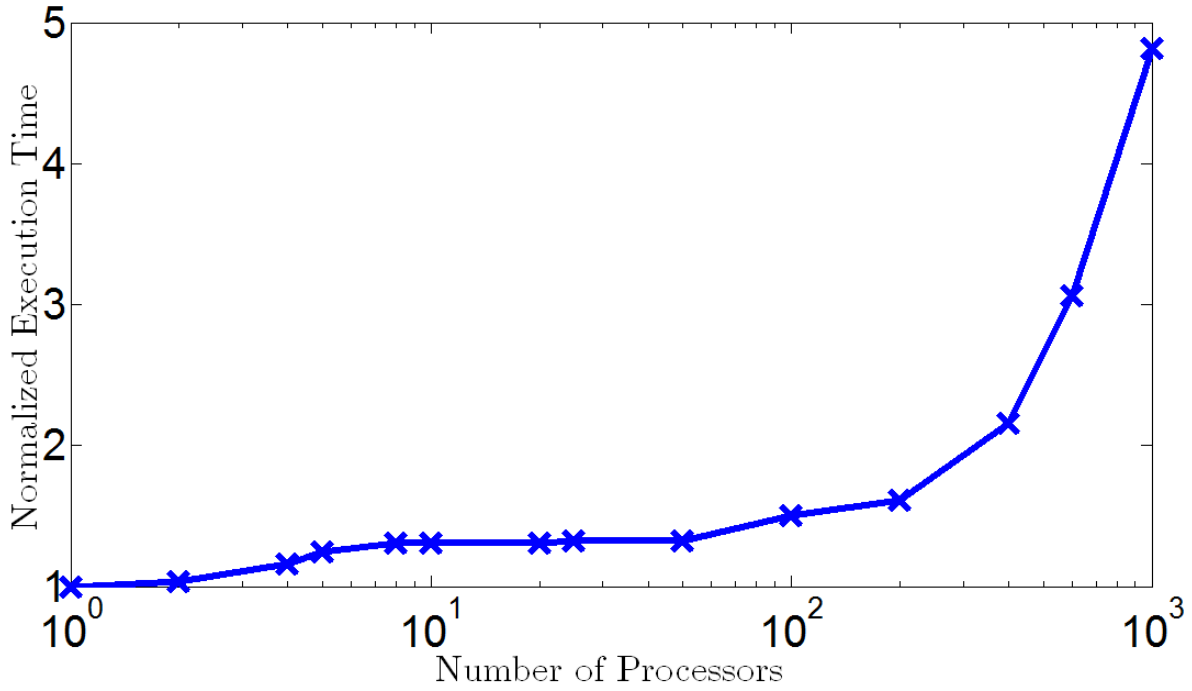


Figure 4.6: Weak scaling results for test problem B with 10 grid points per processor

Conclusion

An efficient solver for large systems of stiff reaction-diffusion equations with few diffusing species was introduced. The solver uses a Single Diagonally Implicit Runge-Kutta scheme to deal with the stiffness of both the diffusion and reaction terms. The order of convergence of every SDIRK scheme tested suffers from the stiffness of the system of reaction-diffusion equations and is reduced to two regardless of the classical order of convergence of each scheme. The implementation uses block decomposition of the Jacobian and the spike algorithm in order to decouple diffusion and reaction. This form of data level parallelism exhibits very good parallel performance. By decoupling the reaction from the diffusion, it is also possible to use optimizations developed specifically for chemical reaction networks. Weak scaling results on spatial parallelization suggest the use of this algorithm to solve similar reaction-diffusion systems in higher spatial dimensions.

Chapter 5

Cluster Dynamics Model validation

In this chapter, the cluster dynamics model prdictions are discussed and benchmarked by comparing to experimental results. These results are chose so that the number of species considered and parameters used remains relatively small, so that we can build some confidence in the processes modeled for a relatively small system size.

5.1 Comparison with experimental results

5.1.1 Experimental conditions modeled in this work

The Thermal Helium Desorption Spectrometry (THDS) experiments from Kornelsen [14] provide useful data in order to benchmark and compare the cluster dynamics model. A THDS experiment is performed in two steps. First, helium is implanted at a given flux and energy in the material sample to study (which might have been already damaged by previous irradiation) at room temperature. In the second step, the helium implantation is stopped and the material sample is moved to the THDS vacuum chamber. There, a temperature ramp increase is performed. During that step, the dissolved helium concentration is measured by a mass spectrometer. During THDS experiments, it is observed that large helium desorption peaks appear at certain temperatures, which are called desorption peak temperatures. We have modeled this experiment using the cluster dynamics code which solves the system of equations introduced in chapter 2.
Kornelsen first performed Krypton ion irradiation experiments to create displacement damage. The effect of Kr binding to vacancies and helium on THDS has been studied [33, 34] and is not expected to play a major role for the low Kr^+ implantation dose of $8 \times 10^{15}/m^2$, as is the case here. While Krypton does not play a major role at these low fluences, it does bind to vacancies and helium complexes, and several possible reactions have been proposed, as noted in table 3.5. However, in our model, we have not explicitly included Krypton, and therefore we will observe a discrepancy where species containing Krypton are believed to be involved.
Figure 5.1 shows the THDS spectrum observed by Kornelsen in tungsten. Heavy ion bombardment by Krypton ions of energy 5 keV to a fluence $8 \times 10^{15}/m^2$ was first used to generate displacement

damage. The resulting point defects act as traps during the helium implantation performed with 250 eV He ions to a fluence of $8 \times 10^{16}/m^2$ .Thermal desorption was then performed at a heating rate of 40 K/s which generated the helium desorption spectrum that has been reproduced in figure 5.1. The spectrum can be interpreted and each peak can be assigned to a specific reaction, as done by Kornelsen et al.. These values are provided in table 5.1.

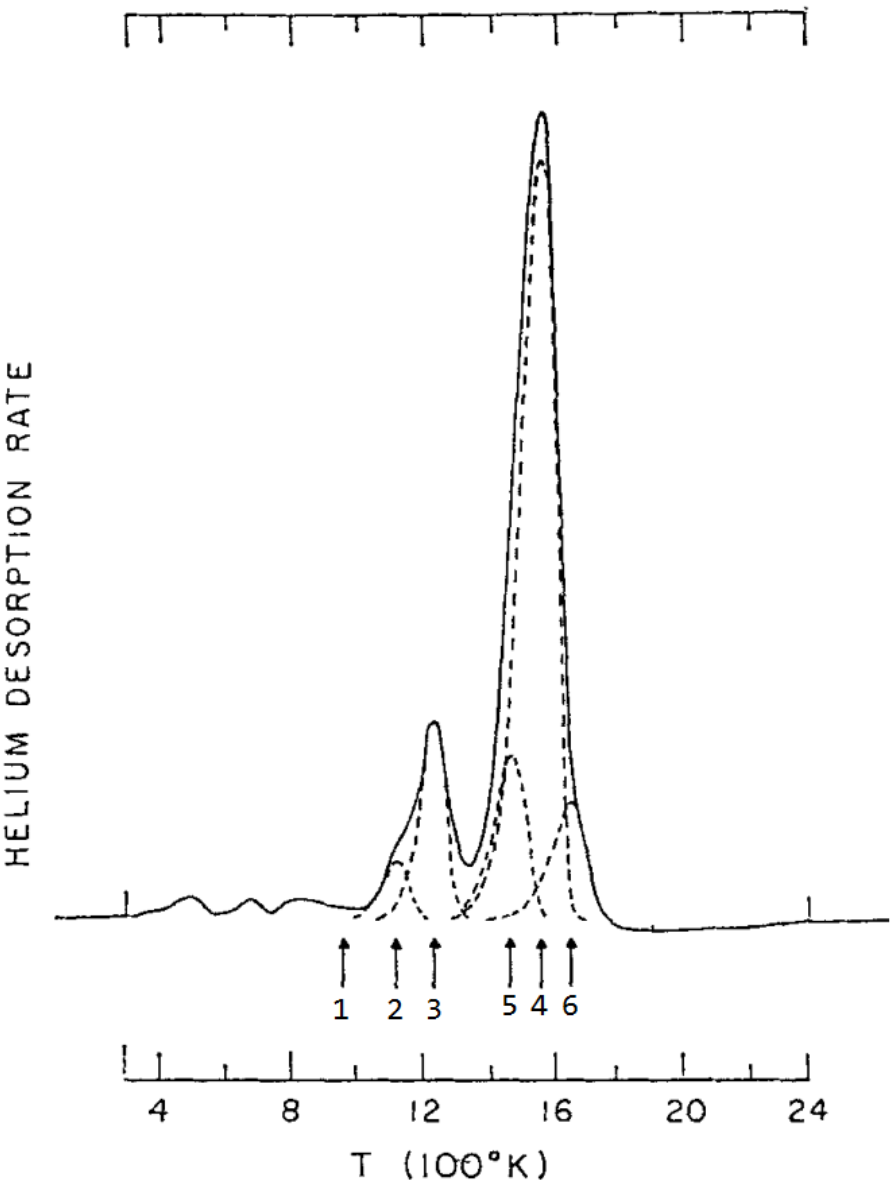


Figure 5.1: THDS spectrum reproduced from Kornelsen [14] obtained after 5 keV Kr^+ irradiation to a fluence of $8 \times 10^{15}/m^2$, followed by 250 eV He^+ implantation to a fluence of $8 \times 10^{16}/m^2$ at room temperature. The dashed lines indicate the assumed reactions that can describe the observed desorption peaks.

Table 5.1: Summary of dissociation events for small He_xV_y clusters, and associate binding energies, as obtained from analysis of experimental THDS measurements [14] or theoretical modes [17, 18] .

Reaction	Description	Experimental analysis of Kornelsen [14] (Desorption peak and binding energy)	Theoretical analysis of Wilson [18]	Theoretical analysis of Casper
1	$He_4V \rightarrow He + He_3V$	T = 950 K, E_b = 2.41 eV	E_b = 2.50 eV	E_b = 2.65 eV
2	$He_3V \rightarrow He + He_2V$	T = 1120 K, E_b = 2.88 eV	E_b = 2.52 eV	E_b = 2.73 eV
3	$He_2V \rightarrow He + HeV$	T = 1220 K, E_b = 3.11 eV	E_b = 2.89 eV	E_b = 3.14 eV
4	$HeV \rightarrow He + V$	T = 1560 K, E_b = 4.05 eV	E_b = 4.39 eV	E_b = 4.78 eV
5	$HeKrV_2 \rightarrow He + KrV_2$	T = 1480 K, E_b = 3.84 eV	E_b = 4.40 eV	
6	$He_2V_2 \rightarrow He + HeV_2$		E_b = 4.42 eV	E_b = 4.98 eV
7	$HeV_2 \rightarrow HeV + V$	T < 1560 K, $E_b <$ 4.05 eV		E_b = 0.27 eV

5.1.2 Modeling results

We have modeled each step of the experiment, although we did not explicitly include the Kr ions after they come to rest in the tungsten matrix. Figure 5.2 shows the predicted vacancy concentration profile as a function of depth below the surface following the 5 keV Kr^+ irradiation to a fluence of $8 \times 10^{15}/m^2$. Due to the fast diffusivity of tungsten self-interstitials and the proximity of the strong free surface sink, no significant density of self interstitials is predicted following the irradiation. The vacancies do not cluster because of the low vacancy diffusivity at room temperature and the weak binding energy of di-vacancies.

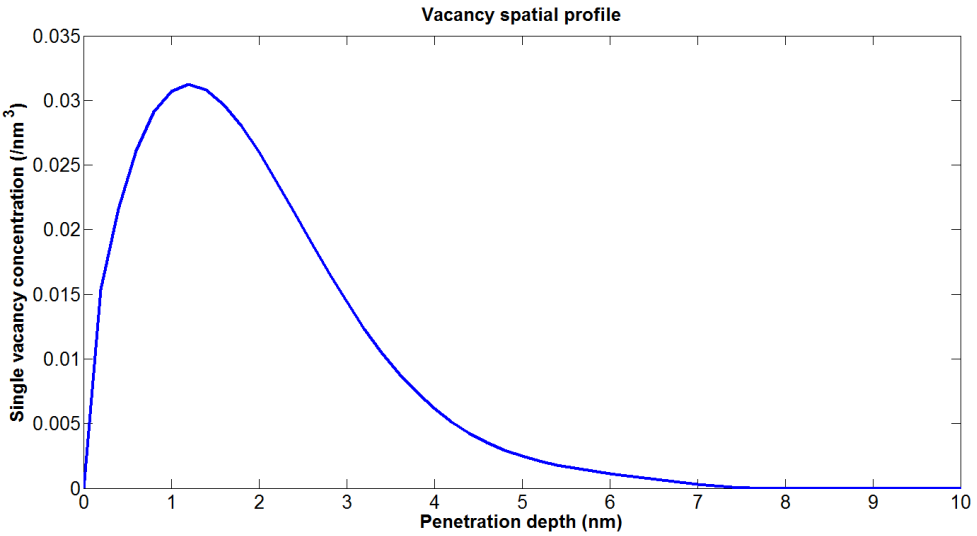


Figure 5.2: Spatial distribution of single vacancies after $8 \times 10^{11}/cm^2$ 5 keV Kr^+ irradiation.

In the next step, we simulate 250 eV helium ion irradiation. Since the incoming helium ion energy is too low to produce additional Frenkel pair defects, helium is implanted with a depth distribution shown in figure 2.2, and then diffuses and reacts with the pre-existing vacancies to form He_nV clusters. Helium can desorb from the system following diffusion to the free (entrant) surface. The distribution of He-vacancy clusters predicted to form following 250 eV He^+ implantation to a fluence of $8 \times 10^{16}/m^2$, is shown in figure 5.3.

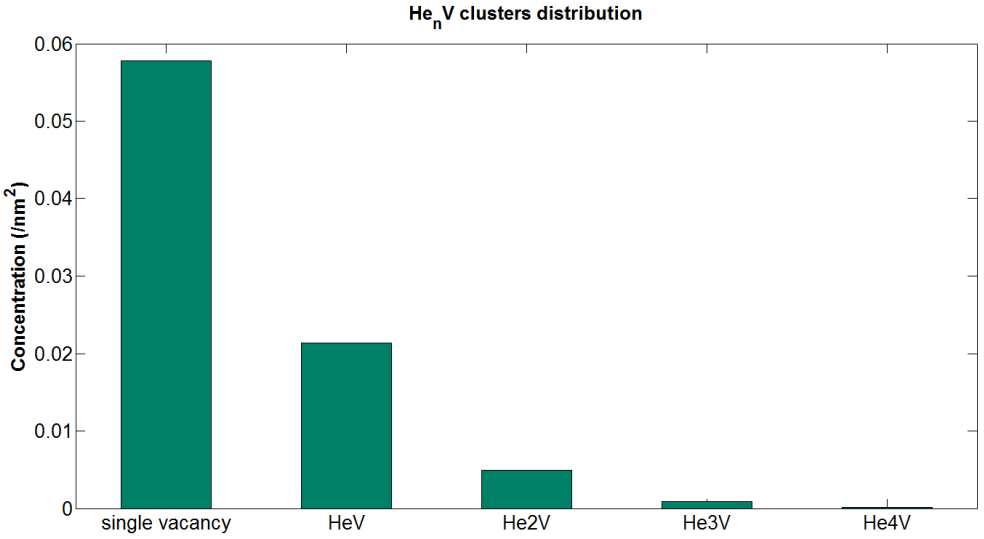


Figure 5.3: Distribution of He_nV clusters predicted following 250 eV He^+ implantation to a fluence of $8 \times 10^{16}/m^2$ in Kr ion irradiated tungsten at room temperature.

We then simulate the THDS experiment by increasing the temperature in the simulation and

computing the helium flux reaching the surface at $x = 0$. Figure 5.4 shows a comparison between the experimental THDS and the numerical simulations. We observe good agreement in both the position of the peaks and their relative magnitude. As the temperature increases, helium is released by dissociation of He_nV clusters corresponding to reactions **1**, **2**, **3** and **4** listed in table 3.5. The vacancies become mobile at around 700 K and start diffusing and reacting with existing He_nV clusters to form He_nV_2 clusters. These clusters dissociate by vacancy dissociation due to their high helium binding energy. In particular, the effect of reaction **6** ($He_2V_2 \rightarrow He + HeV_2$) can be observed in the spectrum. The main discrepancy between the predicted and measured THDS spectra results from not including Kr in the numerical simulation. Kornelsen et al. assumed that reaction **5** ($HeKrV_2 \rightarrow He + KrV_2$) contributes to the large release peak around 1500 K due to the binding of helium to Kr^+ ions. Since our model does not explicitly include Kr as a separate chemical species, there is a slight deviation in the shape of the predicted peak shape around 1500 K.

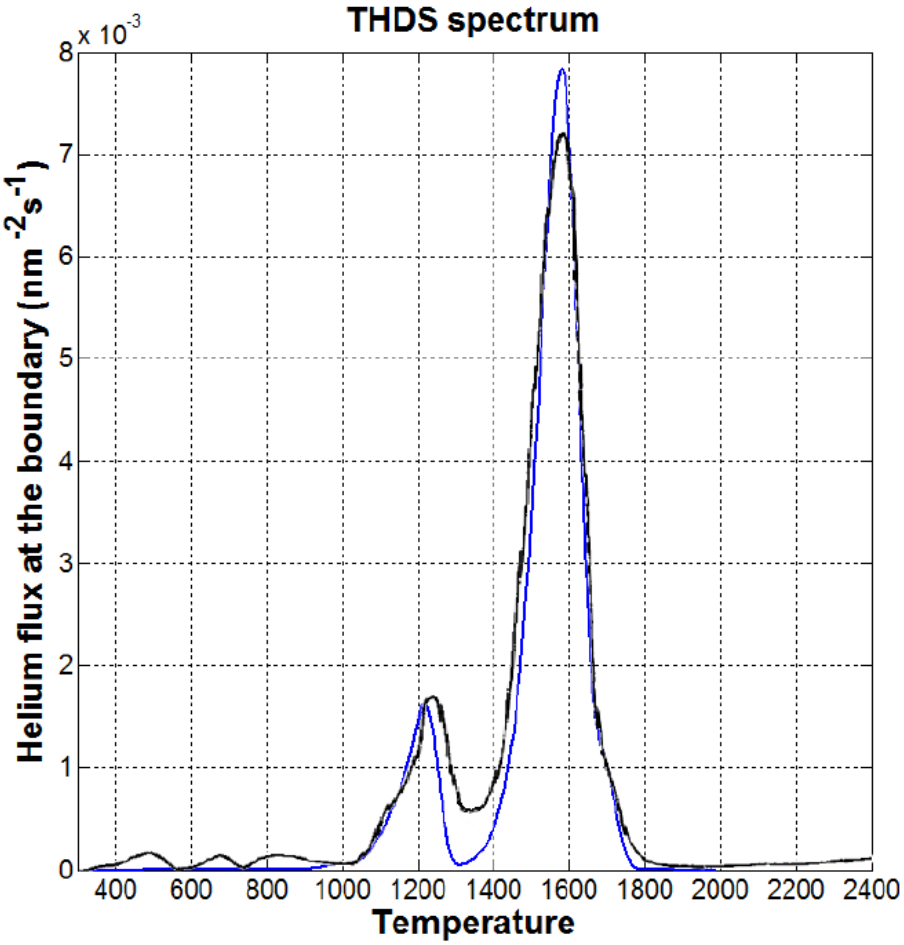


Figure 5.4: Model predictions (blue) and measured THDS (black) spectra following 250 eV He^+ implantation to a fluence of $8 \times 10^{16}/m^2$. The experimental results are reproduced from reference [14].

5.1.3 Effect of implanted He fluence on THDS behavior

Since a large number of thermodynamic and kinetic parameters influence the results, it is difficult to ensure self-consistency through only a single comparison of the model to experimental measurements. Thus, to provide further benchmarking, the model has also been compared to experimental results obtained under different irradiation conditions. Figure 5.5 shows comparisons between several THDS spectra. The experiments consist of sequential 5 keV Kr^+ irradiation to a fluence of $8 \times 10^{15}/m^2$ followed by 250 eV He^+ implantation to fluences from $4.4 \times 10^{15}/m^2$ to $1.8 \times 10^{17}/m^2$. The results again show good agreement between numerical and experimental results for every irradiation dose, where again the absence of reaction **5** is the main discrepancy. In particular, the model is able to simulate implantation of point defects and helium and subsequent

diffusion, reaction and dissociation at higher temperatures in a large range of irradiation conditions.

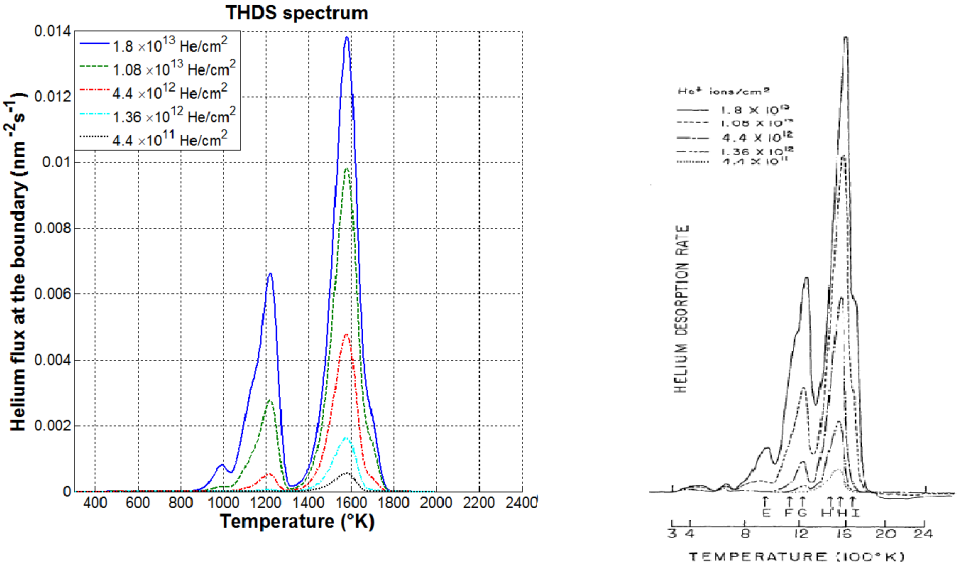


Figure 5.5: Model predictions (left) and measured THDS (right) for experiments performed using 5 keV Kr^+ irradiation to a fluence of $8 \times 10^{15}/m^2$ followed by 250 eV He^+ implantation to fluences from $4.4 \times 10^{15}/m^2$ to $1.8 \times 10^{17}/m^2$. The experimental results are reproduced from reference [14].

5.2 Comparison with Molecular Dynamics

5.2.1 MD Results

In order to develop an understanding of tungsten behavior under fusion relevant conditions, we will use the code with a much larger helium flux, which will be the subject of chapter 6. However, we can first gain insight of the evolution of the microstructure, and hence of the issues we will be facing, by comparing the results with molecular dynamics simulations. It should be noted that the helium fluxes faced in fusion reactors ($\sim 10^{22}$ He m^{-2}s^{-1}) are much smaller than the fluxes used in MD simulations ($\sim 10^{27}$ He m^{-2}s^{-1}), since MD simulations only simulate very small times and therefore much more helium is inserted per time unit in order to see the effect of helium irradiation. Nevertheless, this comparison is useful as it can identify the limits of the cluster dynamics code in extreme conditions.

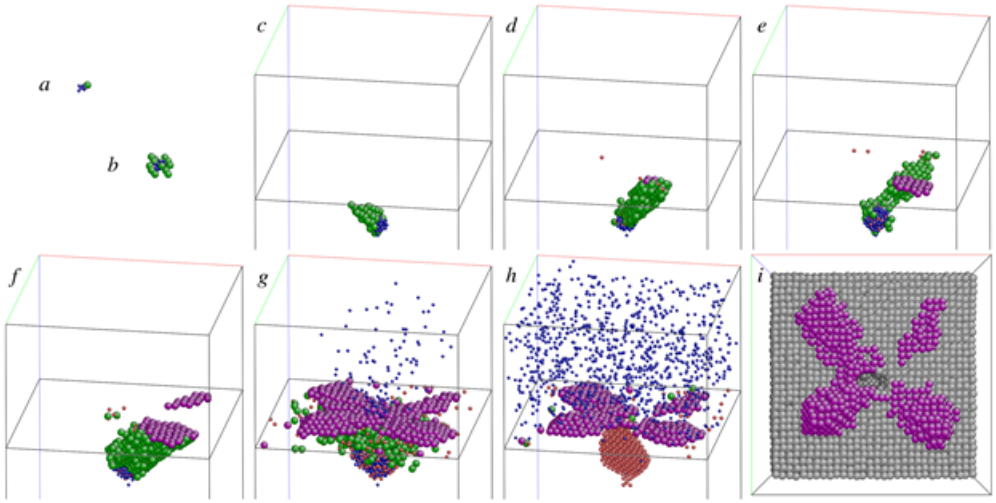


Figure 5.6: Evolution in time of the helium bubble, tungsten interstitials, and surface adatoms during growth of a helium bubble below a tungsten surface (ag). Red spheres are vacant sites, green are displaced tungsten atoms, purple are surface adatoms, blue spheres are helium, and gray spheres are tungsten atoms. (a) to (h) only show the helium, displaced tungsten atoms and vacancies, with the original surface represented by a rectangle. (i) is a top-down view of the final surface with all the atoms represented. Trap-mutation processes of single interstitial formation repeatedly occur as gas pressure increases, leading to the self-assembly of prismatic loops, which de-trap from the bubble and glide to the surface, forming multiple adatom islands. Ultimately, the bubble ruptures (g,h), leaving a heavily deformed surface (i) with multiple layers of tungsten adatom islands, a crater, and a hole. This figure is reproduced from reference [15].

One of the first limits observed for these extreme fluxes is illustrated in figure 5.6: large over-pressurized helium-vacancy clusters formed near the surface by successive trap mutation events are observed bursting at the surface in MD. These bubble bursting events significantly modify the surface morphology as well as the composition of the microstructure below the tungsten surface. Since these events are not taken into account in the cluster dynamics model, we can only simulate for the low times before bubble bursting events occur. Nevertheless, since the accumulation of helium atoms below the surface is the cause for subsequent surface morphology changes, we can aim to predict the conditions (fluence, temperature, concentration, helium content) which will lead to such bubble bursting events.

Another feature is the fact that for fluxes as high as the 10^{27} He $m^{-2}s^{-1}$ used in MD, helium interstitial atoms do not diffuse deep into the materials, as they almost instantaneously react with other atoms in the implantation layer close to the surface. Therefore, all the clusters formed are only a few lattice parameters below the surface, and results such as the helium retention as a function of time and the helium content distribution of gas bubbles formed are more meaningful than the depth dependent cluster distribution.

5.2.2 Modeling Results

Figure 5.7 shows the helium retention results as a function of time and temperature in MD and CD. Both models are in excellent agreement over the range of temperatures considered. These results indicate that the CD model predicts accurately the helium implantation, diffusion and reaction with other mobile helium species. However, as shown in figure 5.8, the agreement for the distribution of helium content among clusters is not good: The CD model predicts, unlike MD, a strongly temperature dependent helium distribution. The CD model also predicts more numerous but smaller clusters than what is observed in MD.

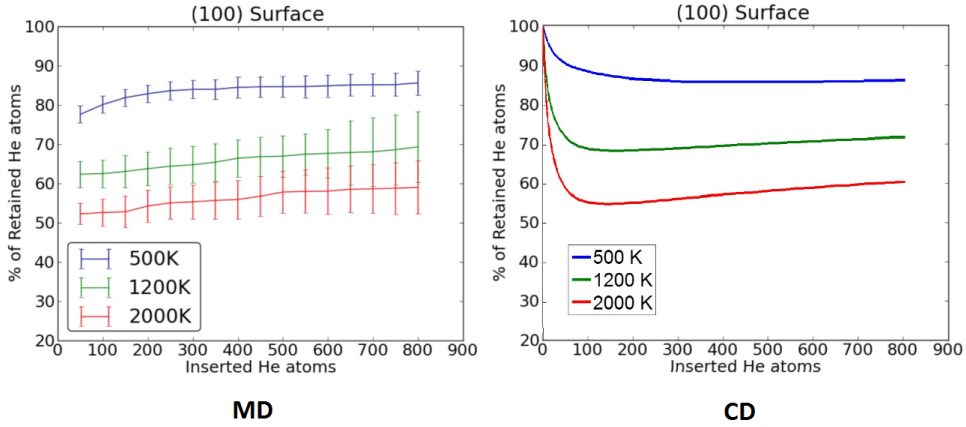


Figure 5.7: CD and MD comparison of helium retention for a flux of 2.4×10^{27} Hem^{-2}s^{-1} up to a fluence of 2×10^{19} He m^{-2}.

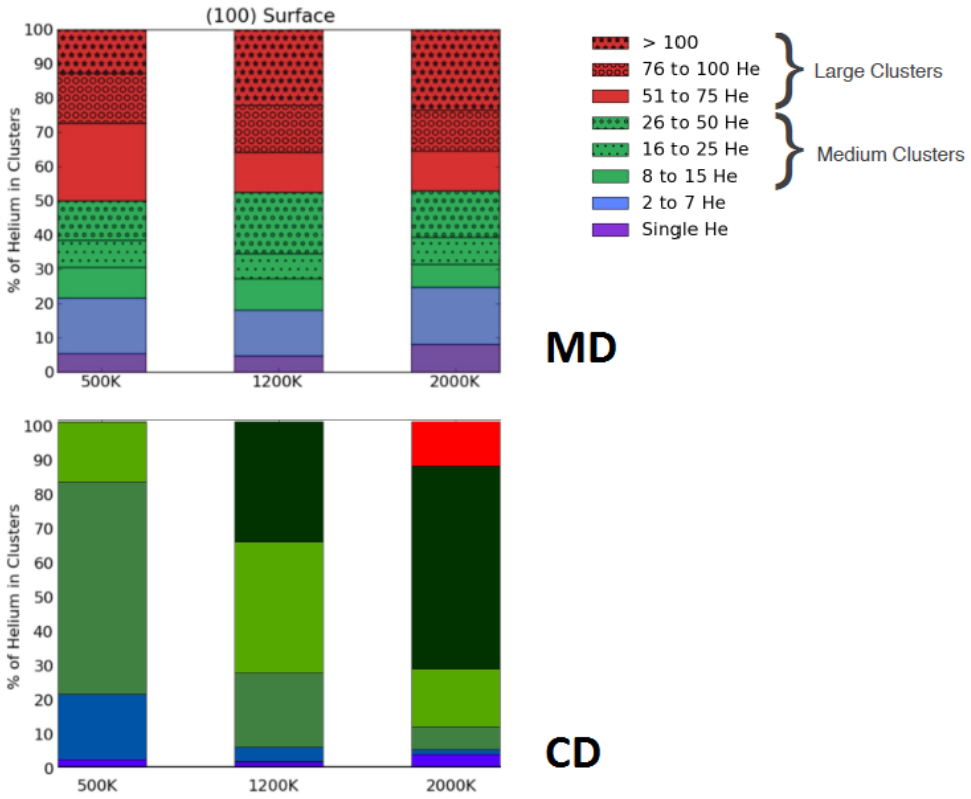


Figure 5.8: CD and MD comparison of helium content in clusters for a flux of 2.4×10^{27} He $m^{-2}s^{-1}$ up to a fluence of 2×10^{19} He m^{-2}, as a function of temperature.

One possible reason for this difference is that the CD model does not take into account spatial correlation. Hence, when the concentration of species becomes very large, as is the case for the extreme fluxes used in MD, the CD model can not reflect the direct interactions between clusters. One of these spatial effects observed in MD is bubble coalescence, when two gas bubbles close to each other merge to form a larger one. Figure 5.9 shows an example of such a coalescence event. These events can partially explain the smaller number of larger clusters observed in MD. As seen in chapter 2, a measure of the dilute limit approximation is given by the volume fraction $V_f = \sum_{\text{all species i}} \frac{4}{3}\pi r_i^3 C_i$. At all times, we need $V_f \ll 1$ for the dilute limit approximation to be valid. Figure 5.10 shows that using MD fluxes, we already reach volume fractions of several percent at very low fluences, and hence we are approaching the limit of the validity of the CD model. Another possible explanation for that discrepancy is that as seen in chapter 3, trap mutation in MD occurs at a higher rate than what is predicted by CD theory. Therefore, there is a bias to form smaller clusters using the CD model when trap mutation is the main growth mechanism.

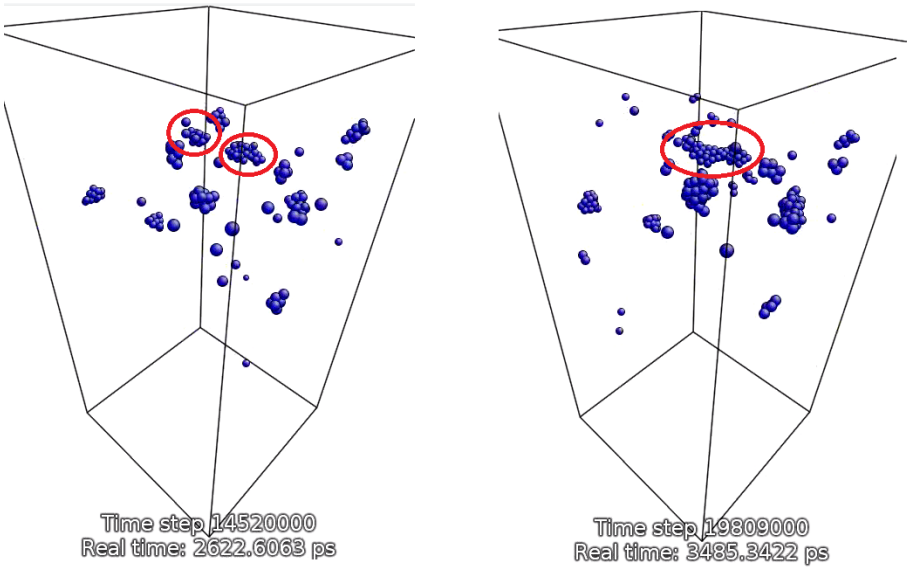


Figure 5.9: Example of a coalescence event between two bubbles (MD simulation performed by Faiza Sefta).

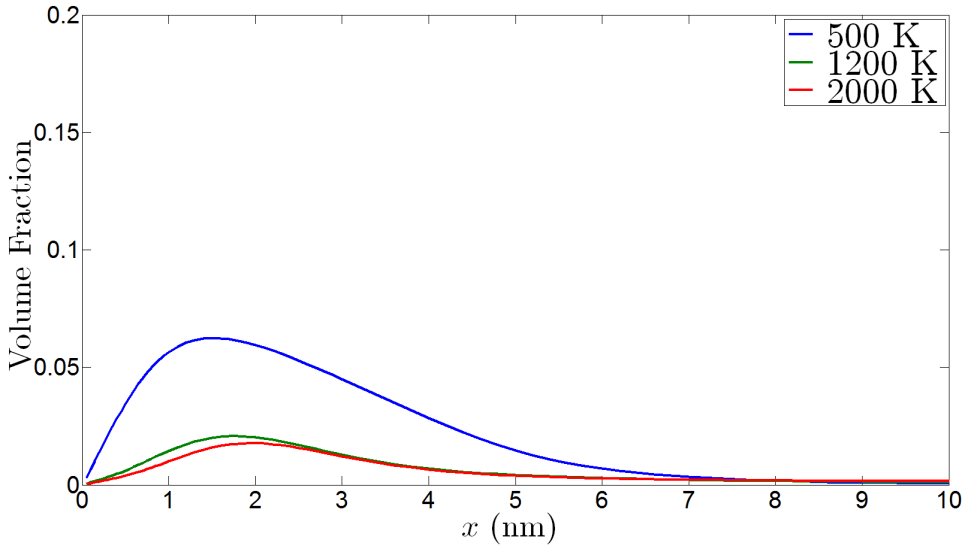


Figure 5.10: Volume Fraction of helium clusters for a flux of 2.4×10^{27} He m^{-2}s^{-1} up to a fluence of 2×10^{19} He m^{-2}, as a function of temperature.

5.2.3 Conclusion

The physical processes of diffusion, reaction and dissociation have been modeled with thermodynamic binding energies and kinetic diffusion coefficients obtained from a combination of experiments and computational models. The good agreement of the desorption peaks between simulations and experiments indicate that the parameters are accurate.
The comparison with MD results is an extreme case scenario useful to identify the processes potentially limiting the use of the Cluster Dynamics model under fusion relevant conditions. In the next chapter, we should therefore care about two issues: first, we should measure the size of the bubbles close to the surface to be aware of possible bursting events affecting the results. Second, we should measure the volume fraction at all times during the simulation to ensure the validity of the dilute limit approximation and of the CD model. Fortunately, we will see that these issues are occurring at much longer irradiation times so we can obtain useful results using the CD model under fusion relevant conditions. This also means that MD simulations, although useful to determine the possible physical processes involved, can not be extrapolated for longer times since the irradiation conditions, with a flux orders of magnitudes higher than in fusion reactors, are the cause of a different growth regime controlled by the very high concentrations of helium and the spatial correlation between these helium defects.

Chapter 6

Cluster Dynamics Results under Fusion Relevant Conditions

In this chapter, the results of the cluster dynamics code applied to helium implantation conditions relevant to divertor operations in fusion reactors are presented (T $\sim$ 1000 K, helium flux $\sim 10^{22} m^{-2} s^{-1}$). First, the trap mutation phenomenon is described in more detail since it is largely responsible for the growth mechanism of helium-vacancy clusters. Second, an extension of the CD model is presented to be able to deal with very large gas bubbles by considering a continuous phase space of species. Finally, results of the cluster dynamics model for two different geometries and several implantation conditions are discussed.

6.1 Trap mutation phenomenon

At high fluxes and temperatures, the following growth mechanism is proposed based on observations from MD simulations [15, 84]: injected helium interstitials diffuse in the tungsten matrix and react with each other, thus forming small helium interstitial clusters. These small interstitial clusters grow by self-trapping of additional helium interstitials and helium interstitial clusters, until they reach a critical, temperature dependent size at which a trap mutation phenomenon occurs. The growing, over-pressurized helium interstitial cluster ejects a surrounding tungsten atom to form a helium-vacancy cluster, in a process we define as trap mutation:

$$He_n \rightarrow He_n V + I \tag{6.1}$$

The tungsten self-interstitial atom formed is free to diffuse towards the free surface or react with other species, while the immobile $He_n V$ cluster formed can keep growing by absorption of more mobile helium atoms. When it reaches a sufficient size, trap mutation can occur again, and the

growth mechanism can be described as:

$$\begin{aligned} He_{n_1} &\rightarrow He_{n_1}V + I \\ He_{n_1}V + n_2He &\rightarrow He_{n_1+n_2}V \rightarrow He_{n_1+n_2}V_2 + I \\ &\vdots \\ He_{n_m}V_m + n_{m+1}He &\rightarrow He_{n_m+n_{m+1}}V_m \rightarrow He_{n_m+n_{m+1}}V_{m+1} + I \end{aligned} \tag{6.2}$$

Trap mutation events ultimately determine which species are considered in the model, since only a limited number of helium can be packed together in a given sized Helium-vacancy cluster. To determine this limit, we are using the results of molecular statics simulations by Juslin et. al [85]. At 0 K, the results of minimizing the energy for a given helium-vacancy cluster can lead to a static trap mutation event. When this happens, we consider that species to be the limiting number of helium for that amount of vacancy. Any reaction with other mobile helium species will lead to a trap mutation event. Figure 6.1 shows the limiting number of helium per vacancy at which trap mutation occurs, as computed using molecular statics simulations. We see that past a certain size ($\sim$ 10 vacancies), the limiting number of helium per vacancy at which trap mutation occurs stabilizes to a value of approximately 4. Therefore, under fusion relevant plasma surface interaction conditions, very large helium-vacancy clusters can quickly form in the tungsten matrix even in the absence of pre-existing traps for the mobile helium.

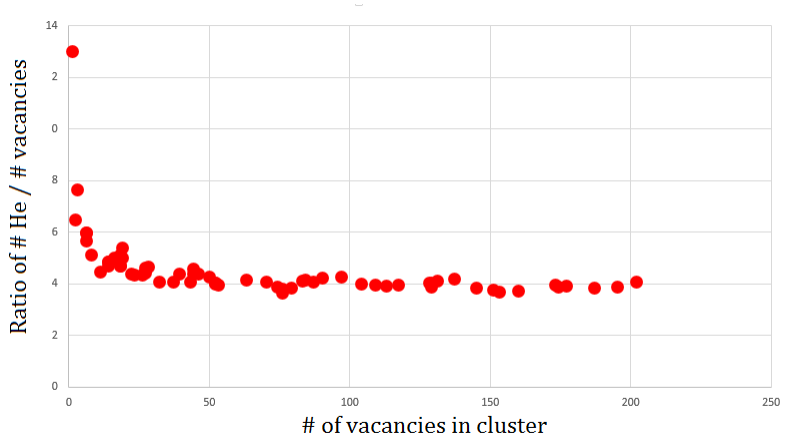


Figure 6.1: Limiting number of helium per vacancy at which trap mutation occurs at 0 K.

6.2 Extension of the model to large clusters

Since the number of helium and vacancies per species can quickly grow to thousands, it becomes very challenging to use the model equations for each different species: first, we need to determine the binding energies for helium dissociation, vacancy dissociation and trap mutation for every single species, and second we need to solve the model equations for a very large number of species

($N > 1000000$).

The first problem can be solved by extrapolating the binding energies of large helium vacancy clusters based on the binding energies computed using molecular dynamics. The second problem can be alleviated in a similar way: since very large over-pressurized helium-vacancy clusters have a similar behavior, we are more interested in general quantities such as total cluster concentration, average size and number of helium or volume fraction occupied by helium-vacancy clusters rather than in the detailed distribution of the concentration of each helium-vacancy cluster.

To explain this in detail, let us order the species considered from 1 to N. We have computed the binding energies using MD for each species up to size N, and we are able to solve the model equations for each of these cluster species. The largest species explicitly considered corresponds to a helium-vacancy cluster with 100 vacancies and 500 helium. The cluster dynamics equations can be written

$$\begin{aligned}
\frac{\partial C_1}{\partial t} &= D_1 \frac{\partial^2 C_1}{\partial x^2} + S - 2k^+_{1,1}C_1^2 - \sum_{i=2}^{N} k^+_{1,i}C_1C_i - \sum_{i=N+1}^{\infty} k^+_{1,i}C_1C_i \\
\frac{\partial C_2}{\partial t} &= D_2 \frac{\partial^2 C_2}{\partial x^2} - k^+_{1,2}C_1C_2 + k^+_{1,1}C_1^2 \\
&\vdots \\
\frac{\partial C_N}{\partial t} &= -k^+_{1,N}C_1C_N + k^+_{1,N-1}C_1C_{N-1} \\
\frac{\partial C_{N+1}}{\partial t} &= -k^+_{1,N+1}C_1C_{N+1} + k^+_{1,N}C_1C_N \\
&\vdots
\end{aligned} \tag{6.3}$$

Now let us define the total bubble concentration and average bubble helium content, radius and capture constant :

$$C_b = \sum_{i=N+1}^{\infty} C_i \tag{6.4}$$

$$< i_b >= \frac{\sum_{i=N+1}^{\infty} iC_i}{C_b} \tag{6.5}$$

$$< r_b >= \frac{\sum_{i=N+1}^{\infty} r_iC_i}{C_b} \approx f(< i_b >) \tag{6.6}$$

$$< k^+_b >= \frac{\sum_{i=N+1}^{\infty} k^+_{1,i}C_i}{C_b} = 4\pi D_1(r_1 + < r_b >) \tag{6.7}$$

$$\tag{6.8}$$

The evolution equations become

$$\frac{\partial C_1}{\partial t} = D_1 \frac{\partial^2 C_1}{\partial x^2} + S - 2k_{1,1}^+ C_1^2 - \sum_{i=2}^{N} k_{1,i}^+ C_1 C_i - < k_b^+ > C_1 C_b \tag{6.9}$$

$$\frac{\partial C_2}{\partial t} = D_2 \frac{\partial^2 C_2}{\partial x^2} - k_{1,2}^+ C_1 C_2 + k_{1,1}^+ C_1^2 \tag{6.10}$$

$$\vdots \tag{6.11}$$

$$\frac{\partial C_n}{\partial t} = -k_{1,N}^+ C_1 C_n + k_{1,N-1}^+ C_1 C_{N-1} \tag{6.12}$$

$$\frac{\partial C_b}{\partial t} = k_{1,N}^+ C_1 C_N \tag{6.13}$$

$$\frac{\partial \left(< i_b > C_b\right)}{\partial t} = (N+1) k_{1,N}^+ C_1 C_N + < k_b^+ > C_1 C_b \tag{6.14}$$

This approach to extending the model description to a larger He-vacancy cluster phase space consists of two main approximations:

- First, we assume

$$< r_b >= r(He_{<i_b>} V_{<i_b>/4}) = r_{He_0 V_1} + \left(\frac{3}{4\pi}\frac{a_0^3}{2}\frac{< i_b >}{4}\right)^{1/3} - \left(\frac{3}{4\pi}\frac{a_0^3}{2}\right)^{1/3} \tag{6.15}$$

  That is, we assume that the average radius of the bubbles is the radius of a helium-vacancy cluster with the average helium content $< i_b >$. Since figure 6.1 shows we have approximately one trap mutation event, and thus one additional vacancy, for every 4 helium absorbed for large helium-vacancy clusters, that radius is then computed using the classical radius formula for a vacancy cluster containing $< i_b > /4$ vacancies. Due to this approximation, the value of $< k_b^+ >$ is not exact anymore and so the conservation of helium atoms is altered. This alteration depends on the actual distribution of large helium vacancy clusters in the phase space: the more the distribution is skewed towards smaller and larger clusters than the average, the more questionable becomes this approximation. However, numerical experiments comparing the detailed model with an explicit account of large helium vacancy clusters and the extended model show that the actual distribution of helium vacancy clusters under constant irradiation conditions has a narrow Gaussian shape centered on the average value $< C_b >$. Therefore, we expect relatively little impact of the extended model on the conservation of helium atoms under these conditions.

- The second approximation is that we neglect dissociation of large helium-vacancy clusters ($\geq He_{250}V_{50}$ in this paper). The binding energy for trap mutation events is indeed lower than the binding energy for helium or vacancy dissociation events for large over-pressurized helium-vacancy clusters. Therefore the frequency of helium and vacancy dissociation events is negligible compared to the frequency of trap mutation events, regardless of the temperature range.

6.3 Results

6.3.1 Tendril Geometry

Several experimental studies show a severe change in the surface morphology of tungsten under fusion relevant conditions of temperature $\geq$ 1000 K, helium flux $\geq$ $10^{22}m^{-2}s^{-1}$, fluence $\geq$ $10^{25}m^{-2}$ and incident helium energy $\leq$ 100 eV) [8, 20]. At temperature above 1000 K, a nanometre-sized fibre structure, or tungsten "nanofuzz", is formed consisting of tungsten tendrils filled with nanometer sized gas bubbles separated by holes in the tungsten surface. Figure 6.2 shows an example of this nanofuzz structure, as reproduced from reference [8].

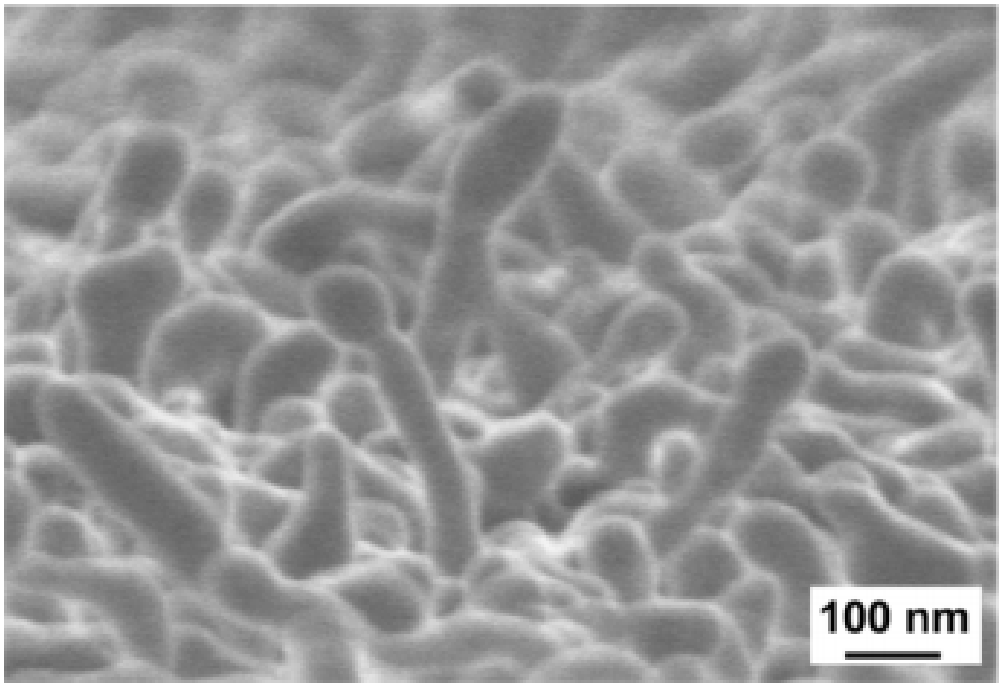


Figure 6.2: SEM micrograph showing a tungsten surface after 50 eV helium ion irradiation up to a fluence of $1.1 \times 10^{25}m^{-2}$ at $1400K$, as reproduced from Ref [8].

We have applied our continuum reaction-diffusion model to simulate helium irradiation in a tendril under different implantation conditions and study the impact of important parameters such as the irradiation temperature or flux. The tendril geometry is assumed to have a simple rectangular shape, with a length much greater than its width. Assuming axial symmetry, our 1-dimensional code thus models helium implantation into the direction perpendicular to a side of the tendril.

Standard case

We present results for a standard case with the following parameters: uniform irradiation on a tendril side with flux = 10^{22} $m^{-2}s^{-1}$, fluence up to 5×10^{25} $m^{-2}s^{-1}$, temperature = 1000 K,

tendril width $\Delta = 30\ nm$ and length $L = 100\ \mu m$. In such a tendril, the volume, V, is 9×10^7 nm^3 and the presence of a single species corresponds to a concentration of $C \sim 10^{-8}\ nm^{-3}$. Figure 6.3 shows that mobile species (He_1 to He_6) quickly reach a steady-state value resulting from a balance between diffusion towards the free surface at $x = 0$ and $x = \Delta$, compared with reactions to form larger clusters. As these clusters react to form larger helium-vacancy clusters through the trap mutation process discussed in section 6.1, we see an increase in concentration of relatively small ($\leq He_{250}V_{50}$) helium-vacancy clusters. These clusters serve as the nuclei that grow into larger gas bubbles. The continuous flux of incident helium atoms causes both an increase in the concentration of gas bubbles as well as the growth of these bubbles. At the end of the simulation (at a fluence of $5 \times 10^{25} m^{-2}$), the concentration of gas bubbles remains relatively small ($C_{bubbles} \approx 10^{-8} nm^{-3}$) and the concentration of small mobile helium clusters is negligible, which means that essentially only single helium atoms are present in the tendril.

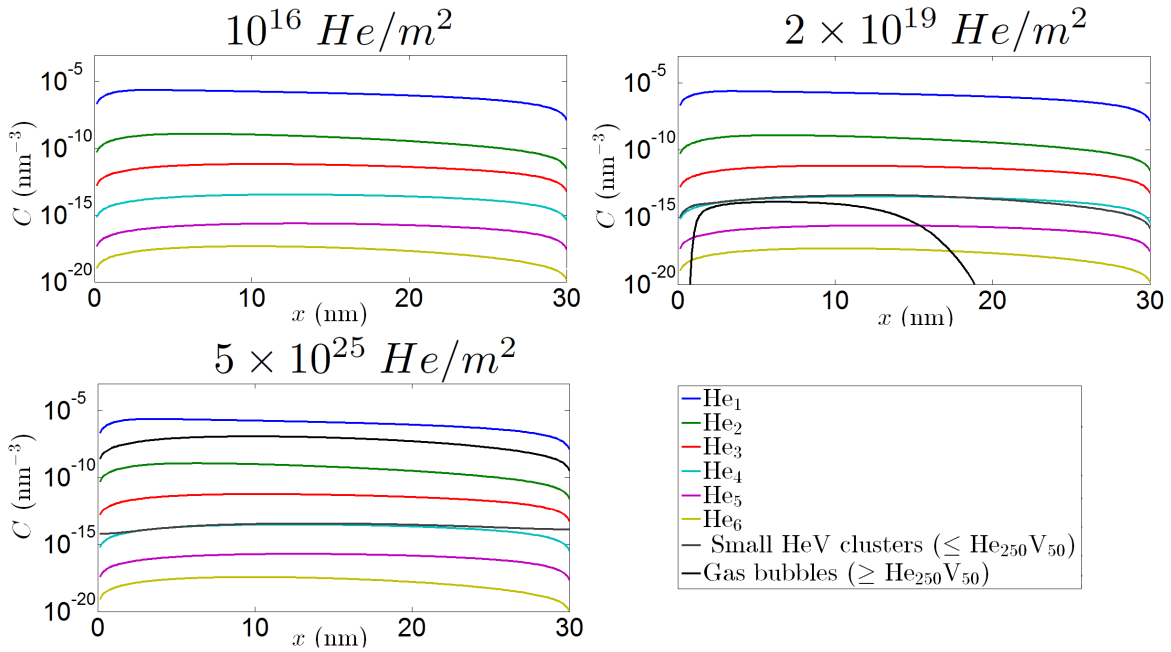


Figure 6.3: Concentration of mobile helium clusters and immobile helium-vacancy clusters in a tendril after $10^{22}\ m^{-2}s^{-1}$ 100 eV helium irradiation at 1000 K up to a fluence of $5 \times 10^{25} m^{-2}$.

Influence of temperature and helium flux

Figures 6.4 and 6.5 show the effect of varying the temperature. Figures 6.6 and 6.7 show the effect of varying the helium flux. We observe that decreasing temperature has the same effect as increasing the incoming helium flux; namely, in the first case, the mobility of the helium clusters decreases so that their concentration increases, and cluster growth is enhanced; while in the latter case, the concentration of single helium is increased which in turn increases the reaction rate with mobile helium clusters, again resulting in enhanced growth of large helium-vacancy clusters

through trap mutation. It is interesting to note that at high temperatures (T $\geq$ $1000K$) or low fluxes ($\phi \leq 10^{22} m^{-2}s^{-1}$), no significant concentration of helium-vacancy clusters form in the tendril, while at low temperatures (T $\leq 500K$) or high fluxes ($\phi \geq 10^{23} m^{-2}s^{-1}$), large gas bubbles are predicted to form at relatively low fluences. In the latter case, these gas bubbles eventually cause helium depletion in the tendril as they absorb the majority of the incoming helium flux. Since experiments show a high concentration of nanometer-sized bubbles in the tendrils which are formed at temperatures above 1000 Kelvins [22], our results appear to indicate that defects are formed in the material before the tendrils are formed.

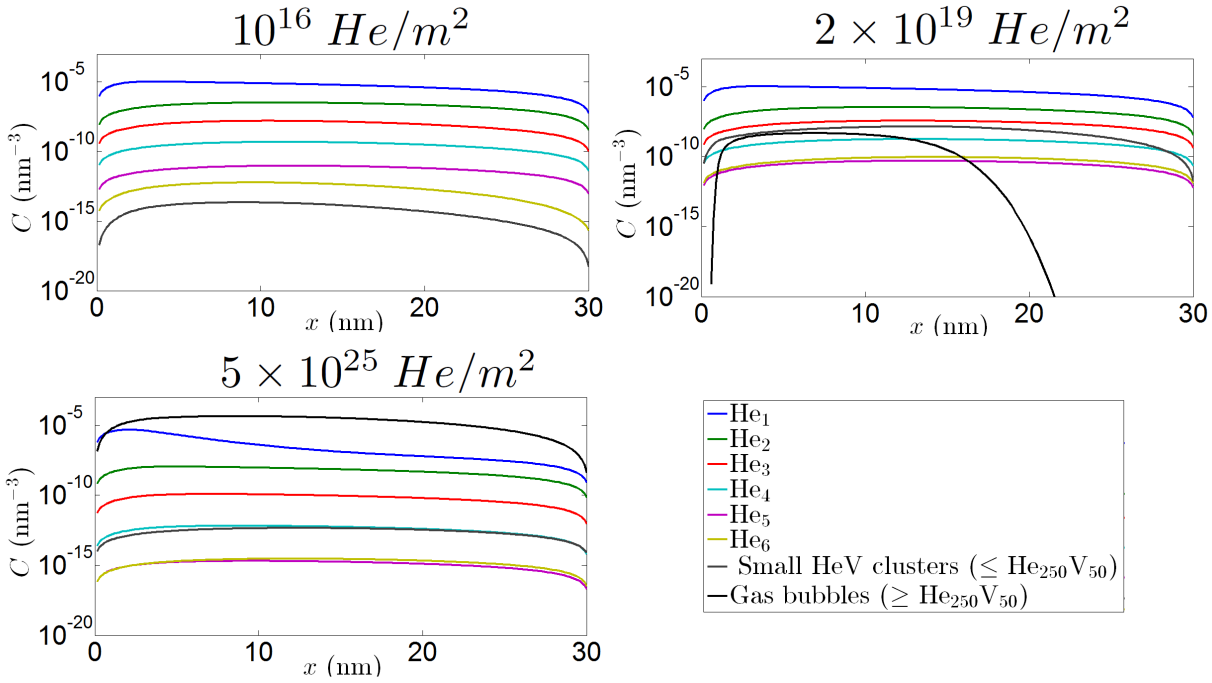


Figure 6.4: Concentration of mobile helium clusters and immobile helium-vacancy clusters in a tendril after 10^{22} $m^{-2}s^{-1}$ 100 eV helium irradiation at 500 K up to a fluence of $5 \times 10^{25} m^{-2}$.

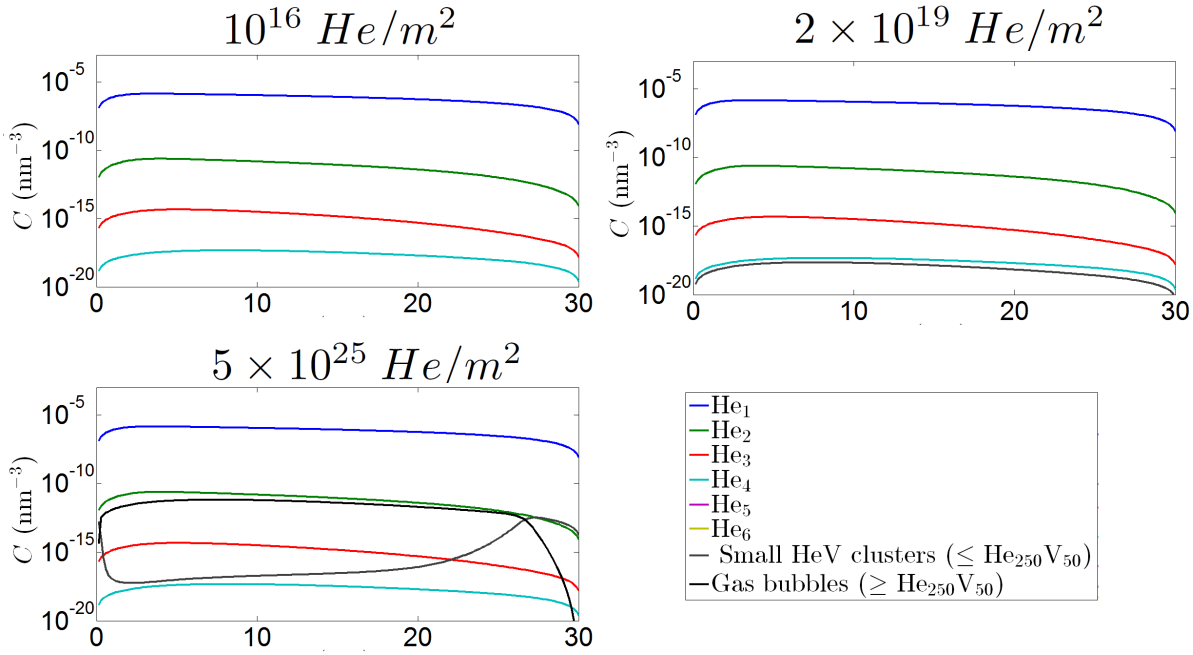


Figure 6.5: Concentration of mobile helium clusters and immobile helium-vacancy clusters in a tendril after 10^{22} $m^{-2}s^{-1}$ 100 eV helium irradiation at 1500 K up to a fluence of $5 \times 10^{25} m^{-2}$.

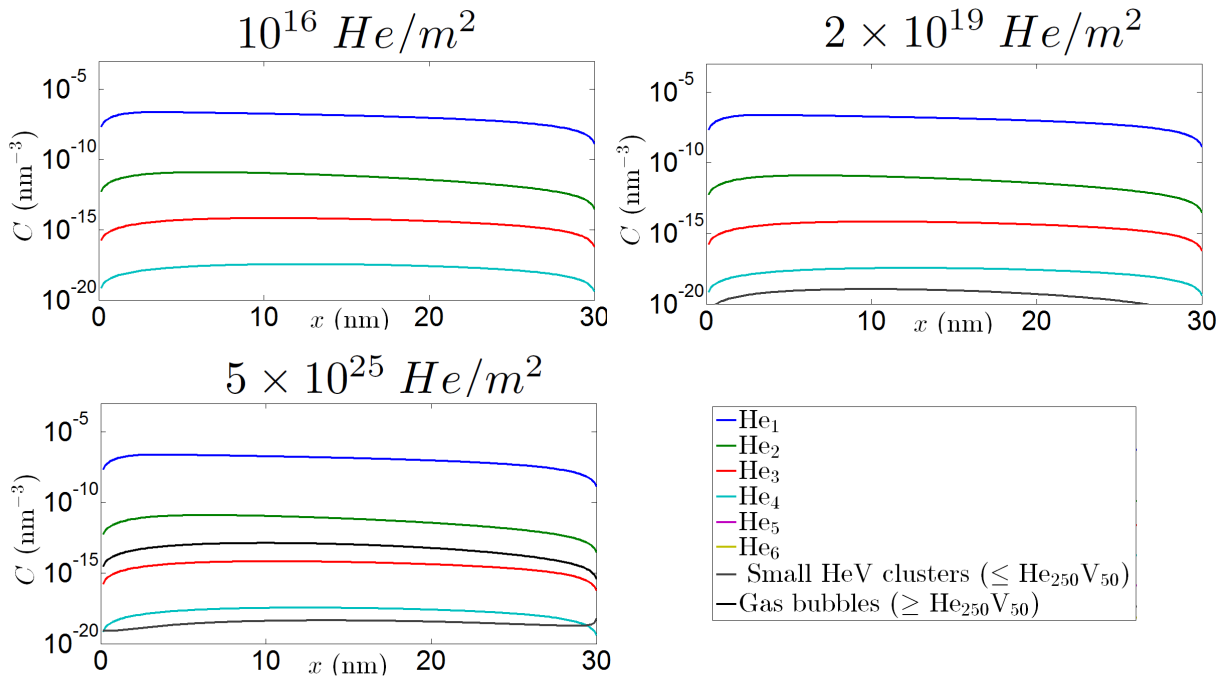


Figure 6.6: Concentration of mobile helium clusters and immobile helium-vacancy clusters in a tendril after 10^{21} $m^{-2}s^{-1}$ 100 eV helium irradiation at 1000 K up to a fluence of $5 \times 10^{25} m^{-2}$.

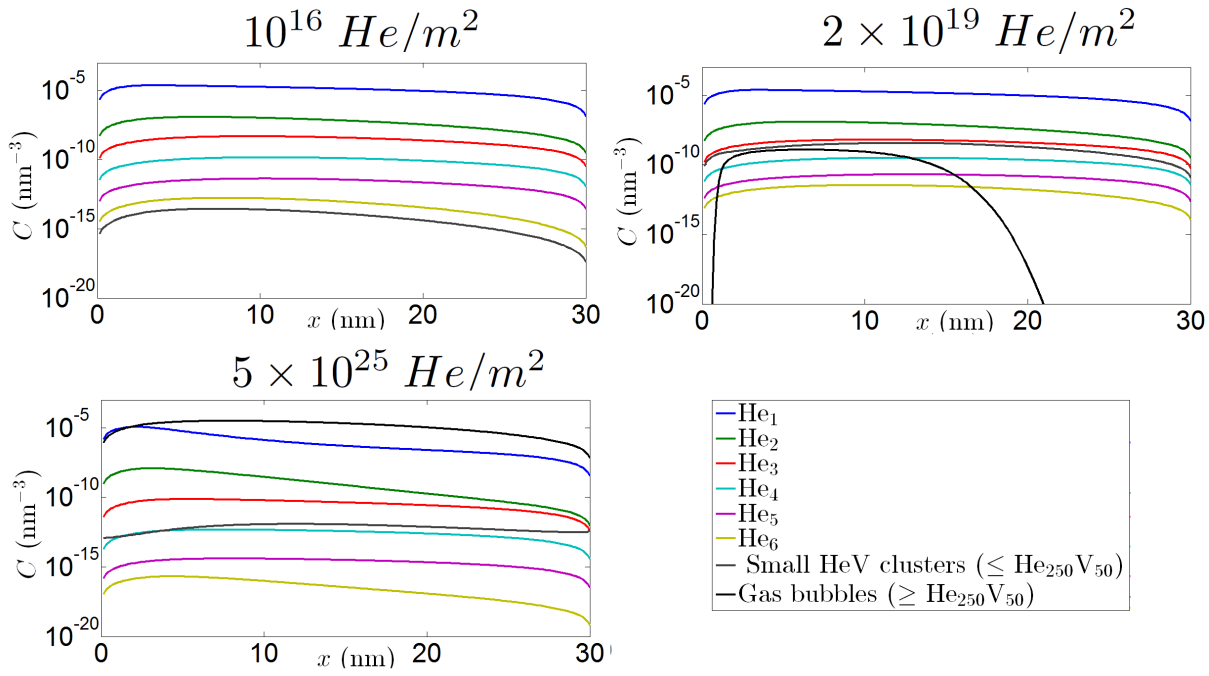


Figure 6.7: Concentration of mobile helium clusters and immobile helium-vacancy clusters in a tendril after $10^{23}\ m^{-2}s^{-1}$ 100 eV helium irradiation at 1000 K up to a fluence of $5 \times 10^{25} m^{-2}$.

Comparison with an analytical model

We can compare these results with an analytical Helium cluster/bubbles dynamics model developed by Krasheninnikov et al. [16]. The analytical model assumption of constant uniform concentration of single mobile helium atoms and steady-state concentrations of mobile helium atom clusters in the tendril geometry is justified by our model results. The values of these steady state concentrations, as shown in figure 6.8, are in excellent agreement with the values given by our model in figure 6.3. Figure 6.9 also compares the time required to produce a single immobile cluster as a function of the helium flux in both models at 1000 K. Again, an excellent agreement is found between the analytical model of Krashenninikov and our simulation results. This tends to confirm that large gas bubbles are not predicted to form in existing tendril geometries for temperatures above 1000 K and fluxes below $10^{22}\ m^{-2}s^{-1}$.

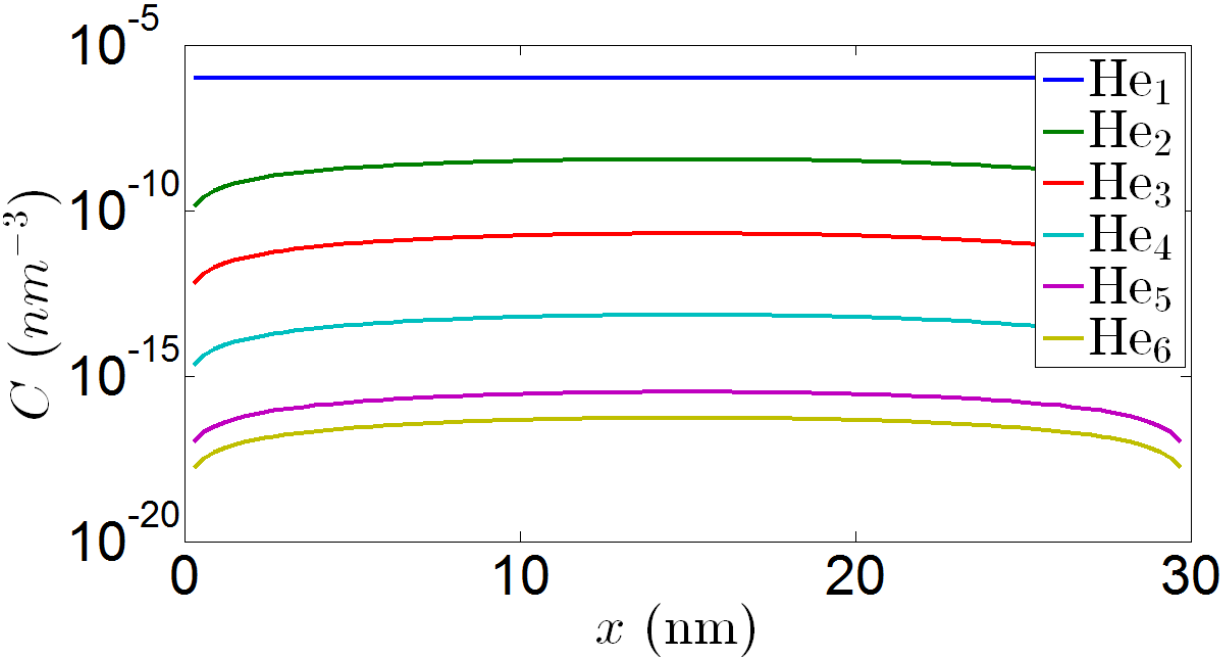


Figure 6.8: Steady-state concentrations of mobile helium clusters in a tendril for $10^{22}m^{-2}s^{-1}$ 100 eV helium implantation at 1000 K, as reproduced from reference [16].

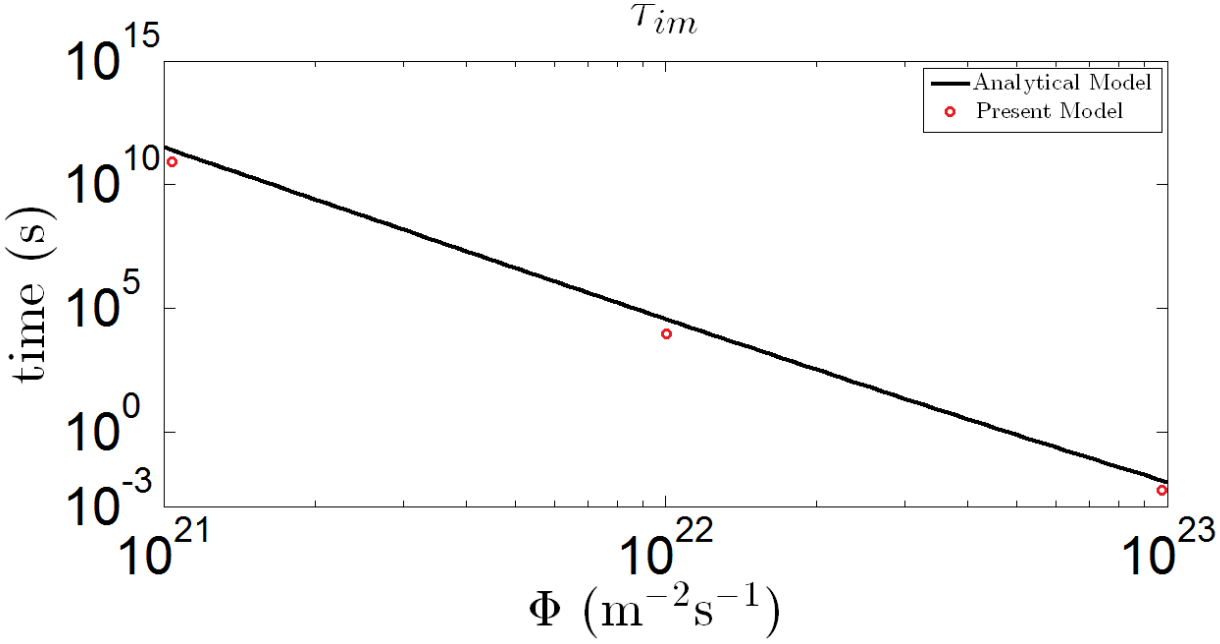


Figure 6.9: Time required to produce a single immobile helium cluster in the tendril as a function of helium implantation flux at 1000 K for both models.

Model limitations

The cluster dynamics model indicates that helium-vacancy defects are formed deeper in the material before surface morphology changes occur. However, we would like to discuss the current model limitations when applied to the tendril geometry: First, since our model is one dimensional and assumes symmetry in the other directions, the effect of free surfaces in a tendril geometry is underestimated. This would indicate an even smaller growth rate of large gas bubbles inside the tendrils. Second, we can not accurately model the tendril evolution once large gas bubbles are formed: molecular dynamics simulations indicate that large over-pressurized gas bubbles with a radius of several nanometers can burst when close to the surface [15], as is the case for the 30 nanometer wide tendril, and induce significant morphology changes. Third, we do not take into account pre-existing impurities in the tungsten which could act as nucleation sites for helium-vacancy clusters before self-trapping occurs, and hence influence both bubble nucleation and growth. These shortcomings are being addressed by a new 3-dimensional cluster dynamics code being developed as part of a SciDAC project on plasma surface interactions [86], which should be able to provide much better predictions for nanofuzz or tendril structures. This code is thus more adapted to predict the results of initial helium irradiation in the tungsten material before significant morphology changes appear, as will be discussed in the next section.

6.3.2 Half-Slab Geometry

In this section, we provide model results for the case of helium implantation into a perfect tungsten surface. The geometry is an infinite half-slab, and the species are allowed to diffuse deep into the material, with a free surface at $x = 0$.

Standard case

Figure 6.10 shows results for an implantation flux of $\phi = 10^{22}\ m^{-2}s^{-1}$ and a temperature of 1000 Kelvin. We observe that helium interstitial atoms diffuse deep into the tungsten material (several micrometers) within relatively short times. Past the implantation layer of a few nanometers, the helium interstitial concentration is almost constant as a result of very fast helium diffusion in tungsten. As the fluence increases, self-trapping of helium interstitial atoms create mobile helium clusters of increasing size. These clusters continue to grow by trapping more helium atoms and become larger, immobile helium vacancy clusters (He_xV_y) through the trap mutation process. The peak concentration of these helium bubbles is initially located far below the surface ($\sim$ 200 nm). As more helium interstitials are implanted and continue to interact and self-trap, as well as diffuse to and react with the existing He_xV_y clusters, the helium bubble concentration increases to reach a peak of 1.5×10^{-6} nm^{-3} at an implanted fluence of $5 \times 10^{25} m^{-2}$.

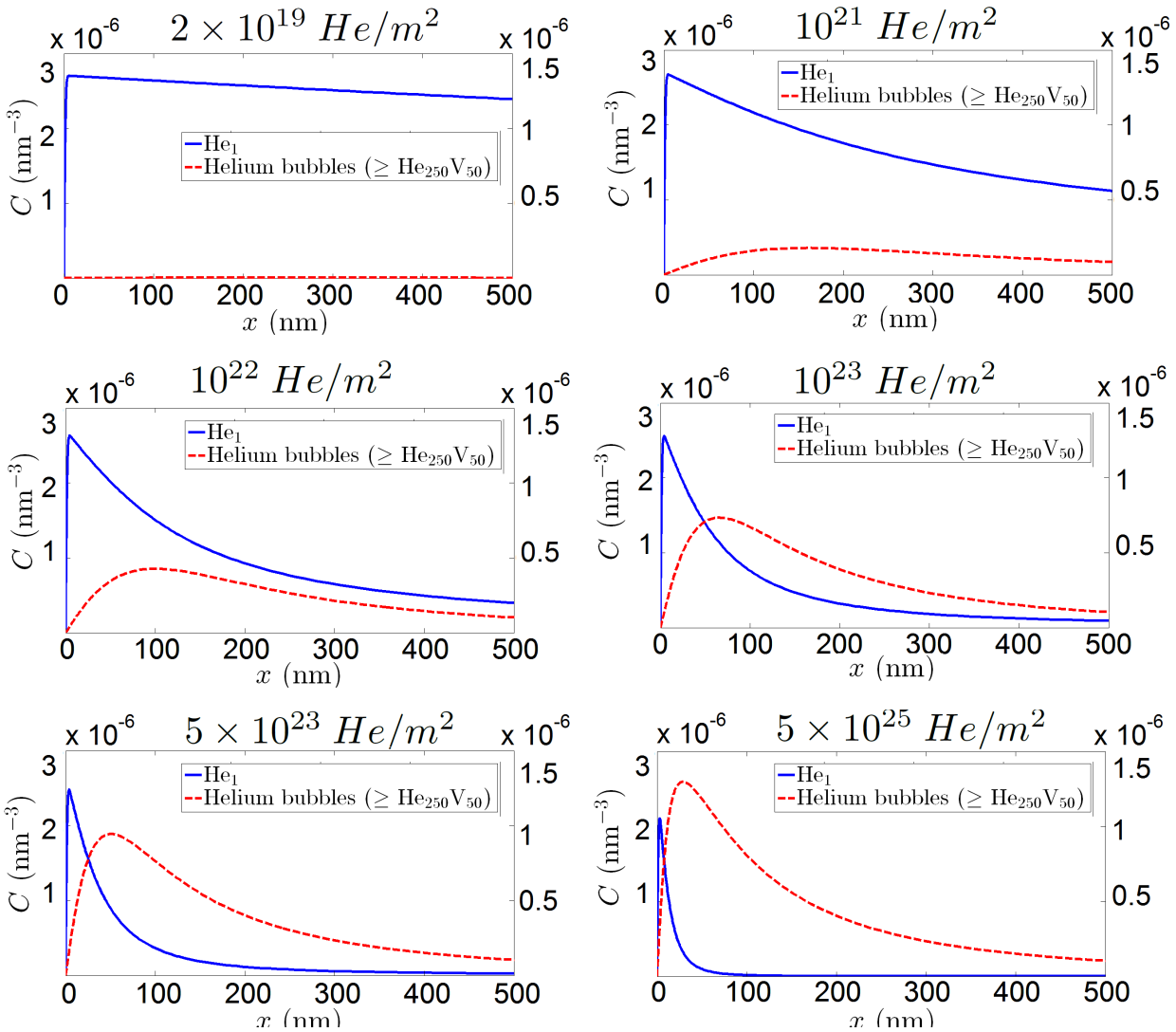


Figure 6.10: Concentration of helium interstitial atoms and helium bubbles after 10^{22} $m^{-2}s^{-1}$ 100 eV helium irradiation at 1000K up to a fluence of $5 \times 10^{25} m^{-2}$.

We also observe that these helium bubbles act as a "plug" preventing the deeper diffusion of helium interstitials into the tungsten material: this plug of large helium bubbles slowly moves towards the surface as incoming helium interstitials react at the front of the plug, while we observe a depletion of the helium content in the material beyond the front of the plug. At the end of the simulation, the plug is located 50 nanometers below the surface, while it was initially formed several hundred nanometers below.

At the largest implanted fluence, the over-pressurized gas bubbles will eventually be close enough to the surface and reach a size which will produce bubble bursting and hence cause significant surface morphology changes, as observed in MD simulations [15]. However, this model does not yet

include such bubble bursting events. Moreover, figure 6.11 shows another concern for the cluster dynamics model: even before bubble bursting and the associated morphology changes at the surface become a concern, the volume fraction occupied by helium species in the tungsten material becomes very large. Hence, we can expect that the dilute limit approximation which ensures the validity of the cluster dynamics model breaks down due to the strong local interactions between species. In this regime, phenomena such as bubble coalescence are expected to become dominant. For a flux of $\phi = 10^{22}\ m^{-2}s^{-1}$ and a temperature of 1000 Kelvin, the dilute limit approximation breaks down at a fluence of approximately $5 \times 10^{23} m^{-2}$.

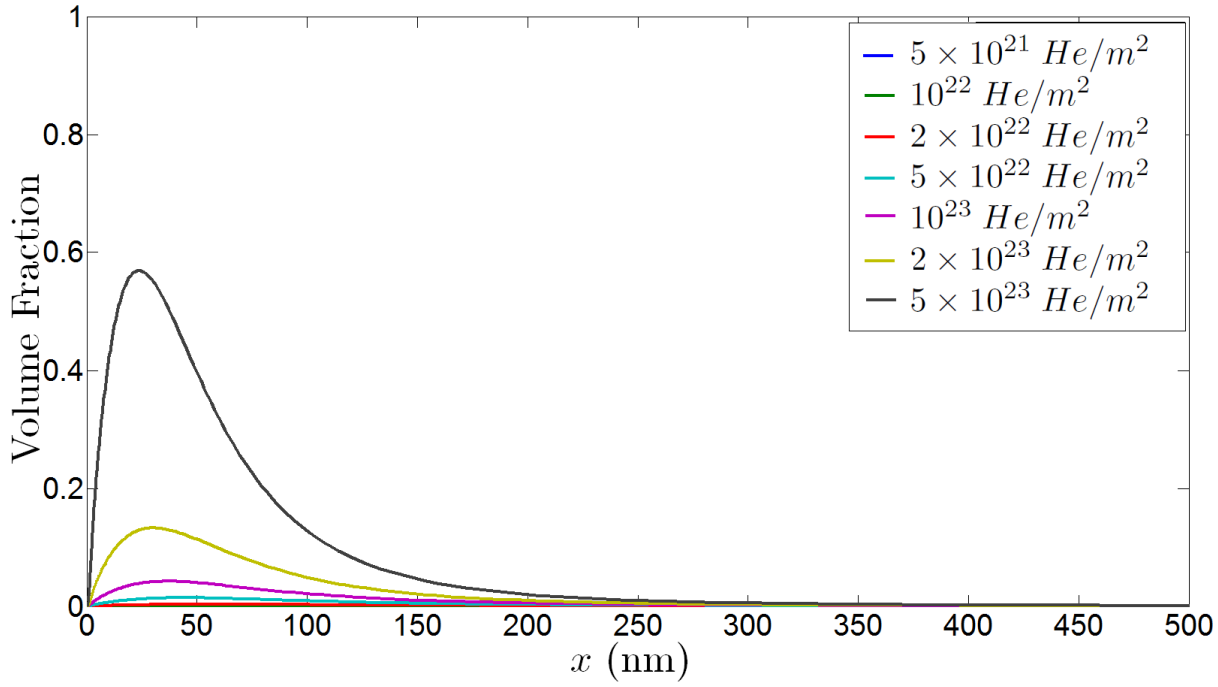
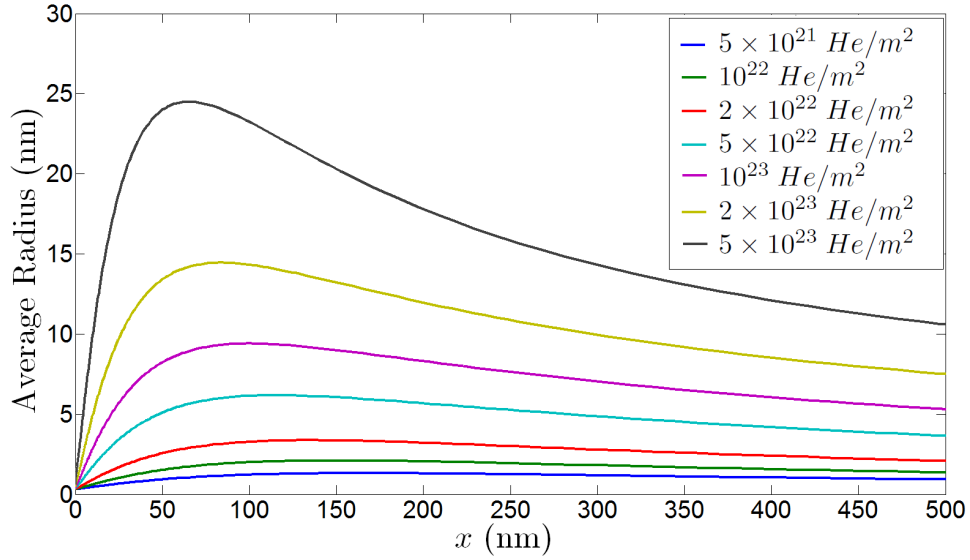
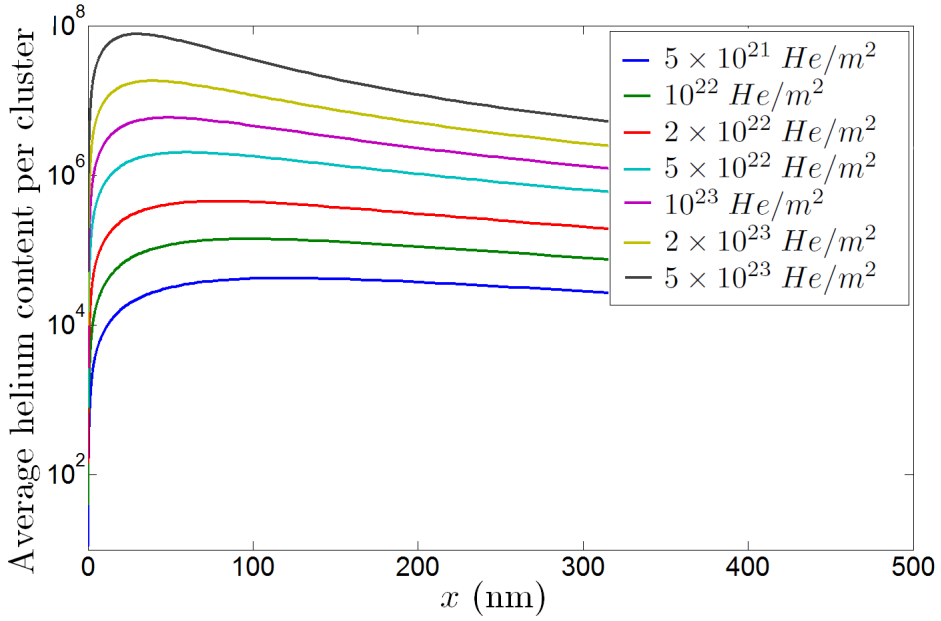


Figure 6.11: Volume fraction of helium species under the tungsten surface after $10^{22} m^{-2}s^{-1}$ 100 eV helium implantation at 1000 K up to a fluence of $5 \times 10^{23} m^{-2}$.

Figure 6.12 shows the corresponding growth of helium vacancy clusters in the same simulation. At a fluence of $5 \times 10^{23} m^{-2}$, 25 nanometer wide helium bubbles have formed containing millions of helium atoms at a concentration of 10^{-6} nm^{-3} and a distance of 50 nanometers below the surface. Hence, in this simulation the dilute approximation breaks down well before bubble bursting events take place.



(a) Average radius

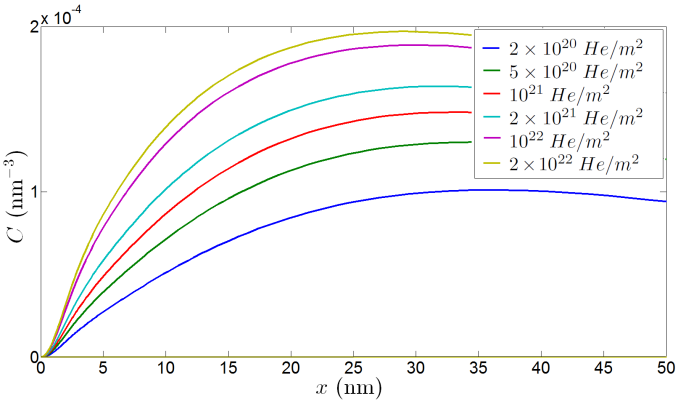


(b) Average helium content

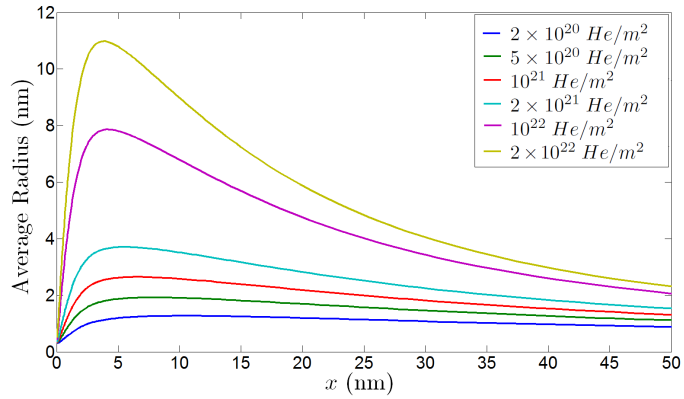
Figure 6.12: Average radius (6.12a) and helium content (6.12b) under the tungsten surface after $10^{22}m^{-2}s^{-1}$ 100 eV helium implantation at 1000 K up to a fluence of $5 \times 10^{23}m^{-2}$.

Influence of temperature

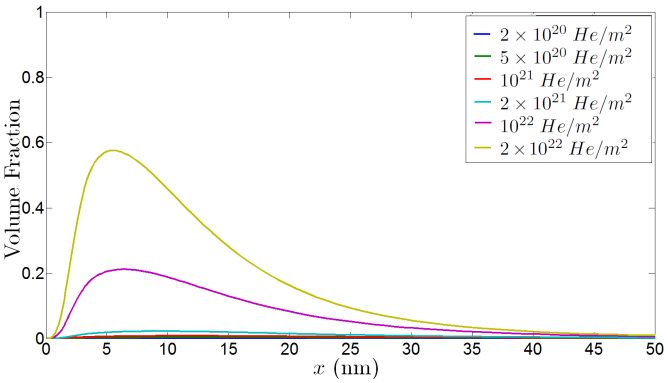
Figures 6.13 and 6.14 show the strong effect of temperature on the model predictions. In the case of helium implantation at 500 Kelvin, the lower diffusivity of helium interstitials produces a faster rate of self-trapping and clustering which occurs closer to the surface: the model predicts high concentrations ($\geq 10^{-4} nm^{-3}$) of large clusters (radius $\geq$ 10 nm) close to the surface for very low fluences ($\approx 10^{22} m^{-2}$). Based on molecular dynamics simulations, we would then expect bubble bursting phenomenon to occur before the dilute limit breaks down and bubble coalescence takes place. We also do not observe a plug of helium bubbles propagating towards the surface, as was observed at higher temperature since this bubble layer has already formed close to the implantation layer. In the case of irradiation at 1500 Kelvin, the enhanced mobility drastically lowers the amount of clustering and self-trapping. Therefore, no significant amount of helium bubbles are predicted to form below the tungsten surface even at high fluences ($\geq 5 \times 10^{25} m^{-2}$).



(a) Concentration of large HeV clusters ($\geq He_{250}V_{50}$)



(b) Average radius



(c) Volume fraction

Figure 6.13: Concentration of large HeV clusters (6.13a),average radius (6.13b) and volume fraction (6.13c) under the tungsten surface after $10^{22}m^{-2}s^{-1}$ 100 eV helium implantation at 500 K up to a fluence of $2 \times 10^{22}m^{-2}$.

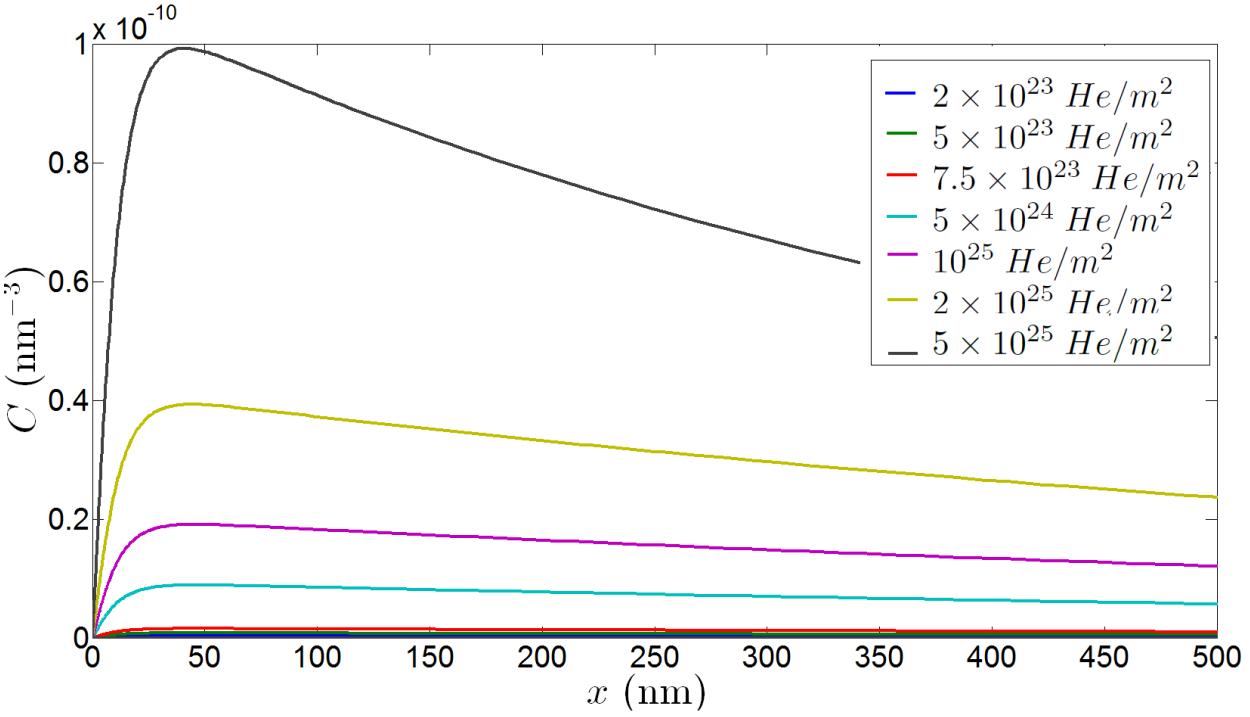


Figure 6.14: Concentration of large HeV clusters ($\geq He_{250}V_{50}$) under the tungsten surface after $10^{22}m^{-2}s^{-1}$ 100 eV helium implantation at 1500 K up to a fluence of $5 \times 10^{25}m^{-2}$.

These results predict that lower temperature and higher flux produce higher concentrations of helium bubbles with larger radius, which are predicted to form closer to the surface. Therefore, we would expect significant surface morphology changes to occur for the lowest temperatures. However, experimental evidence shows the opposite effect; Miyamoto et al. [22] observe a large concentration of small nanometer-sized helium bubbles forming under the tungsten surface at 573 Kelvin under combined helium and deuterium implantation. The bubble concentration is above the percolation threshold and thus, the bubbles are interlinked. However, no significant surface morphology change is observed. On the other hand, Baldwin et al. [20] and Kajita et al. [8] observe very strong surface morphology changes (e.g. "nanofuzz" formation) for temperatures as high as 1400 Kelvins. A possible explanation for this behavior is that at low temperatures (T $\sim$ 500 K), bubble bursting is impeded by a rapid coalescence of helium bubbles below the surface which relieves the pressure, while at high temperatures (T $>$ 1000 K), bubble bursting events are not impeded due to the lower concentration of helium bubbles and hence the surface morphology is strongly affected. However, this experimental observation and discrepancy with the modeling results presented here requires further research and analysis.

Comparison with an analytical model

These results are again in very good agreement with an analytical model proposed by Krasheninnikov [16], which predicts the same behavior with respect to a front of large gas bubbles propagating towards the surface followed by a region depleted in mobile helium interstitial concentration at deeper depths than this front. The qualitative picture of the analytical model is shown in figure 6.15. We observe very similar results as those predicted by our model shown in figure 6.10.

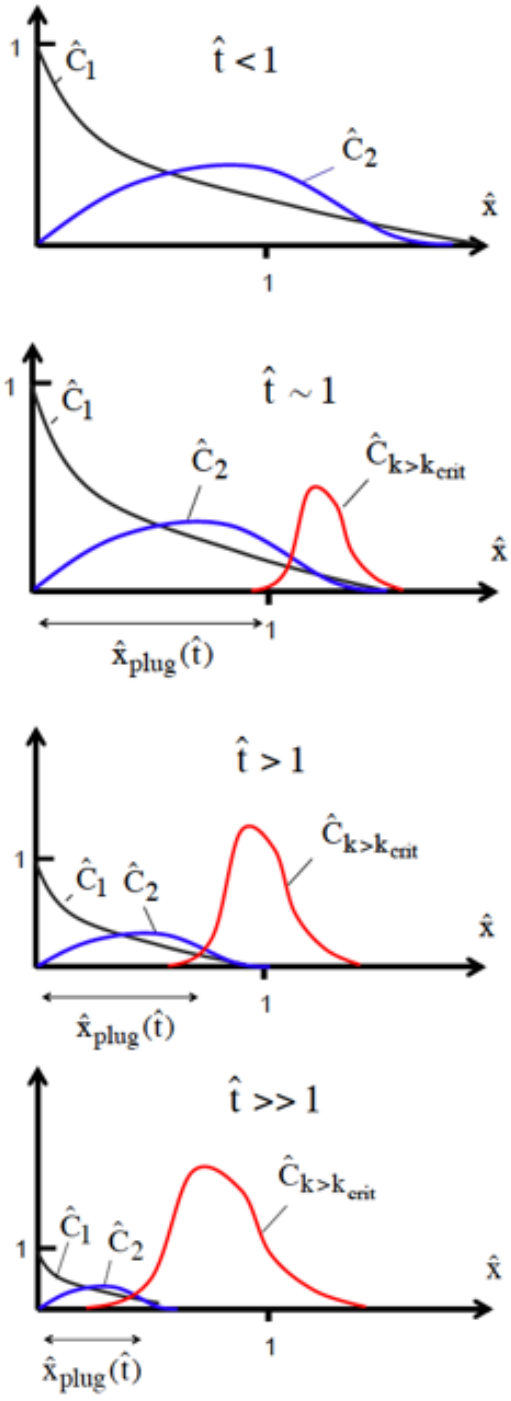


Figure 6.15: Qualitative picture of the evolution of the concentration of the helium bubbles. $\hat{C}$, $\hat{t}$ and $\hat{x}$ are dimensionless quantities depending on the flux and temperature.

Model limitations

Several factors are not yet considered within this model and will be the object of further study: The high volume fraction makes the results of the cluster dynamics model less reliable for high fluences in the low temperature (T $\sim$ 500 K) range. Therefore, the growth of moderately large gas bubbles in a high density environment should be further investigated using multiscale modeling techniques. The surface proximity and the possibility of drift diffusion forces acting on helium and small clusters have also not been considered in this work.

In the high temperature range (T $\sim$ 1500 K), the model predicts a much lower helium bubble density than what is observed in experiments. A possible reason is that the model neglects impurities in the tungsten materials, which can act as trapping sites for helium interstitial atoms and possibly enhance the nucleation of small He_xV_y clusters. Further investigation of the properties of impurity-helium interactions is therefore recommended, as well as additional research to validate the helium-vacancy thermodynamic and kinetic parameters used in this work.

6.4 Conclusion

We have described a cluster dynamics model to simulate low-energy helium implantation in tungsten under fusion relevant conditions at high fluxes and temperatures. The key elements of the model are the high mobility of helium interstitial atoms in the tungsten matrix, the self-trapping of helium atoms to form mobile helium clusters, and the trap mutation process to grow larger helium-vacancy clusters. The model is in excellent agreement with an analytical model developed by S. Krasheninnikov and presented in reference [16]. We predict that self-trapping of helium atoms does not occur in tungsten tendrils at temperatures where tungsten nanofuzz is observed to form, and hence the observed helium gas bubbles should be formed directly under the surface before surface morphology changes occur. For implantation of helium into a perfect tungsten surface with an infinite half-slab geometry, the model identifies different regimes depending on the temperature: for a given fluence, large concentrations of helium gas bubbles are formed close to the surface at low temperatures (T $\approx$ 500 K), while lower concentrations of smaller gas bubbles are formed deeper into the material at intermediate temperatures (T $\approx$ 1000 K). The model ceases to be valid at a temperature dependent fluence due to either bubble bursting phenomena expected to take place near the surface (but not explicitly modeled here) or due to a high volume fraction of helium species leading to bubble coalescence. At higher temperatures (1500 K), the model predicts a much smaller concentration of large helium-vacancy clusters, in apparent disagreement with experimental observations, which might be caused by not taking into account the effect of the various impurities in the tungsten material. These processes will be the object of further investigation in future work.

Chapter 7

Conclusion

The search for a reliable source of energy has led us to consider nuclear fusion as a viable alternative to current fossil fuels. The development of fusion reactors depends on the ability to solve the materials issues associated with the plasma facing components. This research has used a multi-scale modeling approach based on a continuum cluster dynamics model and molecular dynamics to simulate the irradiation of a tungsten divertor exposed to helium implantation conditions relevant to future nuclear fusion reactors.

A cluster dynamics model framework for helium interactions in tungsten has been developed in chapter 2, including the conditions of applicability of the model (diffusion limited reactions, dilute limit approximation, no spatial correlations). The crucial physical processes responsible for the modification of the tungsten microstructure have been identified using molecular dynamics simulations. An extension of the model has been developed in chapter 6 to deal with very large helium-vacancy clusters.

We have used molecular dynamics simulations to determine a consistent set of parameters for the cluster dynamics model. A method to accurately determine the parameters with the highest impact on the model results, the diffusion coefficients, has been presented in chapter 3. The diffusion coefficients and binding energies for each species were calculated using molecular dynamics simulations with the same input potentials, while the capture radii were determined using semi-empirical relations. The limit for the maximum number of helium per vacancy, ultimately determining which species are considered in the model, was shown to be approximately 4 for large helium-vacancy clusters.

In chapter 4, a parallel solver using a decomposition of the reaction-diffusion equations into independent local subproblems has been introduced. The good parallel performances for both strong and weak scaling indicate that the extension to a two- or three-dimensional cluster dynamics model

using a similar algorithm is possible. Convergence results show the effect of the stiffness of the reaction-diffusion equation on the order of accuracy of the numerical scheme.

Cluster dynamics predictions for various helium implantation conditions were presented in chapter 5 and show that the cluster dynamics code correctly models the key atomistic physical processes (diffusion, reaction, dissociation and trap mutation), which impact the tungsten microstructure. The comparison of helium desorption experimental and simulation results serve as a benchmark for the model, while the comparison with the molecular dynamics results give insight into possible issues with the cluster dynamics model for simulating high fluxes and temperatures. It was also shown that caution should be taken when observing results of molecular dynamics simulations of helium implantation on tungsten under fusion relevant conditions, since the high non-physical fluxes used in molecular dynamics strongly impact the results so that an extrapolation to lower fluxes is not always possible.

The cluster dynamics results under fusion relevant conditions presented in chapter 6 indicate that the results strongly depend on the geometry, flux and temperature. For a tendril geometry corresponding to the observed tungsten "fuzz", the results indicate that no large helium-vacancy clusters can nucleate in the tendril without a pre-existing nucleation site, in agreement with an analytical model. Hence, we have shown that the helium gas bubbles in the tendrils observed experimentally form before the modification of the surface structure. For a half-slab geometry, we have shown that for high temperatures, large helium vacancy clusters form deep under the tungsten surface, and create a plug of defects with the peak concentration of clusters in the plug moving closer to the surface as the fluence increases. At the same time, there is a depletion of mobile helium defects beyond the plug. This results in a relatively low concentration of helium gas bubbles which grow very large. The model fails when the dilute limit approximation breaks down, and so we expect that past this point, or even before, these large gas bubbles will coalesce. At low temperatures,we have shown that a much larger concentration of smaller bubbles form closer to the tungsten surface. The model breaks down for lower fluences than at high temperatures due to expected bubble bursting of small bubbles, which has not yet been included in the cluster dynamics model.

Future work needs to be performed to obtain more general results for fusion irradiation conditions:

- The most important and most challenging task is to address the model limits. To understand the formation and growth of the fuzz, it is essential to be able to simulate bubble bursting events leading to important surface morphology changes. The validity of the model with respect to the dilute limit approximation also needs to be addressed. Whether to do so by using a modification of the continuous model or by using another model for the surface modifications is a challenging question.

- The above point also indicates that we should consider an extension of the model to two- or three- dimensions. In addition to being necessary to simulate future surface modifications, it will also allow to consider spatial heterogeneities in the tungsten material such as the effect of zones with high dislocation densities. It will also allow accurate modeling of surface effect in tendril-like geometries. This means that the solver should also be improved to deal with more dimensions. Though the SPIKE algorithm seems adaptable to several dimensions, the size of the reduced system might become eventually too large to neglect and hence a focus on the parallelization of this step is needed.

- To avoid dealing with too many species, as well as to obtain a better description than the extension to average values presented in this work, an extension of the model to a continuous cluster space past a certain cluster size should be performed. Since kinetic parameters for very large clusters appear to vary smoothly (and since we will need to extrapolate these kinetic parameters when the number of species become too large), the use of a continuous cluster space model should not impact the accuracy of the results compared to a full cluster dynamics model as the one presented in chapter 2 of this work.

- More detailed atomistic studies of the trap mutation phenomenon need to be performed since this physical process was found to be essential for fusion relevant conditions. In particular, the discrepancy between the trap mutation rates predicted by theory and observed in molecular dynamics simulations as observed in chapter 3 needs to be investigated. In addition, MD simulations show evidence of trap mutation for small HeV clusters ($< \mathrm{He}_x\mathrm{V}_2$) and loop punching for large gas bubbles ($> \mathrm{He}_x\mathrm{V}_{50}$), in which a SIA cluster is emitted instead of a single SIA. In this work, only trap mutation is modeled. This is correct for small bubbles, but for large bubbles it is an approximation which can be seen as a discrete loop punching process, in which the over-pressurized bubble ejects a succession of SIAs instead of a SIA cluster. Further work is needed to determine the impact of this approximation.

- A detailed study of the effects of impurities and displacement damage in tungsten is necessary. These impurities may enhance nucleation of helium-vacancy clusters and hence strongly affect the results. To account for impurities in the model, the kinetic parameters for impurities such as binding energies with other helium species should be calculated using, e.g., molecular dynamics.

- Finally, the cluster dynamics framework can be applied to other types of defects. In particular, the work performed here can be applied to hydrogen implantation. It is also possible to develop a framework for mixed helium-hydrogen implantation, which is more complex since mixed helium-hydrogen-vacancy clusters can form, thus largely increasing the number of species in the model.

Bibliography

[1] BP, "BP statistical review of world energy," tech. rep., British Petroleum, June 2012.

[2] "Energy information administration." http://www.eia.gov/countries/data.cfm.

[3] "Environmental protection agency." http://www.epa.gov/climatechange/ghgemissions/global.html.

[4] "Fusion dreams delayed," *Nature*, vol. 459, pp. 488–489, 2009.

[5] G. Federici, C. Skinner, J. Brooks, J. Coad, C. Grisolia, A. Haasz, A. Hassanein, V. Philipps, C. Pitcher, J. Roth, W. Wampler, and D. Whyte, "Plasma-material interactions in current tokamaks and their implications for next step fusion reactors," *Nuclear Fusion*, vol. 41, no. 12, 2001.

[6] S. Gilliam, S. Gidcumb, N. Parikh, D. Forsythe, B. Patnaik, J. Hunn, L. Snead, and G. Lamaze, "Retention and surface blistering of helium irradiated tungsten as a first wall material," *Journal of Nuclear Materials*, vol. 347, no. 3, pp. 289 – 297, 2005.

[7] T. Hino, K. Koyama, Y. Yamauchi, and Y. Hirohata, "Hydrogen retention properties of polycrystalline tungsten and helium irradiated tungsten," *Fusion Engineering and Design*, vol. 39-40, no. 0, pp. 227 – 233, 1998.

[8] S. Kajita, W. Sakaguchi, N. Ohno, N. Yoshida, and T. Saeki, "Formation process of tungsten nanostructure by the exposure to helium plasma under fusion relevant plasma conditions," *Nuclear Fusion*, vol. 49, no. 9, p. 095005, 2009.

[9] J. Ziegler, J. Biersack, and M. Ziegler, *SRIM - The Stopping and Range of Ions in Matter*. SRIM Company, 2013.

[10] J.-Y. Tinevez, "Mean square displacement analysis of particles trajectories." http://www.mathworks.com/matlabcentral/fileexchange/authors/29713.

[11] C. Becquart, C. Domain, U. Sarkar, A. DeBacker, and M. Hou, "Microstructural evolution of irradiated tungsten: Ab initio parameterisation of an okmc model," *Journal of Nuclear Materials*, vol. 403, no. 13, pp. 75 – 88, 2010.

[12] N. Juslin and B. Wirth, "Interatomic potentials for simulation of he bubble formation in w," *Journal of Nuclear Materials*, vol. 432, no. 13, pp. 61 – 66, 2013.

[13] E.Hairer and G.Wanner, *Solving Ordinary Differential Equations II - Stiff and Differential-Algebraic Problems*. Springer-Verlag, 1980.

[14] E. V. Kornelsen, "The interaction of injected helium with lattice defects in a tungsten crystal," *Radiation Effects*, vol. 13, no. 3-4, pp. 227–236, 1972.

[15] F. Sefta, K. D. Hammond, N. Juslin, and B. D. Wirth, "Tungsten surface evolution by helium bubble nucleation, growth and rupture," *Nuclear Fusion*, vol. 53, no. 7, p. 073015, 2013.

[16] S. Krasheninnikov, T.Faney, and B. Wirth, "On helium cluster dynamics in tungsten plasma facing components of fusion devices," *Nuclear Fusion*, vol. Submitted, 2013.

[17] D. J. Reed, "A review of recent theoretical developments in the understanding of the migration of helium in metals and its interaction with lattice defects," *Radiation Effects*, vol. 31, no. 3, pp. 129–147, 1977.

[18] W. D. Wilson and C. L. Bisson, "Rare gas complexes in tungsten," *Radiation Effects*, vol. 22, no. 1, pp. 63–66, 1974.

[19] "Intergovernmental panel on climate change." http://www.ipcc.ch/index.htm.

[20] M. Baldwin and R. Doerner, "Helium induced nanoscopic morphology on tungsten under fusion relevant plasma conditions," *Nuclear Fusion*, vol. 48, no. 3, p. 035001, 2008.

[21] M. Baldwin, T. Lynch, R. Doerner, and J. Yu, "Nanostructure formation on tungsten exposed to low-pressure rf helium plasmas: A study of ion energy threshold and early stage growth," *Journal of Nuclear Materials*, vol. 415, no. 1, Supplement, pp. S104 – S107, 2011.

[22] M. Miyamoto, D. Nishijima, M. Baldwin, R. Doerner, Y. Ueda, K. Yasunaga, N. Yoshida, and K. Ono, "Microscopic damage of tungsten exposed to deuteriumhelium mixture plasma in {PISCES} and its impacts on retention property," *Journal of Nuclear Materials*, vol. 415, no. 1, Supplement, pp. S657 – S660, 2011.

[23] S. Takamura, N. Ohno, D. Nishijima, and S. Kajita, "Formation of nanostructured tungsten with arborescent shape due to helium plasma irradiation," *Plasma Fusion Res.*, vol. 1, no. 051, 2006.

[24] C. Becquart and C. Domain, "Ab initio calculations about intrinsic point defects and He in W," *Nuclear Instruments and Methods in Physics Research Section B: Beam Interactions with Materials and Atoms*, vol. 255, no. 1, pp. 23 – 26, 2007.

[25] K. Russell, "Nucleation of voids in irradiated metals," *Acta Metallurgica*, vol. 19, no. 8, pp. 753 – 758, 1971.

[26] K. Russell, "Thermodynamics of gas-containing voids in metals," *Acta Metallurgica*, vol. 20, no. 7, pp. 899 – 907, 1972.

[27] J. L. Katz and H. Wiedersich, "Nucleation of voids in materials supersaturated with vacancies and interstitials," *The Journal of Chemical Physics*, vol. 55, no. 3, pp. 1414–1425, 1971.

[28] Y. Watanabe, H. Iwakiri, N. Yoshida, K. Morishita, and A. Kohyama, "Formation of interstitial loops in tungsten under helium ion irradiation: Rate theory modeling and experiment," *Nuclear Instruments and Methods in Physics Research Section B: Beam Interactions with Materials and Atoms*, vol. 255, no. 1, pp. 32 – 36, 2007.

[29] D. Xu and B. D. Wirth, "Modeling spatially dependent kinetics of helium desorption in {BCC} iron following he ion implantation," *Journal of Nuclear Materials*, vol. 403, no. 13, pp. 184 – 190, 2010.

[30] D. Xu and B. D. Wirth, "Combining in situ transmission electron microscopy irradiation experiments with cluster dynamics modeling to study nanoscale defect agglomeration in structural metals," *Acta Materialia*, vol. 60, no. 10, pp. 4286 – 4302, 2012.

[31] Y. Li, W. Zhou, L. Huang, Z. Zeng, and X. Ju, "Cluster dynamics modeling of accumulation and diffusion of helium in neutron irradiated tungsten," *Journal of Nuclear Materials*, vol. 431, no. 13, pp. 26 – 32, 2012.

[32] L. YANG, H. LIU, and X. ZU, "First-principles study of the migration of helium in tungsten," *International Journal of Modern Physics B*, vol. 23, no. 08, pp. 2077–2082, 2009.

[33] A. Van Veen, L. M. Caspers, E. V. Kornelsen, R. Fastenau, A. Van Gorkum, and A. Warnaar, "Vacancy creation by helium trapping at substitutional krypton in tungsten," *physica status solidi (a)*, vol. 40, no. 1, pp. 235–246, 1977.

[34] A. van Veen, A. Warnaar, and L. Caspers, "Clustering of krypton in tungsten observed by helium desorption spectrometry," *Vacuum*, vol. 30, no. 3, pp. 109 – 115, 1980.

[35] A. van Veen, "Thermal helium desoprtion spectrometry (thds) as a tool for the study of vacancies and self-interstitials," *Material Science Forum*, vol. 15-18, pp. 86 – 96, 1987.

[36] T. R. Waite, "Theoretical treatment of the kinetics of diffusion-limited reactions," *Phys. Rev.*, vol. 107, pp. 463–470, Jul 1957.

[37] C. J. Ortiz and M. J. Caturla, "Simulation of defect evolution in irradiated materials: Role of intracascade clustering and correlated recombination," *Phys. Rev. B*, vol. 75, p. 184101, May 2007.

[38] S. Plimpton, "Fast parallel algorithms for short-range molecular dynamics," *Journal of Computational Physics*, vol. 117, no. 1, pp. 1 – 19, 1995.

[39] M. W. Finnis and J. E. Sinclair, "A simple empirical n-body potential for transition metals," *Philosophical Magazine A*, vol. 50, no. 1, pp. 45–55, 1984.

[40] G. J. Ackland and R. Thetford, "An improved n-body semi-empirical model for body-centred cubic transition metals," *Philosophical Magazine A*, vol. 56, no. 1, pp. 15–30, 1987.

[41] N. Juslin and B. Wirth, "Molecular dynamics simulation of the effect of sub-surface helium bubbles on hydrogen retention in tungsten," *Journal of Nuclear Materials*, vol. 438, Supplement, pp. S1221 – S1223, 2013.

[42] J. Biersack and J. Ziegler, "Refined universal potentials in atomic collisions," *Nuclear Instruments and Methods in Physics Research*, vol. 194, no. 13, pp. 93 – 100, 1982.

[43] D. Beck, "A new interatomic potential function for helium," *Molecular Physics*, vol. 14, no. 4, pp. 311–315, 1968.

[44] K. Morishita, R. Sugano, B. Wirth, and T. D. de la Rubia, "Thermal stability of heliumvacancy clusters in iron," *Nuclear Instruments and Methods in Physics Research Section B: Beam Interactions with Materials and Atoms*, vol. 202, no. 0, pp. 76 – 81, 2003.

[45] L. Verlet, "Computer "experiments" on classical fluids. i. thermodynamical properties of lennard-jones molecules," *Phys. Rev.*, vol. 159, pp. 98–103, Jul 1967.

[46] P. S. Grassia, E. J. Hinch, and L. C. Nitsche, "Computer simulations of brownian motion of complex systems," *Journal of Fluid Mechanics*, vol. 282, pp. 373–403, 1 1995.

[47] S. L. Dudarev, "The non-arrhenius migration of interstitial defects in bcc transition metals," *Comptes Rendus Physique*, vol. 9, no. 34, pp. 409 – 417, 2008.

[48] S. Chandrasekhar, "Stochastic problems in physics and astronomy," *Rev. Mod. Phys.*, vol. 15, pp. 1–89, Jan 1943.

[49] R. Huang, I. Chavez, K. M. Taute, B. Luki, S. Jeney, M. G. Raizen, and E.-L. Florin, "Direct observation of the full transition from ballistic to diffusive brownian motion in a liquid," *Nature Physics*, vol. 7, pp. 576–580, 2011.

[50] A. Einstein, "ber die von der molekularkinetischen theorie der wrme geforderte bewegung von in ruhenden flssigkeiten suspendierten teilchen," *Annalen der Physik*, vol. 322, no. 8, pp. 549–560, 1905.

[51] P. M. Derlet, D. Nguyen-Manh, and S. L. Dudarev, "Multiscale modeling of crowdion and vacancy defects in body-centered-cubic transition metals," *Phys. Rev. B*, vol. 76, p. 054107, Aug 2007.

[52] J. Amano and D. N. Seidman, "Diffusivity of 3he atoms in perfect tungsten crystals," *Journal of Applied Physics*, vol. 56, no. 4, 1984.

[53] A. Wagner and D. N. Seidman, "Range profiles of 300- and 475-ev $^4\mathrm{He}^+$ ions and the diffusivity of $^4\mathrm{He}$ in tungsten," *Phys. Rev. Lett.*, vol. 42, pp. 515–518, Feb 1979.

[54] F. Dausinger and H. Schultz, "Long-range migration of self-interstitial atoms in tungsten," *Phys. Rev. Lett.*, vol. 35, pp. 1773–1775, Dec 1975.

[55] Tanimoto, H., Mizubayashi, H., Nishimura, H., and Okuda, S., "A study of self-interstitial atom in w by means of low-temperature irradiations," *J. Phys. IV France*, vol. 06, pp. C8–285–C8–288, 1996.

[56] R. Balluffi, "Vacancy defect mobilities and binding energies obtained from annealing studies," *Journal of Nuclear Materials*, vol. 6970, no. 0, pp. 240 – 263, 1978.

[57] J. N. Mundy, S. T. Ockers, and L. C. Smedskjaer, "Vacancy migration enthalpy in tungsten at high temperatures," *Philosophical Magazine A*, vol. 56, no. 6, pp. 851–860, 1987.

[58] A. Satta, F. Willaime, and S. de Gironcoli, "Vacancy self-diffusion parameters in tungsten: Finite electron-temperature lda calculations," *Phys. Rev. B*, vol. 57, pp. 11184–11192, May 1998.

[59] R. Johnson and R. J. W.D. Wilson in: P.C. Gehlen, J.R. Beeler, *Interatomic Potentials and Simulation of Lattice Defects,*. Plenum, 1972.

[60] R. A. Johnson, "Point-defect calculations for tungsten," *Phys. Rev. B*, vol. 27, pp. 2014–2018, Feb 1983.

[61] J. M. Harder and D. J. Bacon, "Point-defect and stacking-fault properties in body-centred-cubic metals with n-body interatomic potentials," *Philosophical Magazine A*, vol. 54, no. 5, pp. 651–661, 1986.

[62] W. Xu and J. B. Adams, "Fourth moment approximation to tight binding: application to bcc transition metals," *Surface Science*, vol. 301, no. 13, pp. 371 – 385, 1994.

[63] C. Domain, C. Becquart, and L. Malerba, "Simulation of radiation damage in fe alloys: an object kinetic monte carlo approach," *Journal of Nuclear Materials*, vol. 335, no. 1, pp. 121 – 145, 2004.

[64] M.Feinberg, "Lectures on chemical reaction networks, http://www.chbmeng.ohio-state.edu/ feinberg/lecturesonreactionnetworks/," 1979.

[65] M. Pierre, "Global existence in reaction-diffusion systems with control of mass: a survey," *Milan Journal of Mathematics*, vol. 78, 2010.

[66] S. Hollis and J. Morgan, "On the blow-up of solutions to some semilinear and quasilinear reaction-diffusion systems," *Rocky Mountain Journal of Mathematics*, vol. 24, 1994.

[67] J. Morgan, "Global existence for semilinear parabolic systems," *SIAM Journal on Mathematical Analysis*, vol. 20, no. 5, pp. 1128–1144, 1989.

[68] N. Sfakianakis, *Finite difference schemes on non-uniform meshes for hyperbolic conservation laws*. PhD thesis, University of Crete, Department of applied mathematics, 2009.

[69] T. Faney, D. Xu, and B. Wirth, "Spatially-dependent cluster dynamics modeling of microstructure evolution in low energy helium irradiated tungsten," *Journal of Applied Physics*, vol. Submitted, 2013.

[70] S. Norsett, "Semi-explicit runge-kutta methods," *Mathematics and Computation*, vol. No. 6 University of Trondheim, 1974.

[71] E. Polizzi and A. H. Sameh, "A parallel hybrid banded system solver: the spike algorithm," *Parallel Computing*, vol. 32, no. 2, pp. 177 – 194, 2006.

[72] S. Hirshman, K. Perumalla, V. Lynch, and R. Sanchez, "Bcyclic: A parallel block tridiagonal matrix cyclic solver," *Journal of Computational Physics*, vol. 229, no. 18, pp. 6392 – 6404, 2010.

[73] L. O. Jay, "Inexact simplified newton iterations for implicit runge-kutta methods.," *SIAM J. Numer. Anal*, vol. 38, pp. 1369–1388, 2000.

[74] A. Sandu, F. Potra, G. Carmichael, and V. Damian, "Efficient implementation of fully implicit methods for atmospheric chemical kinetics," *Journal of Computational Physics*, vol. 129, no. 1, pp. 101 – 110, 1996.

[75] G. Karypis and V. Kumar, "Parmetis - parallel graph partitioning and fill-reducing matrix ordering," 2013.

[76] H. Zhang, J. C. Linford, A. Sandu, and R. Sander, "Chemical mechanism solvers in air quality models," *Atmosphere*, vol. 2, no. 3, pp. 510–532, 2011.

[77] A. Sandu, "Positive numerical integration methods for chemical kinetic systems," *Journal of Computational Physics*, vol. 170, no. 2, pp. 589 – 602, 2001.

[78] "On the stability and accuracy of one-step methods for solving stiff systems of ordinary differential equations," *Mathematics of Computation*, vol. 28, pp. 145–162.

[79] R. Frank, J. Schneid, and C. Ueberhuber, "The concept of b-convergence," *SIAM Journal on Numerical Analysis*, vol. 18, no. 5, pp. 753–780, 1981.

[80] K. Burrage, "Efficiently implementable algebraically stable rungekutta methods," *SIAM Journal on Numerical Analysis*, vol. 19, no. 2, pp. 245–258, 1982.

[81] J. R. CASH, "Diagonally implicit runge-kutta formulae with error estimates," *IMA Journal of Applied Mathematics*, vol. 24, no. 3, pp. 293–301, 1979.

[82] R. Alexander, "Diagonally implicit rungekutta methods for stiff o.d.e.s," *SIAM Journal on Numerical Analysis*, vol. 14, no. 6, pp. 1006–1021, 1977.

[83] E. Gallopoulos and Y. Saad, "A parallel block cyclic reduction algorithm for the fast solution of elliptic equations," *Parallel Computing*, vol. 10, no. 2, pp. 143 – 159, 1989.

[84] A. Lasa, K. Henriksson, and K. Nordlund, "{MD} simulations of onset of tungsten fuzz formation under helium irradiation," *Nuclear Instruments and Methods in Physics Research Section B: Beam Interactions with Materials and Atoms*, vol. 303, pp. 156 – 161, 2013.

[85] N. Juslin and B. Wirth, "Manuscript in preparation,"

[86] B. Wirth, "Manuscript in submission," *11th International Symposium on Fusion Nuclear Technology*, 2013.